Dimensionality Reduction Methods for Spatiotemporal Magnetic Resonance Imaging

Jae Eun Song

The Graduate School

Yonsei University

Department of Electrical and Electronic Engineering

Dimensionality Reduction Methods for Spatiotemporal Magnetic Resonance Imaging

A Dissertation

Submitted to the Department of Electrical and Electronic Engineering

and the Graduate School of Yonsei University

in partial fulfillment of the

requirements for the degree of

Doctor of Philosophy

Jae Eun Song

August 2020

This certifies that the dissertation
of Jae Eun Song is approved.

Thesis Supervisor: Dong-Hyun Kim

Dosik Hwang

Bumsub Ham

Seung Ah Lee

Yoonho Nam

The Graduate School

Yonsei University

August 2020

감사의 글

학위과정을 마무리하며 지난 시간들을 돌아보니, 감사한 분들이 정말 많습니다. 이 지면을 통해 그 분들께 감사의 마음을 전하고자 합니다.

먼저, 지도 교수님이신 김동현 교수님께 감사드립니다. 김동현 교수님이 지도 교수님이 아니셨다면 저는 학위과정을 시작할 수도, 마무리할 수도 없었을 것이라는 생각이 듭니다. 배움이 턱없이 부족했던 저에게 기회를 주셨고, 더딘 발전에도 끊임없는 관심으로 이끌어 주셔서 너무나 감사합니다.

학위논문 심사를 맡아 주신 다른 교수님들께 감사드립니다. 황도식 교수님, 함범섭 교수님, 이승아 교수님, 남윤호 교수님, 귀한시간을 내어 주셔서 감사합니다.

의료영상연구실 동료들에게 감사드립니다. 부족함이 많았던 저를 이끌어 주시며 연구의 전환점을 마련해주신 재욱오빠, 너무나 감사합니다. 연구실의 기틀을 마련해 주신 모든 선배님들, 부족한 후배를 이끌어주어 고맙습니다. 앞으로 연구실을 이끌어갈 후배들, 연차가 많이 차이나는 불편한 선배였을 텐데도 항상 잊지않고 챙겨주어 고맙습니다.

에비슨관에서 13C 연구를 함께한 분들께 감사드립니다. 송호택 교수님, 최영숙 박사님, 왕은경 선생님, 김대희 선생님, 최형욱 선생님, 지정현 선생님, 첫 주제를 잘 마무리할 수 있게 도와주셔서 감사합니다.

가족들에게 감사드립니다. 독립적인 둘째 딸에게 항상 서운하시면서도 고마워하신 부모님, 앞으로도 걱정 끼치지 않게 잘하겠습니다. 각자의 개성이 뚜렷해 셋이 모이면 서로 다른 이야기를 하는데도 즐거운 자매들, 앞으로도 함께 좋은 추억을 쌓아가고 싶습니다.

마지막으로, 학부과정의 시작부터 학위과정의 마무리까지, 십여년간 연세에서 스쳐간 모든 이들에게 감사의 마음을 전하고 싶습니다. 이십대의 전부를 보낸 이곳에서 많은 사람들과 소중한 추억을 쌓았습니다. 이제는 연락이 닿지 않는 사람도, 앞으로 연락이 닿지 않을 사람도, 저와 함께해줘서 너무나 고맙습니다.

2020 년 여름
송재은 드림

Contents

List of Figures

List of Tables

Abstract

Dimensionality Reduction Methods for Spatiotemporal Magnetic Resonance Imaging

Jae Eun Song
Dept. of Electrical and Electronic Engineering
The Graduate School
Yonsei University

Magnetic resonance imaging (MRI) is a multidisciplinary imaging modality which offers soft tissue contrast without ionization and invasive procedures. Its flexibility allows many applications including multi-contrast image, metabolic activities in tissues, functional activities in the brain, and electromagnetic properties.

Spatiotemporal MRI dataset provides temporal information as well as spatial information. Several MRI datasets have redundant temporal features such as free induction decay (FID), T2* relaxation, and T1 relaxation, which can be represented through low dimensional subspaces. The dataset reconstructed by using subspaces has a lower dimension than the original dataset, which is called intrinsic dimensionality.

In this dissertation, I propose dimensionality reduction methods for high dimensional MRI, specifically spatiotemporal MRI including magnetic resonance spectroscopic imaging (MRSI) and multi-echo gradient echo (mGRE) imaging. As a linear approach, the consistency of spectral basis of dynamic hyperpolarized 13C MRSI is investigated using principal component analysis (PCA). The spectral basis feature allows for increased SNR as well as reduced scan time not. Another linear approach, robust principal component analysis (rPCA) is implemented to mGRE imaging dataset for myelin water fraction (MWF) mapping. The extracted temporal basis is well corresponded to the temporal evolution of mGRE sources. The separation of sparse feature allows robustness to noise and artifacts, leading to improvements of MWF. As a nonlinear approach, robust deep autoencoder (rDAE) is implemented to mGRE imaging dataset for MWF mapping. The robustness to noise and artifact maintained and the complex-valued feature is extracted from mGRE sources as well.

Keywords: magnetic resonance imaging, dimensionality reduction, principal component analysis, autoencoder, machine learning,

Chapter 1

Introduction

Magnetic resonance imaging (MRI) is an elaborate imaging modality that provides versatile contrasts of tissues without ionization and invasive procedure. The application of MRI is not limited to providing anatomical structure but varies including metabolic imaging, microstructure imaging, and blood flow assessment.

The MR dataset is acquired using sequences tailored to each application, and the acquired dataset is composed of various dimensions including spatial, temporal, and spectral. Among numerous sequences, magnetic resonance spectroscopic imaging (MRSI) and multi-echo gradient-echo (mGRE) imaging provide temporal features of free induction decay (FID) and T2* relaxation, respectively. For MRSI, the spectral distribution is investigated by Fourier Transform of the FID in each spatial voxel and is assessed for quantitative estimates of the metabolites. For mGRE, the T2* decaying at each spatial voxel is investigated by curve-fitting and is assessed for myelin water imaging and R2* mapping.

The high dimensional spatiotemporal dataset possesses redundant features (e.g., FID of MRSI and T2* decay of mGRE), which can be extracted through dimensionality reduction. Dimensionality reduction techniques are largely divided into linear and non-linear approaches according to the projection relationship between the original dataset and the subspace. Principal component analysis (PCA), the most representative linear

dimensionality reduction technique, performs dimensionality reduction by projecting the data into a linear subspace of lower dimensionality. Robust principal component analysis (rPCA), which is similar to PCA, outperforms PCA for the corrupted dataset by separating anomaly features into a sparse component. Autoencoder, the most representative non-linear dimensionality reduction technique, captures the non-linear low dimensional feature at the bottleneck layer by allowing nonlinearity using non-linear activation function. Consequently, the dataset reconstructed by using subspaces has a lower dimension than the original dataset, which is called intrinsic dimensionality.

This dissertation aims to develop dimensionality reduction techniques for spatiotemporal MRI, specifically for MRSI and mGRE dataset. In Chapter 3, I propose a subspace approach for dynamic hyperpolarized 13C MRSI. In Chapter 4, I propose a multi low dimensional rPCA for myelin water fraction (MWF) mapping using mGRE imaging. In Chapter 5, I propose a multi low dimensional autoencoder for MWF mapping using mGRE imaging.

1.1 Outline

Chapter 2: Background provides fundamentals of MRI, and dimensionality reduction techniques. I start with the fundamentals of MRI which offers MR physics for acquisition and reconstruction including magnetization, excitation, relaxation, and pulse sequence. Then, I describe essential dimensionality reduction techniques including principal component analysis (PCA), non-negative matrix factorization (NMF), robust principal

component analysis (rPCA), and robust deep autoencoder (rDAE).

Chapter 3: Dynamic Hyperpolarized 13C MRSI using SPICE (SPectroscopic Imaging by exploiting spatiospectral CorrElation) in Mouse Kidney at 9.4 T deals with the subspace-based spectroscopic imaging for dynamic 13C MRSI. In previous studies, the original SPICE technique was developed for 1H MRSI and the feasibility of SPICE for 13C MRSI was demonstrated. Furthermore, the consistency of principal components (referred here as a spectral basis) according to dynamic frames is validated by estimating cosine similarity. With the feasibility of a single-framed principal component, dynamic 13C MRSI is acquired and reconstructed. It is tested and analyzed in the simulations, enzyme phantom, and *in-vivo* experiments.

Chapter 4: Blind Source Separation for Myelin Water Fraction Mapping using Multi-echo Gradient-echo Imaging deals with the separation of source signals of mGRE by encouraging data-driven properties of low-rankness and sparsity. In the original rPCA algorithm, a single low-rank component was separated by using nuclear norm minimization. Furthermore, based on the data-driven properties mGRE dataset, rPCA algorithm is incorporated with incorporating hankelization and nonnegative matrix factorization. It is demonstrated that the proposed method improves the estimation of MWF. It is tested and analyzed in the simulations, and *in-vivo* experiments including healthy volunteers and patients.

Chapter 5: Robust Deep Autoencoder for mGRE Source Separation deals with the

separation of source signals of mGRE by encouraging data-driven properties of low-dimensionality and sparsity. In the original rDAE algorithm, a single low-dimensional component was separated by using deep autoencoder. Furthermore, based on the data-driven properties mGRE dataset, rDAE algorithm is incorporated with model-based single source estimation. It is demonstrated that the proposed method improves the estimation of MWF. It is tested and analyzed in the simulations, and *in-vivo* experiments including healthy volunteers and patients.

Chapter 6: Conclusion summarizes the improvements of spatiotemporal MRI reconstruction from data-driven dimensionality reduction techniques.

Chapter 2

Background

2.1 Fundamentals of Magnetic Resonance Imaging

In this chapter, I give fundamentals of MRI from magnetic resonance phenomena to data acquisition. I start with the magnetization and precession. Then, I describe excitation and relaxation. Lastly, I describe the elements of the pulse sequence and introduce two pulse sequences used in the following chapters.

2.1.1 Magnetization and Precession

Nuclei with odd numbers of protons and/or neutrons formulate spin angular momentum (e.g., 1H, 13C, etc), resulting in magnetic dipole moment. When there is no external magnetic field, magnetic dipole moments are randomly aligned. When the external magnetic field $\boldsymbol{B}$ is introduced, the magnetic dipole moments align with the direction of the external magnetic field $\boldsymbol{B}$, and the net magnetization $\boldsymbol{M}$ is formed.

In classical physics, the behavior of net magnetization along the external magnetic field is described as follows:

$$\frac{d\boldsymbol{M}}{dt} = \boldsymbol{M} \times \gamma \boldsymbol{B} \tag{2.1}$$

where γ is the gyromagnetic ratio which is unique to nuclei (e.g., 42.576 and 10.705 MHz/T for 1H and 13C, respectively). Equation (2.1) represents the precession of magnetization along the external magnetic field. The direction of the main magnetic field, $\boldsymbol{B_0}$, is commonly selected by the z-axis, which is referred to as a longitudinal axis. The net magnetization precesses along the main magnetic field with a specific angular frequency as follows:

$$\omega_0 = \gamma B_0 \tag{2.2}$$

where ω_0 is called resonance frequency, or Larmor frequency which is determined by gyromagnetic ratio and the strength of the main magnetic field.

2.1.2 Excitation and Relaxation

To tip the magnetization from the equilibrium state, an additional magnetic field with resonance frequency should be introduced. It is referred to as radiofrequency (RF) field, $\boldsymbol{B_1}$. The direction of RF field is commonly selected by xy-plane, which is referred to as a transverse plane. The magnetization resonates with RF field and results in excitation.

Following the excitation, the magnetization returns to the equilibrium state, which is called relaxation [1, 2]. It is described in T1 relaxation and T2 relaxation. T1 relaxation, M_z, refers to the recovery of the longitudinal magnetization which originates from the

energy exchange between spins and neighboring nuclei. T2 relaxation, M_{xy}, refers to the decay of the transverse magnetization which originates from the dephasing of spins. The behavior of each magnetization is described as follows:

$$\frac{dM_z}{dt} = -\frac{M_z - M_0}{T_1} \tag{2.3}$$

$$\frac{dM_{xy}}{dt} = -\frac{M_0}{T_2} \tag{2.4}$$

where M_0 is the initial magnetization at equilibrium, T1 is the longitudinal relaxation time constant, and T2 is the transverse relaxation time constant

Combining the precession and relaxation behavior, the classical physics of the magnetization is described by the Bloch equation as follows [3]:

$$\frac{d\vec{M}}{dt} = \vec{M} \times \gamma\vec{B} - \frac{M_x\hat{x} + M_y\hat{y}}{T_2} - \frac{(M_z - M_0)\hat{z}}{T_1} \tag{2.5}$$

where $\hat{x}$, $\hat{y}$, and $\hat{z}$ are the unit vectors for x, y, z-axis, respectively.

2.1.3 Pulse sequence

The pulse sequence is a combination of RF pulses, gradient waveforms, and analog-to-digital converter (ADC). The MR image contrasts are varied according to the arrangement of these elements.

The simple MGRE sequence is depicted in Figure 2.1a. The sequence begins with an RF

pulse with a slice selection gradient that selects a specific slice of the subject along the z-axis. The phase encoding gradient is then applied according to the spatial information such as FOV and resolution. Lastly, the readout gradient is applied, and the echo signal is acquired in Fourier domain using ADC. As a multi echo signal is acquired, the T2* contrast of each temporal dimension is represented.

The two spatial dimensional MRSI sequence is depicted in Figure 2.1b. Here, the readout gradient in MGRE is adapted to the other phase encoding gradient. The echo signal is acquired for each phase encoding step, without readout gradient. The free induction decay is acquired for each spatial voxel, representing the spectral distribution.

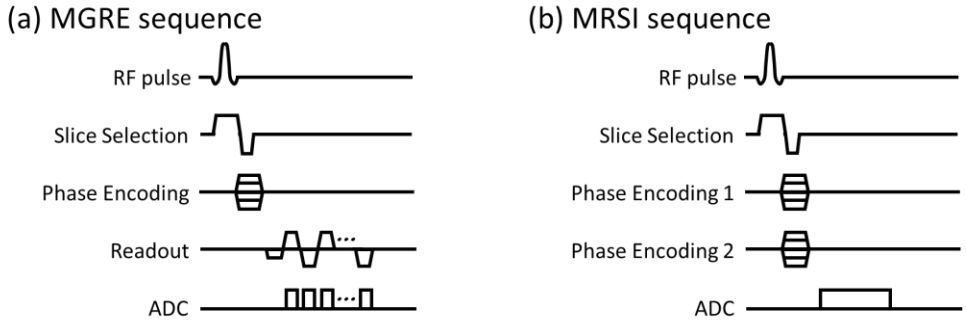

Figure 2.1. The timing diagram of pulse sequences used in the following chapters. (a) MGRE in chapters 4 and 5. (b) MRSI in chapter 3.

2.2 Dimensionality Reduction Techniques

In this chapter, I give a brief introduction of dimensionality reduction techniques which

are covered in the following chapters. As a linear technique, PCA and rPCA are presented. As a non-linear technique, DAE and rDAE are presented.

2.2.1 Principal Component Analysis

PCA is a representative linear dimensionality reduction technique. It reduces the dimensionality of data by embedding the original data matrix into a linear subspace of lower dimensionality. Statistically, it extracts a low-dimensional representation of the data that describes as much of the variance in the data as possible [4-7].

Before looking into PCA mathematically, brief linear algebra is presented [8]. For $m \times n$ asymmetry matrix $\boldsymbol{M}$, simple eigenvalue and eigenvector problem fail. More than that, two sets of singular vectors $\boldsymbol{u}$'s and $\boldsymbol{v}$'s are needed. For singular vectors, each $\boldsymbol{Mv}$ equals $\sigma\boldsymbol{u}$ as:

$$\boldsymbol{Mv}_1 = \sigma_1\boldsymbol{u}_1, \dots, \boldsymbol{Mv}_r = \sigma_r\boldsymbol{u}_r, \qquad \boldsymbol{Mv}_{r+1} = 0, \dots, \boldsymbol{Mv}_n = 0 \tag{2.6}$$

where r is the rank of $\boldsymbol{A}$, the number of independent columns, and rows. σ_k are singular values in descending order $\sigma_1 \geq \sigma_2 \geq \cdots \geq \sigma_r > 0$. The number r indicates the dimension of the column space and the row space. Equation (2.6) can be written in matrix form as:

$$\boldsymbol{MV} = \boldsymbol{U\Sigma}, \qquad \boldsymbol{M}\begin{bmatrix} \boldsymbol{v}_1 \dots \boldsymbol{v}_r \dots \boldsymbol{v}_n \end{bmatrix} = \begin{bmatrix} \boldsymbol{u}_1 \dots \boldsymbol{u}_r \dots \boldsymbol{u}_n \end{bmatrix}\begin{bmatrix} \sigma_1 & & \\ & \dots \sigma_r & \\ & & 0 \end{bmatrix} \tag{2.7}$$

where $\boldsymbol{V}$ and $\boldsymbol{U}$ are square matrices of size $n \times n$ and $m \times m$ respectively. As the columns of $\boldsymbol{v}_k$'s and $\boldsymbol{u}_k$'s are orthogonal unit vectors, $\boldsymbol{V}^T = \boldsymbol{V}^{-1}$ and $\boldsymbol{U}^T = \boldsymbol{U}^{-1}$ are satisfied. It allows us to rearrange Equation (2.7) to usual singular value decomposition (SVD) form as (Figure 2.2):

$$\boldsymbol{M} = \boldsymbol{U}\boldsymbol{\Sigma}\boldsymbol{V}^T = \sum_{k=1}^{min\{m,n\}} \sigma_k \boldsymbol{u}_k \boldsymbol{v}_k^T \tag{2.8}$$

PCA is based on rank-r approximation for matrix $\boldsymbol{M}$. The principal components of matrix $\boldsymbol{M}$ are extracted by solving matrix optimization problem as:

$$\widehat{\boldsymbol{M}} = \widehat{\boldsymbol{U}}\widehat{\boldsymbol{\Sigma}}\widehat{\boldsymbol{V}}^T = \sum_{k=1}^{r} \sigma_k \boldsymbol{u}_k \boldsymbol{v}_k^T$$

$$s.t.\ \|\boldsymbol{M} - \boldsymbol{M}\|_F \geq \sqrt{\sum_{k=r+1}^{\min\{m,n\}} \sigma_k} \tag{2.9}$$

where F indicates the Frobenius norm. By thresholding largest σ_k's, dominant subspaces are extracted.

2.2.2 Robust Principal Component Analysis

rPCA is an algorithm that recovers a low-rank matrix, $\boldsymbol{L}$, and a sparse matrix, $\boldsymbol{S}$, from the data matrix, $\boldsymbol{M}$. The arbitrary corruptions do not exhibit low-dimensionality, and consequently, these features are extracted to a sparse matrix by ℓ_1-norm constraint. The matrix minimization problem is as [9, 10]:

$$minimize \quad \|\boldsymbol{L}\|_* + \rho\|\boldsymbol{S}\|_1$$

$$s.t. \ \boldsymbol{L} + \boldsymbol{S} = \boldsymbol{M} \tag{2.10}$$

where $\|\cdot\|_*$ denotes the nuclear norm, $\|\cdot\|_1$ denotes the ℓ_1-norm, ρ denotes regularization parameters for sparsity. Recent advances in the proximal algorithm for convex optimization, alternating direction method of multipliers (ADMM), allow Equation (2.10) to be optimized separately for each variable with fast convergence [11]. This algorithm will be illustrated in detail in Chapter 4.3.

2.2.3 Autoencoder

Autoencoder is feed-forward neural networks with an odd number of hidden layers and shared weights between the top and bottom layers. It has been developed to learn the underlying representation of data of various attributes. It has been trained to learn low-dimensional features while minimizing the error between input data and output data [12].

A basic three-layer autoencoder with input $\boldsymbol{x}$ and hidden feature $\boldsymbol{h}$ can be expressed as:

$$\boldsymbol{h} = f_{\mathcal{E}}(\boldsymbol{x}) = g_1(\boldsymbol{W}_1\boldsymbol{x} + \boldsymbol{b}_1) \tag{2.11a}$$

$$\hat{\boldsymbol{x}} = f_{\mathcal{D}}(\boldsymbol{h}) = g_2(\boldsymbol{W_2}\boldsymbol{h} + \boldsymbol{b}_2) \tag{2.11b}$$

where $f_{\mathcal{E}}$ and $f_{\mathcal{D}}$ are encoder and decoder functions respectively. $\boldsymbol{W}_1$ and $\boldsymbol{W}_2$ are

weight matrix with the size of $r \times n$ and $n \times r$ respectively. $\boldsymbol{b}_1$ and $\boldsymbol{b}_2$ are bias vector with the size of $r \times 1$ and $n \times 1$ respectively. g's are element-wise nonlinear activation functions. The dimensionality of input $\boldsymbol{x}$ is reduced from n into r, and the low-dimensional features are represented in the bottleneck $\boldsymbol{h}$. The layer parameters for $\boldsymbol{W}_1$, $\boldsymbol{W}_2$, $\boldsymbol{b}_1$, $\boldsymbol{b}_2$ are estimated while training autoencoder to reduce the root mean squared error between input $\boldsymbol{x}$ and output $\hat{\boldsymbol{x}}$ as:

$$\underset{\boldsymbol{W}_1,\boldsymbol{W}_2,\boldsymbol{b}_1,\boldsymbol{b}_2}{\operatorname{argmin}} \frac{1}{N}\sum_{k=1}^{N}\left\|\boldsymbol{x}_k - f_{\mathcal{D}}\left(f_{\mathcal{E}}(\boldsymbol{x}_k)\right)\right\|_2^2 \tag{2.12}$$

Deep autoencoder (DAE) is constructed by stacking multiple encoding and decoding layers (Figure 2.3). The encoder and decoder functions are represented as:

$$\boldsymbol{h} = f_{\mathcal{E}}(\boldsymbol{x}) = g_L\left(\boldsymbol{W}_L \ldots g_2\left(\boldsymbol{W}_2\left(g_1(\boldsymbol{W}_1\boldsymbol{x} + \boldsymbol{b}_1)\right) + \boldsymbol{b}_2\right) \ldots \boldsymbol{b}_L\right) \tag{2.13a}$$

$$\hat{\boldsymbol{x}} = f_{\mathcal{D}}(\boldsymbol{h}) = g_{2L-1}\left(\boldsymbol{W}_{2L-1} \ldots g_{L+2}\left(\boldsymbol{W}_{L+2}\left(g_{L+1}(\boldsymbol{W}_{L+1}\boldsymbol{h} + \boldsymbol{b}_{L+1})\right) + \boldsymbol{b}_{L+2}\right) \ldots \boldsymbol{b}_{2L-1}\right) \tag{2.13b}$$

2.2.4 Robust Deep Autoencoder

rDAE is an algorithm that recovers a non-linear low-dimensional feature, $\boldsymbol{L}$, and a sparse feature, $\boldsymbol{S}$, from the data matrix, $\boldsymbol{M}$. The arbitrary corruptions do not exhibit low-dimensionality, and consequently, these features are extracted to a sparse matrix by ℓ_1-norm constraint. The matrix minimization problem is as [13]:

$$\min_{\theta_{\mathcal{D}},\theta_{\mathcal{E}},\boldsymbol{S}} \left\| \boldsymbol{L} - \mathcal{D}_{\theta_{\mathcal{D}}}\left(\mathcal{E}_{\theta_{\mathcal{E}}}(\boldsymbol{L})\right)\right\|_2 + \rho\|\mathbf{S}\|_1$$

$$\text{s.t. } \boldsymbol{M} - \boldsymbol{L} - \boldsymbol{S} = 0 \tag{2.14}$$

where $\|\cdot\|_*$ denotes the nuclear norm, $\|\cdot\|_1$ denotes the ℓ_1-norm, ρ denotes regularization parameters for sparsity. As Equation (2.14) is non-differentiable, the idea of an ADMM and Dykstra's alternating projection method are combined [11, 14]. This algorithm will be illustrated in detail in Chapter 5.3.

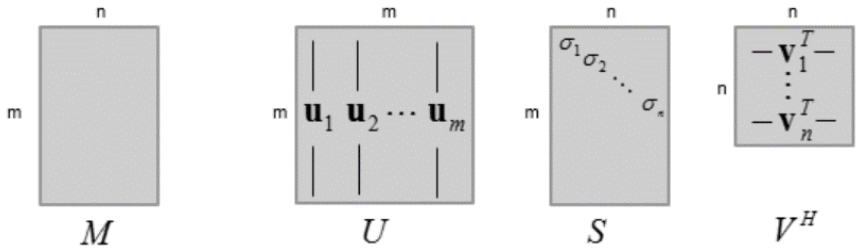

Figure 2.2. Schematic diagram of singular value decomposition (SVD) for $m > n$.

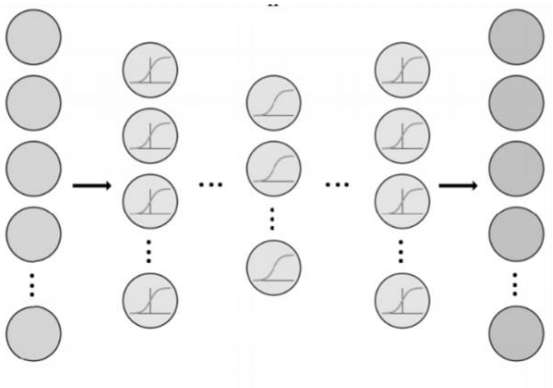

Figure 2.3. Schematic diagram of deep autoencoder (DAE).

Chapter 3

Dynamic Hyperpolarized 13C MRSI using SPICE in Mouse Kidney at 9.4T

3.1 Motivation

The development of hyperpolarized ^{13}C MRSI via dissolution dynamic nuclear polarization (DNP) has enabled the in-vivo observation of pyruvate and its products (e.g., lactate and alanine) [15]. Hyperpolarized ^{13}C spectra obtained from the kidney, liver, and prostate have been examined, and the lactate/pyruvate ratio exhibited elevated levels in tumor regions [16, 17]. Through observation of these spectra over time, the change in the metabolic state has also been demonstrated in normally fed and fasted animals [18]. Following these studies, there have been many studies on dynamic hyperpolarized ^{13}C MRSI in clinical applications including tumor investigations [19-23] and diabetes [24, 25]. However, signal levels have been a concern owing to the limited lifetimes of the hyperpolarized signals, which disappear according to their T_1 relaxation times, thus making it difficult to acquire reliable high-spatial-resolution dynamic hyperpolarized ^{13}C MRSI [26].

To overcome this limitation, fast imaging techniques such as echo-planar spectroscopic imaging (EPSI) [20], spiral CSI [27], compressed sensing [28-30], and IDEAL spiral CSI [31] have been investigated. These techniques help improve spatial and temporal resolutions in dynamic hyperpolarized ^{13}C MRSI. By contrast, as an alternative to MRSI, spectral-spatial (SPSP) excitation radio frequency (RF) pulses have been applied to dynamic hyperpolarized ^{13}C imaging [32-36]. They use spectral selective excitation by exploiting a priori knowledge of the frequency distribution to acquire high-spatial-resolution hyperpolarized ^{13}C images [32, 33].

Recently, the SPectroscopic Imaging by exploiting spatiospectral CorrElation (SPICE) technique has been developed to accelerate ^{1}H MRSI [37, 38], and it has also been applied to various nuclei (e.g., ^{13}C MRSI for single slice [39] and ^{31}P MRSI for dynamic imaging[40]). In ^{1}H MRSI, SPICE demonstrated hybrid acquisition employing CSI and EPSI segments: 1. The CSI segment acquires the 'training dataset' (D1) with high spectral resolution and relatively high signal-to-noise ratio (SNR). 2. The EPSI segment acquires the 'imaging dataset' (D2) sparsely in the spectral domain with high spatial resolution. By using the partial separability (PS) of spectroscopic signals [41, 42], subspace structures of the spectroscopic signals are exploited from the D1 dataset to generate the spectral basis functions. Afterward, high spatial resolution images are reconstructed by solving a regularized linear least-squares problem to obtain the full spectroscopic imaging dataset [43-45]. The feasibility of the SPICE technique for hyperpolarized ^{13}C MRSI has been investigated and applied to the imaging of pyruvate and lactate from mouse kidney [39].

In this study, I present a new dynamic hyperpolarized ^{13}C MRSI method using the SPICE technique. The original acquisition scheme of SPICE has been modified to the proposed method. The subspace structure exploited from the single D1 dataset is applied to subsequent D2 datasets to reconstruct dynamic hyperpolarized ^{13}C spectroscopic images. The feasibility of using a single D1 dataset has been investigated in two parts: (1) consistency of spectral basis and (2) accuracy of estimated k_{pl} (conversion constant rate from pyruvate to lactate) with regard to the dynamic frame at which the D1 dataset is acquired. The proposed acquisition scheme is implemented in an enzyme phantom experiment. Finally, dynamic ^{13}C MRSI is obtained from normal diet and high-fat diet mice using the proposed acquisition scheme.

3.2 Methods

3.2.1 Partially separable function for dynamic MRSI

A high dimensional dynamic spectroscopic signal can be represented as a partially separable function [42] as follows:

$$\rho(r, f, t) = \sum_{l=1}^{L} c_l(r, t)\varphi_l(f, t) \tag{3.1}$$

where L is the model order determined by the singular values of the D1 dataset, l is the index of the spectral basis, and $\varphi_l(f, t)$ is the spectral basis function at dynamic frame t. The spatial coefficient $c_l(\boldsymbol{r}, t)$ is the corresponding spatial coefficient for $\varphi_l(f, t)$ at

dynamic frame *t* and includes the effect of metabolism, perfusion, and T_1 relaxation [46]. The spatial coefficient $c_l(\boldsymbol{r}, t)$ varies for each dynamic frame *t*. The spectral basis function s determined according to the intrinsic characteristics of metabolites such as chemical shift (Δf). Although the time varying basis function $\varphi_l(f, t)$ should be determined for each dynamic frame *t*, it leads to impractical implementation circumstances in hyperpolarized ^{13}C situation that require scans within a finite time. Here, the time varying basis function is assumed to be consistent over the dynamic frames (i.e., $\varphi_l(f, t) \approx \varphi_l(f)$). Based on this assumption, I propose a data acquisition scheme comprising a single D1 dataset that captures the $\varphi_l(f)$ information and several D2 datasets that capture the $c_l(\boldsymbol{r}, t)$ information in each dynamic frame. To investigate the feasibility of this assumption, the consistency of the spectral basis function and the accuracy of the estimated k_{pl} were evaluated with respect to the acquisition timing of D1 dataset, at which $\varphi_l(f)$ was extracted.

3.2.2 Data acquisition and reconstruction for dynamic SPICE

Figure 3.1 shows the proposed acquisition scheme composed of 1) a single D1 dataset using a centric ordered FIDCSI sequence and 2) several D2 datasets using a centric ordered EPSI sequence with bipolar readout gradient. From the two acquired datasets, high-resolution dynamic spectroscopic images were reconstructed [42].

The B_0 field inhomogeneity effect of each dataset was compensated by a field map

acquired using ^{1}H multi-echo gradient echo sequence according to the spatial resolution of each dataset. The frequency shift in ^{1}H was scaled by γ_{13C}/γ_{1H} to set a frequency shift in ^{13}C and was corrected by using the conjugate phase method [47].

The spectral basis function set, $\Phi = \{\varphi_l(f)\}_{l=1}^{L}$, was extracted from the D1 dataset through singular value decomposition (SVD). The left singular vector was selected from the SVD of the D1 dataset as the spectral basis. The model order, L, was set to a singular number within which 95% power was maintained [42]. Consequently, the spatial coefficients at each dynamic frame, $C_t = \{c_l(\boldsymbol{r}, t)\}_{l=1}^{L}$, were estimated from the D2 dataset by solving the following minimization problem for each dynamic frame:

$$\min_{C_t} \frac{1}{2} \left\| d_{2,t} - \Omega F(\Phi C_t) \right\|_2^2 + \lambda \sum_r \| R_r(C_t) \|_* \tag{3.2}$$

where t is the dynamic frame, $d_{2,t}$ is the D2 dataset at each dynamic frame, Ω is the sampling operator in spectral dimension to fit the spectral bandwidth of the D1 and D2 datasets, F is the Fourier transform in the spatial domain, λ is the regularization constant, R_r is a locally low-rank (LLR) regularization function, which encourages the low rankness of the local regions [48], and $\|\cdot\|_*$ represents the nuclear norm [49]. Equation (3.2) was solved by the alternating direction method of multipliers (ADMM) algorithm [11]. Notably, the matrix size of Φ and C_t was $N_f \times L$ (N_f: spectral size of D1) and $L \times N_{pixel}$ (N_{pixel}: spatial size of D2) respectively.

3.2.3 Kinetic modeling for dynamic hyperpolarized 13C signal

The two-site exchange model with arterial input function (AIF) was implemented to simulate the dynamic evolution of the metabolites and evaluate the k_{pl} estimation as [20]:

$$M_{pyr}(t) = \begin{cases} \frac{rate_{inj}}{k_{pyr}}\left(1 - e^{-k_{pyr}(t-t_{arrival})}\right), & t_{arrival} \le t < t_{end} \\ M_{pyr}(t_{end})e^{-k_{pyr}(t-t_{end})}, & t \ge t_{end} \end{cases} \quad (3.3a)$$

$$M_{lac}(t) = \begin{cases} \frac{k_{pl}rate_{inj}}{k_{pyr}-k_{lac}}\left(\frac{1-e^{-k_{lac}(t-t_{arrival})}}{k_{lac}} - \frac{1-e^{-k_{pyr}(t-t_{arrival})}}{k_{pyr}}\right), & t_{arrival} \le t < t_{end} \\ \frac{M_{pyr}(t_{end})k_{pl}}{k_{pyr}-k_{lac}}\left(e^{-k_{lac}(t-t_{end})} - e^{-k_{pyr}(t-t_{end})}\right) + M_{lac}(t_{end})e^{-k_{pyr}(t-t_{end})}, & t \ge t_{end} \end{cases} \quad (3.3b)$$

where $M_{pyr}(\mathrm{t})$ and $M_{lac}(t)$ are signal evolutions of pyruvate and lactate as a function of time, respectively; k_{pyr} and k_{lac} are the decay rate constants owing to T_1 relaxation and RF excitation for pyruvate and lactate, respectively (s^{-1}); $rate_{inj}$ is the rate of pyruvate arrival (s^{-1}); $t_{arrival}$ is the time of pyruvate arrival (s) and t_{end} is the time of the maximum pyruvate signal (s); k_{pl} is the reaction rate constant from pyruvate to lactate (s^{-1}). k_{pyr} and k_{lac} were estimated as $e^{-TR/T1} \cdot \cos(\mathrm{FA})$.

Before fitting dynamic curves of dynamic SPICE, several parameters were pre-determined and assumed. First, $t_{arrival}$, t_{end}, and $rate_{inj}$ were estimated by fitting the dynamic signal evolution acquired from pre-scan to Equation 3.3a; the resulting values

were 1 s, 12 s, and 0.3 s^{-1} respectively. Second, the T1 and T2* relaxation of all metabolites were set to 40 s and 30 ms, respectively [50]. Third, the signal evolution of alanine and pyruvate-hydrate was generated by an amount of 1/5 of lactate and 1/10 of pyruvate, respectively, to imitate the various substances of in vivo circumstances.

3.2.4 Consistency of the spectral basis according to the dynamic frame

To investigate the influence of timing at which the spectral basis is collected, the spectral basis was extracted from the D1 datasets at various dynamic frames from the beginning of lactate peak (here, index of dynamic frame was from 1 to 19). The consistency between the two spectral basis function was evaluated by 'cosine similarity', which was used as a metric for the similarity between two spectra [51].

$$S_l(i,j) = \left\| \frac{\sum_f \varphi_l(f,i)\cdot\varphi_l(f,j)}{\sum_f \varphi_l(f,i)^2 \ \sum_f \varphi_l(f,j)^2} \right\| \qquad (i,j = 1,2,3,\dots,19) \tag{3.4}$$

where l is an index of the spectral basis, $\varphi_l(f,i)$ and $\varphi_l(f,j)$ denote an l^{th} spectral basis at the i^{th} and j^{th} dynamic frames, respectively, $\|\cdot\|$ denotes the Euclidian norm for complex vector ($\sqrt{x^* \cdot x}$) [51]. Notably, the 1st dynamic frame indicates the timing at which the lactate signal is maximum (here, 18 s after the beginning of metabolite exchange) and the interval of each dynamic frame is 0.96, which is the same as that of the acquisition time for a single D1 dataset. Note that S_l was evaluated for $l = 1,2,\dots,\mathrm{L}$. A value close

to 1 indicates high similarity (i.e., most consistent) and a value near 0 indicates low similarity (i.e., less consistent) between the spectral basis.

In the simulation, the D1 datasets were generated repeatedly during 19 dynamic frames considering signal decay due to T_1 relaxation, RF excitation, and metabolite conversion rate (k_{pl}). A numerical vial phantom composed of 7 vials with different k_{pl} was designed (Figure 3.1a). The k_{pl} of each vial was set to [0.002:0.004:0.026], respectively. All the D1 datasets were generated assuming a spatial matrix size = 4x4 with 16 phase encodings, spectral size = 320 points, spectral bandwidth = 6000 Hz, FA = 10°. Gaussian noise was added such that the peak SNR of pyruvate was 300 in the reconstructed spectrum of the D1 dataset at the first dynamic frame. The level of SNR was determined with reference to *in-vivo* experiment. Notably, only D1 datasets were utilized to investigate the consistency of the spectral basis.

In the *in-vivo* experiment, D1 datasets were continuously acquired from an ND mouse using a centric ordered FIDCSI sequence from 19 dynamic frames. The imaging parameters were a spatial matrix size = 4 × 4, number of phase encoding = 16, TE/TR = 3.5/60 ms, FOV = 35 × 35 mm^2, slice thickness = 8.5 mm, FA = 10°, and spectral bandwidth = 6009.6 Hz. The data acquisition commenced 18 s following the start of injection of 350 μL hyperpolarized ^{13}C pyruvate substrate (pH = 7.2, polarization level = 15.4%, 79 mM).

3.2.5 Effect of transition of spectral basis on k_{pl} estimation

To investigate the effect of transition of spectral basis on the accuracy of k_{pl} estimation, the spectral bases were estimated from D1 datasets in various situations. All the simulations were conducted in a series of Monte-Carlo simulations (300 repetitions). A numerical vial phantom composed of seven vials with different k_{pl} (0.002:0.004:0.026) (Figure 3.1a) was designed.

First, the effect of a dynamic frame from a D1 dataset on the estimated k_{pl} was investigated. D1 datasets were generated similarly to those in the aforementioned simulation. D2 datasets were generated repeatedly in a similar way to the D1 datasets assuming a spatial size (N_{pixel}) = 32 × 32, spectral size (N_f) = 160 points, and spectral bandwidth = 6000 Hz (here, nine D2 datasets were generated). Gaussian noise was added so that the peak SNR of pyruvate was 150 in the reconstructed spectrum of the D2 dataset in the first dynamic frame. The SNR was determined with reference to the *in-vivo* experiment. The D1 dataset of each dynamic frame (from 1 to 19) was used to reconstruct the spatial coefficients from the D2 datasets. Note that a single D1 dataset and nine D2 datasets were used to reconstruct the spectral-spatial-temporal MRSI data, which were used to generate a k_{pl} map. The estimated k_{pl} and the cosine similarity of spectral basis were evaluated at the same dynamic frame. Additionally, to investigate whether the acquisition of a D1 dataset during the injection (i.e., upslope) period influences k_{pl} estimation, a D1 dataset was acquired during this period.

Second, the effect of spatial resolution of the D1 dataset on the estimated k_{pl} was investigated. In addition to vial phantom, a numerical anatomical kidney phantom was designed considering the hyperpolarized ^{13}C situation in which a few of the whole FOV showed signal. A phantom was composed of three types of tissues with different k_{pl} (0.018, 0.014, and 0.026 for modeling cortex, medullar, and vascular tissues, respectively). D1 datasets were generated similarly to those in the aforementioned simulation and only the spatial size (N_{pixel}) was varied from 4 × 4 to 32 × 32. Note that the same D2 datasets of the aforementioned simulation were used.

3.2.6 Enzyme phantom experiment

Phantom experiments were conducted to verify the feasibility of estimating k_{pl} using the proposed dynamic SPICE. For this purpose, the estimated k_{pl} map from dynamic SPICE was compared with the k_{pl} value estimated from unlocalized spectroscopy. The enzyme phantom was composed of one 15 ml Falcon tube filled with five-fold concentrated phosphate buffered saline at 14 ml, nicotinamide adenine dinucleotide (NADH) at 4.4 mM (Sigma-Aldrich, Gillingham, UK), and L-Lactate Dehydrogenase (LDH) extracted from rabbit muscle at 120 U (Sigma-Aldrich, Gillingham, UK) [52]. 1 ml of the hyperpolarized ^{13}C pyruvate solution was injected through a line with an inner/outer diameter of 0.28/0.61 mm. A T_2 weighted proton image was acquired with a rapid acquisition with relaxation enhancement (RARE) system with a RARE factor = 4, TE/TR = 22/3000 ms, FOV = 40 ×

40 mm^2, and in-plane resolution = 0.31 × 0.31 mm^2. Subsequently, hyperpolarized ^{13}C MRSIs were acquired using slice-selective RF excitation pulses.

For unlocalized spectroscopy, the signal was obtained from the FOV in dynamic SPICE without spatial encoding. The acquisition parameters were set as follows: spectral bandwidth = 6009.6 Hz, FID points = 320, scan time = 120 s, TR = 1000 ms, FOV = 40 × 40 mm^2, and flip angle = 10°. The data acquisition commenced before the injection of 1 ml hyperpolarized 13C substrate (pH = 7.2, polarization level = 18.6%) and the lactate peak was represented at 24 s after injection.

For dynamic SPICE, the imaging parameters for D1 (FIDCSI) and D2 (EPSI) were set as follows: 1. D1 dataset: spatial matrix size = 4 × 4, phase encoding for CSI = 16, spectral bandwidth = 6009.6 Hz, FID points (N_f) = 320, and scan time = 0.96 s. 2. D2 dataset: spatial matrix size (N_{pixel}) = 32 × 32, phase encoding number = 32, sampling bandwidth = 96.15 kHz, spectral points (echo train length) = 64, and scan time = 17.28 s. D2 datasets were acquired for nine dynamic frames; the time interval between each dynamic frame was 1.92 s. The total acquisition time was 18.24 s, TE/TR = 3.5/60 ms, FOV = 40 × 40 mm^2, and flip angle = 10°. Data acquisition commenced 18 s following the start of injection of 1 ml hyperpolarized pyruvate substrate (pH = 7.2, polarization level = 17.6%). The scan for dynamic SPICE started 24 s after injection based on the dynamic signal evolution in unlocalized spectroscopy.

3.2.7 Animal experiments of two groups: mice following a normal diet and mice following a high-fat diet

Animal studies were conducted using two different experimental groups: ND mice (n = 3) and HFD mice (n = 3). A high metabolic activity was expected owing to the diabetic condition of the HFD mice because long exposure to hyperglycemia has been regarded as a factor that can induce kidney disease[9]. These animal sets have been used for the study of the metabolism of the mouse brain[39]. All imaging parameters were the same as the enzyme phantom experiment described above except for FOV and slice thickness (= 8.5 mm). The FOV of ND mice and HFD mice was determined to cover their entire body without aliasing (35×35 mm^2 and 40×40 mm^2 for ND mice and HFD mice, respectively). In advance to dynamic SPICE acquisition, pre-scan was executed using unlocalized spectroscopy as phantom experiment and the lactate peak was represented at 18 s after injection (Figure 3.1c). Dynamic SPICE acquisition commenced 18 s following the start of injection of 350 μL hyperpolarized pyruvate substrate (pH = 7.2, polarization level = 16.5%, 79 mM). The pyruvate peak map and the lactate peak map were obtained for seven dynamic frames with an in-plane resolution of 1.09×1.09 mm^2 and 1.25×1.25 mm^2 for ND mice and HFD mice, respectively. The ROI was manually segmented for three types of tissues (vascular, medullar, and cortical tissues) based on the T_2 weighted proton image. Student t-test was used to compare the two groups for each ROI, respectively. The mean and standard deviation of k_{pl} in each group were calculated.

Male ICR mice (30–35 g, seven weeks old) were purchased from Japan SLC, a branch of Charles River Laboratories (Shizuoka, Japan). Mice were fed either a ND (PicoLab, 13.1 kcal % fat) or HFD (Research Diet INC., 60.0% kcal fat) for 12 weeks and 24 weeks. The body weights of the ND mice and HFD mice were 53.5 ± 3.41 g and 78.58 ± 4.34 g, respectively. The fasting blood glucose (FBG) levels of ND and HFD were measured as 141.5 ± 5.91 mg/dL and 285.6 ± 38.02 mg/dL respectively. All animal procedures were approved by the Institutional Animal Care and Use Committee of Yonsei University College of Medicine (IACUC No.2015-0039). All experiments were conducted in accordance with the relevant guidelines and regulations.

3.2.8 Hardware and Polarization Procedure

Phantom and in-vivo experiments were conducted on a 9.4 T Bruker BioSpec 94/20 small animal imaging MRI scanner (Bruker Biospin MRI GmbH, Ettlingen, Germany) equipped with a $^{1}H/^{13}C$ dual-tuned single-channel transmit/receive coil with an inner diameter of 72 mm. Hyperpolarized ^{13}C pyruvate was produced using the HyperSense DNP polarizer (Oxford Instruments Molecular Biotools Ltd, Abingdon, UK). The polarization levels were estimated at the beginning of injection. For ^{13}C transmit gain calibration, an 8 M ^{13}C urea syringe phantom was placed near the phantom and mouse body. Post-processing was implemented in MATLAB (MathWorks, Natick, MA).

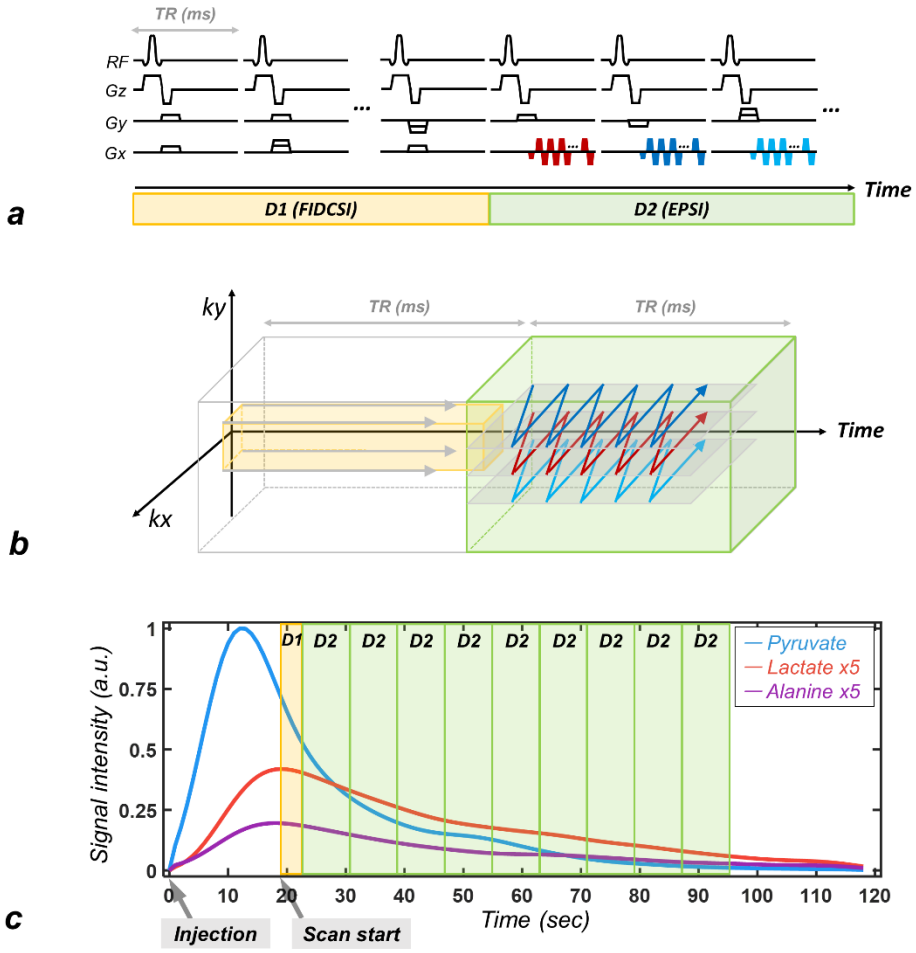

Figure 3.1. Proposed acquisition scheme of hyperpolarized 13C dynamic SPICE. (a) Two components of the pulse sequence: The D1 dataset is acquired using centric ordered FIDCSI and the D2 dataset is acquired using EPSI with a bipolar gradient during dynamic frames. (b) Sampling trajectories of D1 dataset and D2 dataset. For EPSI, the readout direction is the kx-axis and the phase-encoding direction is the ky-axis with centric order. (c) Signal evolution of metabolites acquired from unlocalized spectroscopy and corresponding acquisition timing of datasets.

3.3 Results

3.3.1 Simulations

Figure 3.2 shows the results for the consistency of spectral basis (φ_l) over time for the simulation and in vivo experiment. In the simulation, the model order, L, was determined to be 2 based on the power of singular values of the D1 dataset (Figure 3.2a). Without noise, the cosine similarity of φ_1 and φ_2 exceeded 0.95 throughout the dynamic frames. However, as noise was added, the cosine similarity of φ_2 decreased to 0 at the 19th frame, while that of φ_1 exceeded 0.90 (Figure 3.2b). This supports the fact that the reduction of cosine similarity derives from the noise. The spectrogram of φ_l shows the noise robustness of φ_1 and noise sensitivity of φ_2 according to dynamic frames (Figure 3.2c). This indicates that noise becomes prevalent when the spectral basis functions are extracted at the later dynamic frame; correspondingly, the cosine similarity becomes smaller. In the *in-vivo* experiment, the model order, L, was determined to be 3 based on the power of singular values of the D1 dataset (Figure 3.2e). The cosine similarities of φ_2 and φ_3 decreased to 0.5 and 0, respectively, at the 19th frame, while the cosine similarity of φ_1 exceeded 0.90 (Figure 3.2f). The noise sensitivity became prominent when the spectral basis functions were extracted at the later dynamic frame.

Figure 3.3 shows the effect of acquisition timing of the D1 dataset on the accuracy of the estimated k_{pl}. Each acquisition timing corresponds to a dynamic frame. For early dynamic

frame (1~10), the error of the estimated k_{pl} was within 5 % as the cosine similarity over 0.85 and noise std under 0.1. After the 11th dynamic frame, the estimated k_{pl} was increasingly overestimated as cosine similarity reduced and noise std increased. The overestimation was substantial for low k_{pl}. For the D1 dataset acquired before the lactate peak (i.e., at dynamic frames -7 to -1), k_{pl} was underestimated (Figure 3.4). Figure 3.5 shows the effect of the spatial resolution of the D1 dataset on the accuracy of the estimated k_{pl}. Regardless of the spatial resolution of the D1 dataset, the error of the estimated k_{pl} was consistent within 5% (Figure 3.5b and 3.5d).

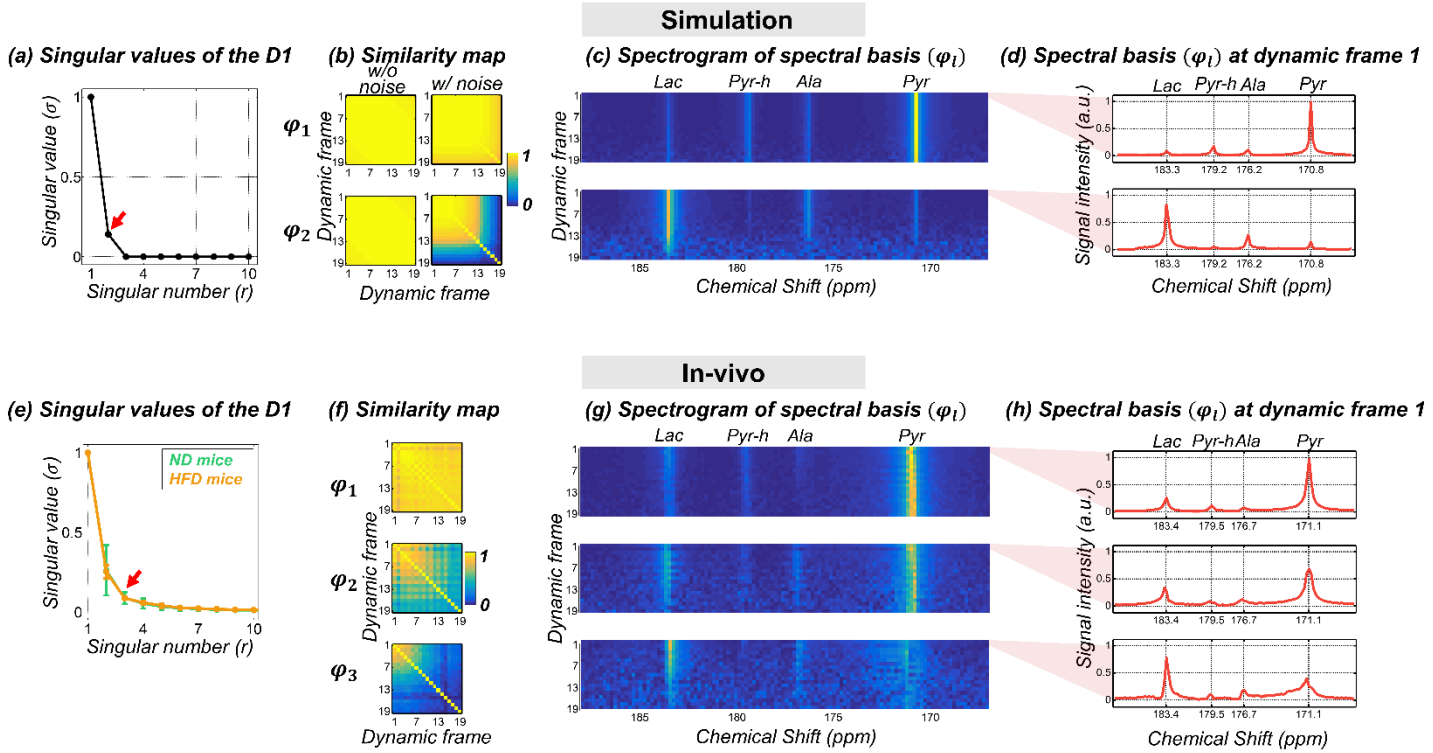
Simulation
(a) Singular values of the D1
(b) Similarity map
(c) Spectrogram of spectral basis (φ_l)
(d) Spectral basis (φ_l) at dynamic frame 1
Singular value (σ)
Singular number (r)
w/o noise
w/ noise
φ_1
φ_2
Dynamic frame
Lac
Pyr-h
Ala
Pyr
Chemical Shift (ppm)
Signal intensity (a.u.)
183.3
179.2
176.2
170.8
In-vivo
(e) Singular values of the D1
(f) Similarity map
(g) Spectrogram of spectral basis (φ_l)
(h) Spectral basis (φ_l) at dynamic frame 1
ND mice
HFD mice
φ_3
183.4
179.5
176.7
171.1

Figure 3.2. Consistency analysis for spectral basis according to the dynamic frame (a-d: simulation, e-h: in-vivo). (a) Singular values of the D1 dataset, (b) cosine similarity with noise and without noise for φ_1 and φ_2, (c) Spectrogram of φ_1 and φ_2 with regard to dynamic frames, and (d) Spectral distribution of φ_1 and φ_2 at dynamic frame 1. (e) Rank of the D1 dataset, (f) Cosine similarity for φ_1, φ_2, and φ_3, (g) Spectrogram of φ_1, φ_2, and φ_3 with regard to dynamic frames, and (h) Spectral distribution of φ_1, φ_2, and φ_3 at dynamic frame 1.

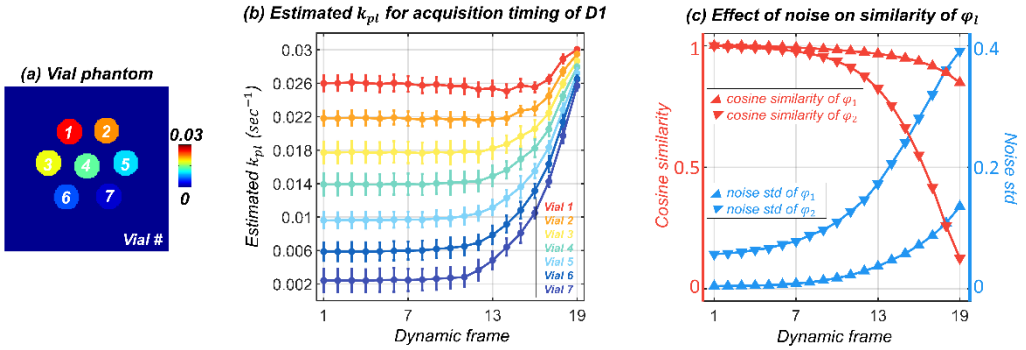

Figure 3.3. Effect of dynamic frame of D1 dataset on accuracy of k_{pl} estimation. (a) Numerical phantom composed of seven vials. The k_{pl} of each vial was set from 0.002 to 0.026 with a step size of 0.004. (b) Estimated k_{pl} of each vial and (c) Standard deviation of noise and cosine similarity according to the dynamic frame from which the D1 dataset was extracted.

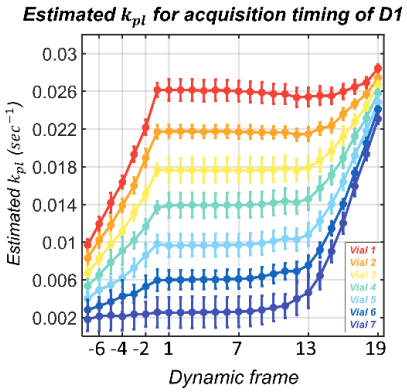

Figure 3.4. Effect of the acquisition timing of the D1 dataset on the estimated k_{pl}. The true k_{pl} values for vial 1 to vial 7 are 0.026 to 0.002 with step size of 0.004, which is depicted in the left vertical axis. Note that the index of dynamic frame -1 to -7 indicate 1 sec to 7 sec before the maximum lactate signal.

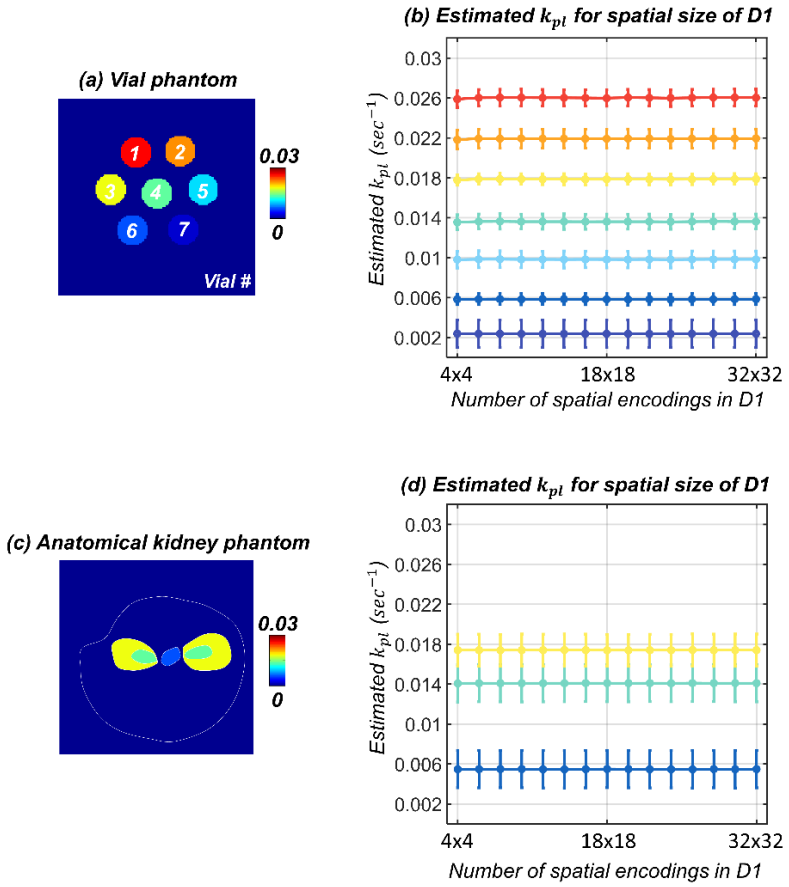

Figure 3.5. Effect of spatial resolution of the D1 dataset on the estimated k_{pl}. (a) Numerical phantom composed of seven vials. The k_{pl} of each vial was set from 0.002 to 0.026 with a step size of 0.004. (b) Estimated k_{pl} of each vial according to the spatial resolution of the D1 dataset. (c) Simplified numerical phantom representing the kidney. The k_{pl} of each tissue was set to 0.006 (vasculature), 0.014 (medulla), and 0.018 (cortex). (d) Estimated k_{pl} of each tissue according to the spatial resolution of the D1 dataset.

3.3.2 Phantom experiment

Figure 3.6 shows the results of dynamic SPICE imaging for the enzyme phantom experiment. The pyruvate and lactate peak maps are presented in representative dynamic frames (Figure 3.6d). The k_{pl} map was measured uniformly (Figure 3.6b), and the mean and standard deviation of the k_{pl} map of the given ROI (black line in Figure 3.6b) was 0.0113 ± 0.0019. Regions outside of the ROI were excluded due to the turbulence effects during the injection of the pyruvate solution. Nevertheless, these regions also showed relatively homogeneous k_{pl} values as compared to the heterogeneous metabolite maps. The estimated k_{pl} map from dynamic SPICE showed approximately 10% overestimation compared to the measurement using unlocalized spectroscopy (k_{pl} = 0.0103).

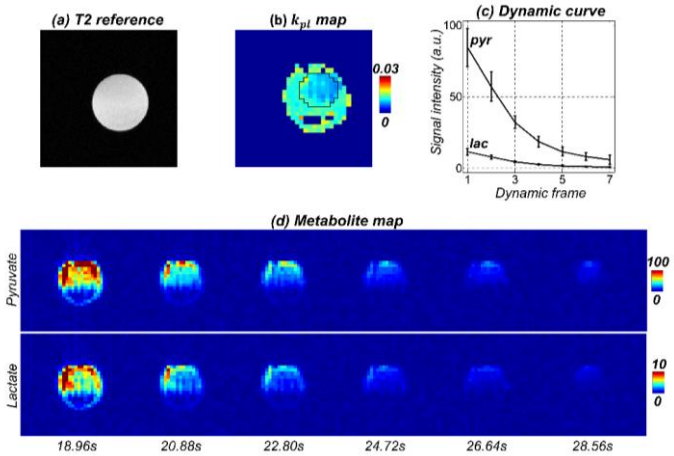

Figure 3.6. In vitro enzyme phantom experiment. (a) T2 reference image. (b) Estimated k_{pl} map. (c) Time course of metabolites from unlocalized spectroscopy during 7 dynamic frames. The signal intensity of metabolites inside the black line of the k_{pl} map was averaged. (d) Metabolite map of pyruvate and lactate at each dynamic frame.

3.3.3 In-vivo experiment

Figure 3.7 shows the results for the ND and HFD mouse kidney using the proposed acquisition scheme. Representative metabolite maps and the k_{pl} map for ND mouse are provided in Figure 3.7a and Figure 3.7c respectively. The estimated k_{pl} was approximately 0.01 throughout the kidney, including the cortex and medulla, while it was 0.007 in the vasculature region. The spectrum of the three representative voxels provided in Figure 3.7d shows high SNR even at the 3rd dynamic frame. Representative metabolite maps and the k_{pl} map for the HFD mouse are provided in Figure 3.8a and Figure 3.8c, respectively. The pyruvate map shows a higher value in the cortex than in the medulla, while the lactate map shows a similar value throughout the kidney (Figure 3.8a). This is represented in the k_{pl} map. The estimated k_{pl} was approximately 0.02 at the medulla, 0.017 at the cortex, and 0.011 at the vasculature (Figure 3.8c). The spectrum from the 3rd dynamic frame is shown in Figure 3.8d. The generation of alanine in the medullar and cortex was observed (red arrow in Figure 3.8d), which was not the case for the ND mouse. Table 3.1 shows the ROI analysis of the k_{pl} map for the ND and HFD mice. The averaged k_{pl} was higher in the HFD mice than in the ND mice for the three ROIs. The difference in the two groups was significant in the medulla (p value<0.05), but non-significant in the vasculature.

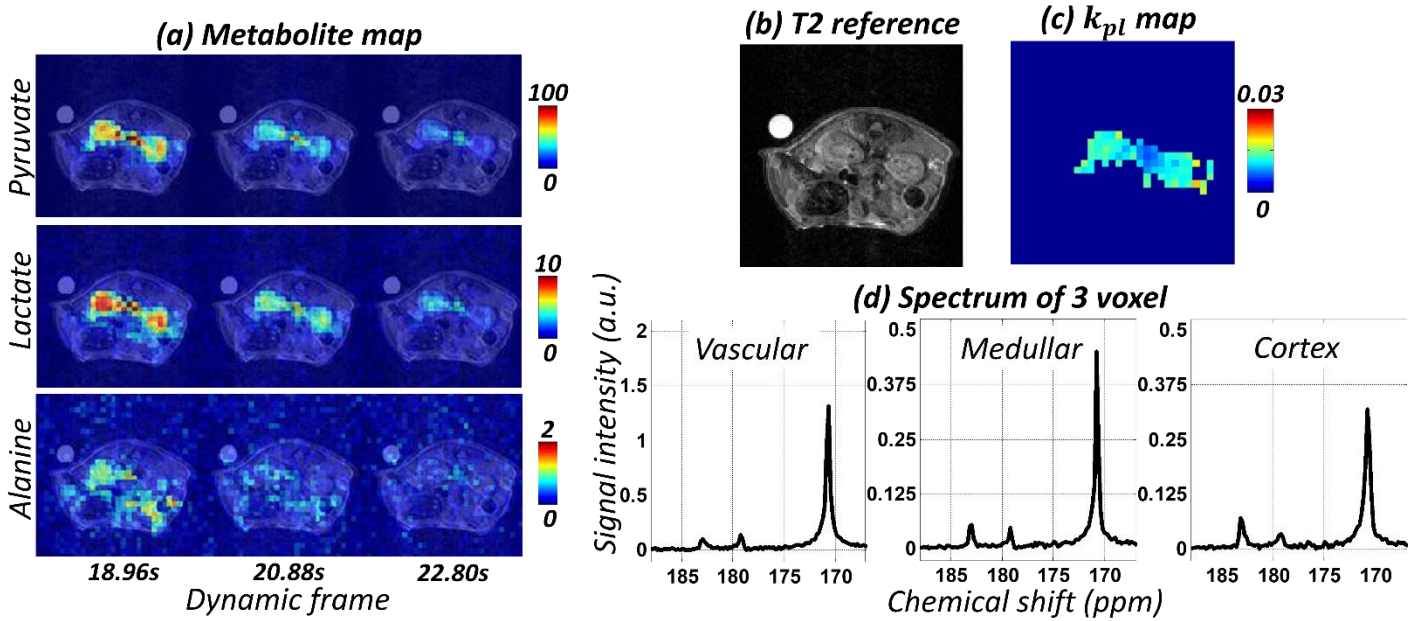

Figure 3.7. In-vivo experiment of ND mouse overlayed to the T2 reference image. (a) Metabolite map of pyruvate, lactate, and alanine in the dynamic frame. (b) T2 reference image of ND mouse. (c) Estimated k_{pl} map. (d) Spectrum of vascular, medullar, and cortical regions at the 3rd dynamic frame.

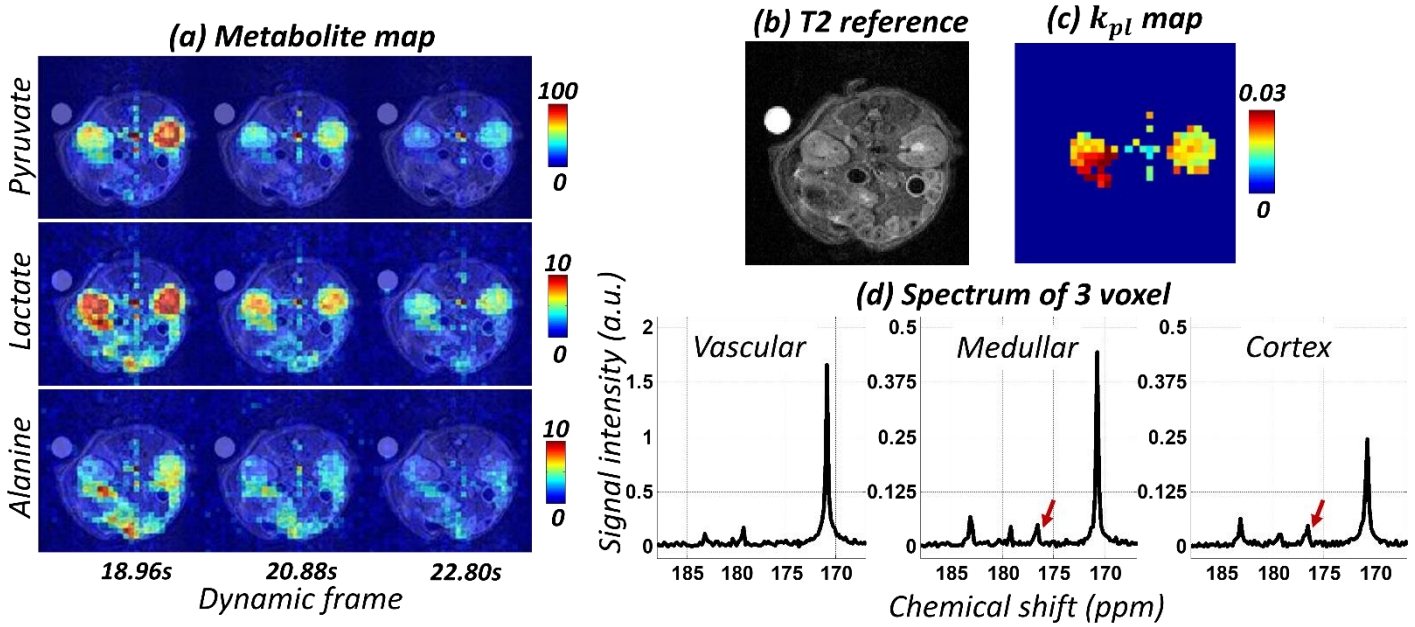

Figure 3.8. In-vivo experiment of HFD mouse overlayed to the T2 reference image. (a) Metabolite map of pyruvate, lactate, and alanine in the dynamic frame. (b) T2 reference image of HFD mouse. (c) Estimated k_{pl} map. (d) Spectrum of vascular, medullar, and cortical regions at the 3rd dynamic frame.

	Vasculature	Medulla	Cortex
ND (n=3)	0.0087±0.0013	**0.0119±0.0022***	0.0148±0.0023
HFD (n=3)	0.0132±0.0050	**0.0195±0.0005***	0.0224±0.0054

* $p < 0.05$

Table 3.1. ROI analysis of k_{pl} (s-1) map for ND and HFD mice.

3.4 Discussion

The purpose of this study was to investigate the feasibility of dynamic hyperpolarized ^{13}C MRSI using the SPICE technique and to estimate the conversion constant rate k_{pl}.

In the model of the partially separable function, the model order determines the degrees of spectral variations of the D1 dataset. Theoretically, to extract the spectral basis through SVD, the spectral-spatial matrix of size $N_t \times N_{kxky}$ has to satisfy $N_t > L$ and $N_{kxky} > L$ [42]. In this study, the model order of simulation was consistent at 2 regardless of the extent of spatial frequencies, while that of the *in-vivo* experiments varied from 3 to 5. This is because φ_1 and φ_2 are decomposed as different bases, although the dominant peaks such as pyruvate are identical (Figure 3.2h). Effects such as B_0 inhomogeneity cause these differences. Moreover, an additional basis could be extracted when large amounts of other metabolites were produced (e.g., alanine or bicarbonate). Although the bicarbonate peak was not observed in this study owing to limited signal power [53], the SNR improvements in both D1 and D2 might detect low-power signals at the expense of low spatial resolution.

Here, the size of the D1 dataset in the spatial dimension was 4×4 based on the observation of singular values. This has to be considered experimentally and optimized according to the spectral-spatial composition of the target.

The reliability of using the basis extracted from a single time point − in our case, at the maximum lactate signal− has been demonstrated in two parts: 1) by showing the consistency of the spectral basis over time and 2) by evaluating the accuracy of k_{pl} according to various dynamic frames. The consistency of the spectral basis over time was maintained during several dynamic frames despite T_1 relaxation, RF excitation, and metabolic conversion effects. This indicates that the acquisition timing of the D1 dataset does not significantly affect the subspace structure of the spectral basis. However, the consistency was disrupted with the reduction of SNR. The effect of noise was prominent as the singular number (i.e., index of spectral basis) increased. This was due to the characteristic of SVD, whereby the denoising effect on the basis component became weaker as the singular number increased. The collapse of the consistency owing to the SNR decrease deviated the accuracy of the estimated k_{pl} (Figure 3.3b - 3.3c). It was also shown that if the acquisition begins before the sub-metabolite peak (here, the lactate peak), i.e., during the upslope period, then k_{pl} is incorrectly estimated (Figure 3.4). For this period, the amount of conversion from the substrate to sub-metabolite is insufficient, resulting in misdetection of the spectral basis. This supports the fact that the acquisition of a spectral basis with high SNR is optimal for dynamic hyperpolarized ^{13}C MRSI.

The spatial resolution in a single dynamic frame was acquired at 1.09×1.09 mm^2 and 1.25×1.25 mm^2 for ND mice and HFD mice respectively. Note that the FOV of each mouse was determined as the range including the entire body in the axial slice. Although it was difficult to distinguish the anatomic structure of the cortex and medulla in the k_{pl} map, the k_{pl} value of HFD mice was higher than that of ND mice throughout the kidney. It has been reported that almost 90 % of the filtered glucose is reabsorbed into the kidney cortex via sodium-glucose cotransporter type 2 (SGLT-2) and the remaining glucose is reabsorbed by the medulla via SGLT-1 [54]. However, hyperglycemia in blood leads to higher glucose in urine, increasing the absorption of glucose in the kidney[55]. Along with previous hyperpolarized ^{13}C studies in the kidney of the diabetic rats [24, 25], our results show that increased glucose load in the kidney by hyperglycemia leads to higher hyperpolarized ^{13}C lactate conversion (Table 3.1).

In the enzyme phantom experiment, the beginning of the scan for dynamic SPICE was determined based on unlocalized spectroscopy and the resulting k_{pl} values were rather free from bias owing to the inadequate acquisition timing of the D1 dataset. Nevertheless, the estimated k_{pl} map from dynamic SPICE showed approximately 10 % overestimation compared to the measurement using unlocalized spectroscopy. The difference seems to derive from the unevenly mixed substrate in the vial phantom. Although the k_{pl} map exhibits a homogeneous distribution, the metabolite maps shows a more inhomogeneous distribution. As future work, more elaborate phantom experiments to improve the accuracy of k_{pl} estimation should be conducted.

The chemical shift slice-offset between pyruvate and lactate was 1.66 mm for all experiments (using a 440mT/m gradient system). The displacement was less than 5 % and 20 % of slice thickness in phantom and in-vivo experiment respectively. As chemical shift offset is a classical problem in CSI, and there have been many ways to reduce it this by using high BW radiofrequency pulses such as adiabatic pulses [56, 57].

In dynamic SPICE, a FIDCSI (i.e., D1 dataset) with limited spatial frequency was acquired to extract the spectral basis. The extracted spectral basis did not comprise a single metabolite peak but comprised several metabolites with different peak values. The possibility of an artificial spectral basis composed of a single metabolite peak has been investigated and it was demonstrated that they could not function as spectral base. This implies that the spectral basis cannot be generated using only prior knowledge of the spectral distribution such as peak positions. Here, the spectral basis was extracted from the D1 dataset based on a data-driven approach.

A similar approach to SPICE MRSI is IDEAL-CSI, where spectral prior knowledge is acquired from a slice-selective region at the beginning of the acquisition scheme [31]. This spectral prior knowledge is utilized to localize the chemical shift resonance frequencies and to precondition the chemical shift encoding matrix. As dynamic SPICE acquires the D1 dataset using a FIDCSI to extract the spectral basis with high SNR, there is an advantage of SNR [37, 38]. The limitation of proposed method is the absence of the upslope curve. Due to the difficulty of sequence modification, all the D2 datasets were acquired after the acquisition of D1 datasets. As the scan started when lactate was maximum, the upslope

curve could not be acquired (Figure 3.1c). In this study, as an alternative, several parameters (such as $t_{arrival}$, t_{end}, $rate_{inj}$, and T1) for dynamic curve fitting were estimated from pre-scan. Further improvement can be expected where the acquisition scheme interleaves with a '(several D2) – (single D1) – (again several D2)' scheme.

As a future work, first, D1 acquisition can be modified to improve the accuracy of k_{pl} estimation. This is a problem with many ^{13}C studies, where acquisition tries to sample the center regions of the k-space with the highest SNR. A similar problem has arisen in this study as well. As seen in Figure 3.4, acquiring D1 too early leads to inaccurate k_{pl} estimation. Therefore, prolonging the beginning of the acquisition seems to be beneficial at the expense of SNR. A radial D1 acquisition with golden angle sampling might be beneficial in determining the timing more accurately and the SNR. Second, alternative kinetic models can be implemented [53, 58]. Here, the consistency of a single basis and the accuracy of k_{pl} estimation were demonstrated for the two-site exchange model. It will be effective in other dynamic models because the extracted spectral bases are affected by noise (Figure 3.2) and not by the dynamic variation of metabolite concentration. Lastly, reordering of the D1 and D2 elements, or even interleaving them could result in better k_{pl} estimations. By doing so, I can also acquire data from the upslope curve of the dynamics, which has been missed in the present implementation. In our current implementation, pulse sequence design options limited the implementation of such capabilities. I had to resort to the D1 followed by D2 acquisition ordering step. In future work, I expect more flexibility in pulse sequence design to perform alternative acquisition timing options.

3.5 Conclusion

In conclusion, I have developed a SPICE-based technique to acquire dynamic hyperpolarized ^{13}C MRSI with high spatial-spectral-temporal resolution. The feasibility of the proposed method was investigated in simulation and *in-vivo*. The k_{pl} map was estimated with an error of less than 10 % through an enzyme phantom experiment. Dynamic MR spectroscopic images were acquired from ND mice and HFD mice and k_{pl} values were estimated. The estimated k_{pl} map from two animal sets presents a reliable difference in the medullar region. The modification of D2 acquisition will be part of future work to improve the spatial resolution.

Chapter 4

Blind Source Separation for Myelin Water Fraction Mapping using Multi-echo Gradient Echo Imaging

4.1 Motivation

4.1.1 Overview

In conventional myelin water imaging (MWI), spin-echo (SE) images (referred here as 'SE-MWI') are acquired at multiple echoes to measure signal decay due to T2 relaxation [59]. In white matter of the brain, it has been demonstrated that this signal has multiple T2 components e.g., myelin water and axonal/extracellular water. In order to separate these multiple signal sources, the measured signal is fitted to numerical models representing multi-exponential T2 relaxation [59, 60]. This allows the separation of fast-decaying myelin water signal (i.e., short T2 component) and slow-decaying axonal/extracellular water signal (i.e., long T2 component). Myelin water fraction (MWF) is then estimated as the ratio of the fast-decaying water signal to the total water signal.

In recent studies, multi-echo gradient recalled echo (mGRE) based MWI (referred here as 'GRE-MWI') has been suggested to separate multi-exponential T2* components [61-64]. These studies have demonstrated that the mGRE signal can also be separated into multiple components mentioned above. Furthermore, GRE-MWI has potential benefits such as large volume coverage, fast scan time and insensitivity to the inhomogeneity of the transmit field compared to SE-MWI. Despite these advantages, however, GRE-MWI suffers from imaging artifacts (e.g. voxel spread function (VSF) effect [65, 66] and physiological noise [67]) which render the mGRE signal to deviate from the pre-assumed numerical model (e.g. multi-component exponential curves or three component exponential curves). Also, the conventional optimization algorithm to solve multi-component exponential curves which is a nonlinear least squares algorithm, has instability problems regarding initial value selection and local minima [68].

Previously, blind source separation (BSS) techniques have been suggested to separate sources of the MR signal without any explicit model or with minimum prior information [69, 70]. Instead of using numerical models, BSS techniques utilize data-driven properties such as "low rankness" or "sparsity". This allows separating specific signals (e.g. pulsation artifacts in fMRI [69], free water in DWI [71]) that are difficult to specify a numerical model. Among various BSS algorithms, robust principal component analysis (rPCA) has been introduced for separation of background signal in dynamic MRI [72], on/off-resonance signal representation in multispectral imaging [73] and elimination of MR artifacts [74, 75]. Based on singular value decomposition (SVD) analysis, rPCA extracts

redundant signal sources using low-rank property (or fixed-rank property) and encourages the sparsity of the residual signal.

In this study, as an alternative to conventional nonlinear least squares approach, a modified version of rPCA is developed for signal separation in mGRE targeted for MWF mapping. The proposed technique separates mGRE images into two unit-rank components (referred to as L1 and L2) and sparse component (referred to as S). In this process, matrix hankelization and non-negative matrix factorization (NMF) are utilized to further enhance the separation of multi-component exponential signals. This offers L1, L2, and S to represent slow-decaying, fast-decaying and artifact components, respectively. An alternative MWF map is suggested as the ratio of L2 to sum of L1 and L2. The proposed technique is demonstrated in healthy volunteers and clinical patients.

The rest of this chapter is as follows. In Chapter 4.1.2 and 4.1.3, the conventional model-based GRE-MWI methods are introduced and the motivation of SVD analysis for the mGRE signal is described. In Chapter 4.2, the modification version of rPCA algorithm is described. The methods and results of the simulation and in-vivo experiments are described in Chapter 4.3 and 4.4, respectively. Finally, Chapter 4.5 contains the discussion and conclusion.

4.1.2 Model-based MWF mapping

The multi-component magnitude model fits the decay curve to the following [76]:

$$S(t) = \sum_{j=1}^{M} A_j e^{-(1/T_{2,j}^*)t} \quad (4.1)$$

where $S(t)$ is the measured signal at time t, A_j is the unknown amplitude of the spectral component with relaxation time $T_{2,j}^*$, M is the number of T_2^* components. Equation (4.1) is typically solved by regularized non-negative least squares (rNNLS) forming a continuous spectral distribution of T_2^* components [76]. Then, the myelin water component (i.e., fast-decaying signal) and axonal/extracellular water component (i.e., slowly-decaying signal) are separated based on a cutoff T_2^* (e.g. 25ms) value [77, 78].

The three-component magnitude model fits the decay curve to the following:

$$S(t) = A_{my} e^{-(1/T_{2,my}^*)t} + A_{ax} e^{-(1/T_{2,ax}^*)t} + A_{ex} e^{-(1/T_{2,ex}^*)t} \quad (4.2)$$

where $A_{my}, A_{ax}\ and\ A_{ex}$ are the amplitude of the three water components, $T_{2,my}^*, T_{2,ax}^*$ and $T_{2,ex}^*$ are T_2^* values of the three water components [61, 78].

Lastly, the three-component complex model fits the decay curve to the following [63]:

$$S(t) = (A_{my} e^{-(1/T_{2,my}^* + i2\pi\Delta f_{bg+my})t} + A_{ax} e^{-(1/T_{2,ax}^* + i2\pi\Delta f_{bg+ax})t}$$

$$+ A_{ex} e^{-(1/T_{2,ex}^* + i2\pi\Delta f_{bg+ex})t}) e^{-i\varphi_0} \quad (4.3)$$

where $\Delta f_{bg+my}, \Delta f_{bg+ax}$ and Δf_{bg+ex} are the frequency offset of the three water components plus the sum of background frequency offset, φ_0 is the B_1^+ phase offset.

For the three-component models, Eqs (2) and (3), the parameters are estimated by

minimizing the least-squares errors using an iterative nonlinear curve-fitting algorithm [63, 68, 78]. The MWF can be calculated by dividing the myelin water component (i.e., fast-decaying signal) to the total water component. In this approach, the initial values and bounds of the fitting parameters need to be set to avoid getting trapped in local minima (e.g. see [79]).

4.1.3 BSS in mGRE images

I denote matrices by boldface uppercase letters, operators by lightface uppercase letters, vectors by boldface lowercase italics, constants by lightface uppercase italics. $\mathbb{C}$, $\mathbb{R}$ and $\mathbb{R}_+$ represent a set of complex, real and positive-real values, respectively.

Among the various BSS methods, SVD analysis can be performed on the magnitude of mGRE data to separate source signals without any constraint of the signal such as the predetermined model and initial/boundary values.

In order to apply standard SVD, the mGRE data, $m(\cdot)$ is represented to the spatio-temporal Casorati matrix as follows:

$$\mathbf{M}(\boldsymbol{r}, t) = \begin{bmatrix} m(\boldsymbol{r}_1, t_1) & m(\boldsymbol{r}_1, t_2) & \cdots & m(\boldsymbol{r}_1, t_{N_t}) \\ m(\boldsymbol{r}_2, t_1) & m(\boldsymbol{r}_2, t_2) & \cdots & m(\boldsymbol{r}_2, t_{N_t}) \\ \vdots & \vdots & \ddots & \vdots \\ m(\boldsymbol{r}_{N_s}, t_1) & m(\boldsymbol{r}_{N_s}, t_2) & \cdots & m(\boldsymbol{r}_{N_s}, t_{N_t}) \end{bmatrix} \tag{4.4}$$

where $\mathbf{M} \in {\mathbb{R}_+}^{N_s \times N_t}$, N_s is the total number of spatial components (i.e. number of

pixels) and N_t is the number of temporal components (i.e. number of echoes). The standard SVD of $\mathbf{M}$ is represented as:

$$\mathbf{M} = \mathbf{USV}^{\mathrm{T}} = \sum_{k=1}^{\min\{N_s, N_t\}} \lambda_k \boldsymbol{u}_k \boldsymbol{v}_k^T \tag{4.5}$$

where $\{\lambda_k\}_{k=1}^{\min\{N_s, N_t\}} \in \mathbb{R}$ are the singular values of $\mathbf{M}$, $\{\boldsymbol{u}_k\}_{k=1}^{\min\{N_s, N_t\}} \in \mathbb{R}^{\min\{N_s, N_t\}\times 1}$ are the left singular vectors representing the spatial weight, $\{\boldsymbol{v}_k\}_{k=1}^{\min\{N_s, N_t\}} \in \mathbb{R}^{\min\{N_s, N_t\}\times 1}$ are the right singular vectors representing the temporal basis. The rank-R approximation of $\mathbf{M}$ is obtained by:

$$\widehat{\mathbf{M}} = \widehat{\mathbf{U}}\widehat{\mathbf{S}}\widehat{\mathbf{V}}^{\mathrm{T}} = \sum_{k=1}^{R} \lambda_k \boldsymbol{u}_k \boldsymbol{v}_k^T,$$

$$s.t.\ \left\|\mathbf{M} - \widehat{\mathbf{M}}\right\|_F = \sqrt{\sum_{k=R+1}^{\min\{N_s, N_t\}} \lambda_k} \tag{4.6}$$

where $\widehat{\mathbf{U}} \in \mathbb{R}^{N_s\times R}$, $\widehat{\mathbf{S}} \in \mathbb{R}^{R\times R}$, $\widehat{\mathbf{V}} \in \mathbb{R}^{N_t\times R}$, F represents the Frobenius norm. For the example mGRE data used here, the rank was approximated to four where the power of the residual signal is below 2%.

Representative $\{\boldsymbol{u}_k\}_{k=1}^{R}$ and $\{\boldsymbol{v}_k\}_{k=1}^{R}$ are shown in Figure 4.1a. As a result of standard SVD, signal sources are separated into the $\{\boldsymbol{v}_k\}_{k=1}^{R}$, which is ordered by the redundancy of the source signal. Among the temporal bases in Figure 4.1a, the first basis, $\boldsymbol{v}_1$, represents a slow-decaying T_2^* relaxation ($T_2^* \approx 44$ms) with relatively homogeneous spatial weights, $\boldsymbol{u}_1$. The other bases, $\boldsymbol{v}_2$, $\boldsymbol{v}_3$, and $\boldsymbol{v}_4$, however, have negative values which

cannot represent a true tissue-oriented T_2^* relaxation signal. Particularly, $\boldsymbol{v}_2$ represents fast-decaying signal but biased to negative value (Figr1a). The reason for this is that real-valued exponential decays (e.g., multi component T_2^* relaxation signals) are highly correlated with each other and separation of these signal sources are badly-conditioned under the constraint of orthogonality. Nevertheless, the spatial weight maps represent different anatomic features for $\boldsymbol{u}_2$, $\boldsymbol{u}_3$, and $\boldsymbol{u}_4$.

Through SVD, I have described the potential of BSS in mGRE data. Although the temporal basis cannot reveal the actual feature of T_2^* relaxation, the signal sources can be distinguished by different characteristics.

(a) BSS in mGRE using SVD

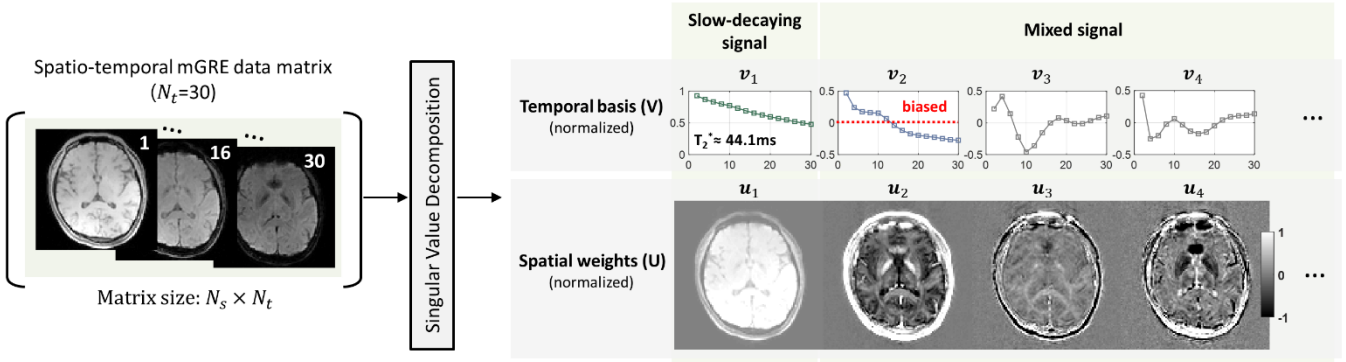

(b) BSS in hankelized mGRE using NMF

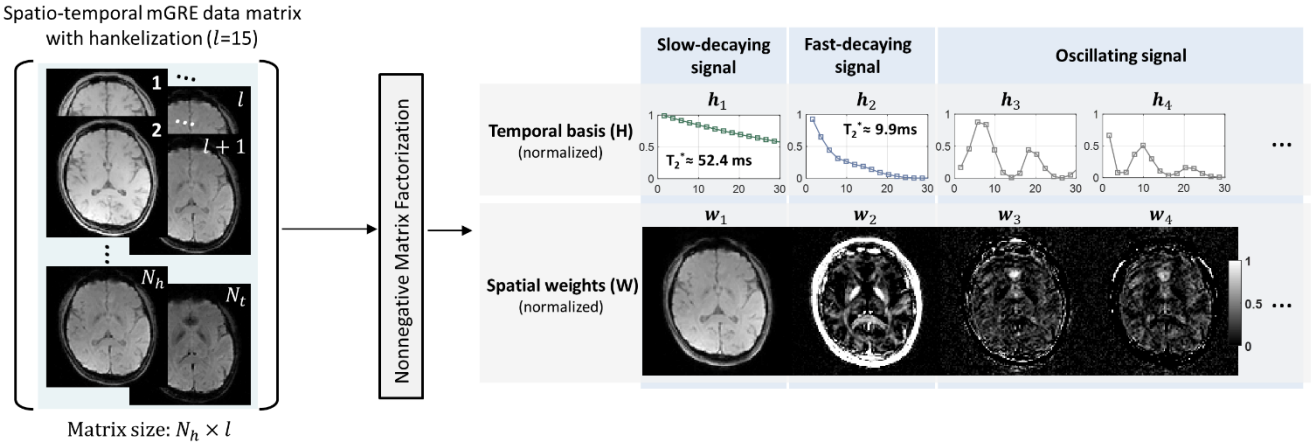

Figure 4.1. A conceptual illustration of BSS in spatio-temporal mGRE data matrix (subject 1). (a) Standard SVD applied to mGRE data matrix and (b) NMF applied to mGRE data matrix with hankelization (l =15). For each BSS scheme, four representative temporal bases ($\{\boldsymbol{v}_k\}_{k=1}^{4}$ and $\{\boldsymbol{h}_k\}_{k=1}^{4}$) and spatial weights ($\{\boldsymbol{u}_k\}_{k=1}^{4}$ and $\{\boldsymbol{w}_k\}_{k=1}^{4}$) are shown. Note that BSS using NMF provides temporal bases that corresponds more to the physical signal characteristics than using SVD.

4.2 Theory

4.2.1 Priorities of mGRE signal

In order to overcome the aforementioned problem when using standard SVD, additional constraints in the signal sources were incorporated which enforces the non-negativity of the temporal basis and exponential characteristics of T_2^* relaxation.

As a variant of SVD, non-negative matrix factorization (NMF) was implemented to take into consideration that the T_2^* relaxation of the myelin and axonal/extracellular water components is non-negative [80]. This constraint is similar to a common assumption used in conventional MWI processing (i.e. NNLS) [61, 77, 78]. The NMF of the spatio-temporal matrix $\mathbf{M}$ is now represented as:

$$\mathbf{M} \approx \widehat{\mathbf{W}}\widehat{\mathbf{H}}^{\mathrm{T}} = \sum_{k=1}^{R} \boldsymbol{w}_k \boldsymbol{h}_k^T \tag{4.7}$$

where $\widehat{\mathbf{W}} \in {\mathbb{R}_+}^{N_s \times R}$, $\widehat{\mathbf{H}} \in {\mathbb{R}_+}^{N_t \times R}$, $\{\boldsymbol{w}_k\}_{k=1}^{R} \in {\mathbb{R}_+}^{N_s \times 1}$ are the left singular vectors representing the spatial weight, $\{\boldsymbol{h}_k\}_{k=1}^{R} \in {\mathbb{R}_+}^{N_t \times 1}$ are the right singular vectors representing the temporal basis. In conventional NMF, $\widehat{\mathbf{W}}$ and $\widehat{\mathbf{H}}$ are obtained by:

$$\min \left\| \mathbf{M} - \widehat{\mathbf{W}}\widehat{\mathbf{H}}^{\mathrm{T}} \right\|_F^2 \qquad s.t.\ \widehat{\mathbf{W}}, \widehat{\mathbf{H}} \geq 0 \tag{4.8a}$$

$$\mathrm{H} \leftarrow \mathrm{H} \odot \frac{\mathrm{W}^{\mathrm{T}}\mathrm{M}}{\mathrm{W}^{\mathrm{T}}\mathrm{W}\mathrm{H}}, \quad \mathrm{W} \leftarrow \mathrm{W} \odot \frac{\mathrm{X}\mathrm{H}^{\mathrm{T}}}{\mathrm{W}\mathrm{H}\mathrm{H}^{\mathrm{T}}} \tag{4.8b}$$

using multiplicative update rule with element-wise multiplication operator $\odot$ [81]. As

the results of NMF depend on the initial value of $\widehat{\mathbf{W}}$ and $\widehat{\mathbf{H}}$, various initialization techniques have been suggested [82-84]. Here, based on the observation of standard SVD in mGRE data which has potential to represent tissue-oriented structure (Figure 4.1a), NMF with SVD based initialization method in [82] referred to as nonnegative double singular value decomposition (NNDSVD) was implemented. One of the features of NNDSVD is that the uniqueness of initial value guarantee the convergence to the same solution [82].

Prior to the NMF operation, as a temporal operator, hankelization was implemented in order to enforce the unit rank property of each temporal basis [85]. The hankelized matrix of $\mathbf{M}$ with hankelization length l is shown in Figure 4.1b and is represented as [86, 87]:

$$\mathcal{H}_l\big(\mathbf{M}(\boldsymbol{r},t)\big) = \begin{bmatrix} m(\boldsymbol{r}_1,t_1) & m(\boldsymbol{r}_1,t_2) & \cdots & m(\boldsymbol{r}_1,t_l) \\ m(\boldsymbol{r}_1,t_2) & m(\boldsymbol{r}_1,t_3) & \cdots & m(\boldsymbol{r}_1,t_{l+1}) \\ \vdots & \vdots & \ddots & \vdots \\ m(\boldsymbol{r}_{N_h},t_1) & m(\boldsymbol{r}_{N_h},t_2) & \cdots & m(\boldsymbol{r}_{N_h},t_{N_t}) \end{bmatrix} \tag{4.9}$$

where $\mathcal{H}_l(\mathbf{M}) \in {\mathbb{R}_+}^{N_h \times l}$ and $N_h = N_s(N_t - l + 1)$. When the echo spacing is equidistant (i.e., $t_i - t_{i-1} = \Delta TE$), the relaxation rate for the j^{th} component in Eq. 4.1 is proportional by an amount $e^{-(1/T_{2,j}^*)\Delta TE}$ for any echo time. This indicates that the hankelization of a mono-exponential signal has unit-rank. Based on this, the hankelization was implemented in order to encourage the unit-rank property of each exponential decay [85]. The hankelization length, *l*, was selected to half the total number of echoes as an optimal length for exponential signal [88].

After incorporating these two constraints (Figure 4.1b), the first and second temporal

basis, $\boldsymbol{h}_1$ and $\boldsymbol{h}_2$, become closer to pure exponential decays. The separated mono-exponential T_2^* values corresponds well to the slow (i.e., axonal/extracellular water signal) and fast (i.e., myelin water signal) components (T_2^* of $\boldsymbol{h}_1$ = 52.4ms, T_2^* of $\boldsymbol{h}_2$ = 9.9ms) [61]. Furthermore, the other temporal bases, $\boldsymbol{h}_3$ and $\boldsymbol{h}_4$, represent oscillating signals which are related to remnant residual components including artifacts.

4.2.2 Algorithm of the proposed rPCA-MWF

Based on the aforementioned ideas, a modified rPCA to separate three distinct sources from mGRE data is presented. The original rPCA separates the signal sources into a low-rank component, **L**, and a sparse component, **S**, by solving the minimization problem with convex objective function as [9, 74] :

$$\mathcal{J}(\mathbf{L},\mathbf{S}) \equiv \frac{1}{2}\|\mathbf{L}+\mathbf{S}-\mathbf{M}\|_2^2 + \mu\|\mathbf{L}\|_* + \rho\|\mathbf{S}\|_1 \tag{4.10}$$

where $\mathbf{M},\mathbf{L},\mathbf{S} \in \mathbb{R}^{N_s \times N_t}$, $\|\cdot\|_*$ denotes the nuclear norm, $\|\cdot\|_1$ denotes the ℓ_1-norm, μ and ρ denote regularization parameters for low rankness and sparsity, respectively. In this study, the signal source of mGRE data was separated to two unit-rank components (i.e., slow-decaying signal ($\mathbf{L_1}$) and fast-decaying signal ($\mathbf{L_2}$)) and sparse component (i.e., residual artifact signal (**S**)). The minimization problem $\min_{\mathbf{L}_1,\mathbf{L}_2,\mathbf{S}} \mathcal{J}(\mathbf{L}_1,\mathbf{L}_2,\mathbf{S})$ with the convex objective function is defined as:

$$\mathcal{J}(\mathbf{L}_1, \mathbf{L}_2, \mathbf{S}) \equiv \frac{1}{2}\|\mathbf{L}_1 + \mathbf{L}_2 + \mathbf{S} - \mathbf{M}\|_2^2$$

$$+\mu_1 \sum_r \left\|\mathcal{R}_r\left(\mathcal{H}_l(\mathbf{L}_1)\right)\right\|_* + \mu_2 \sum_r \left\|\mathcal{R}_r\left(\mathcal{H}_l(\mathbf{L}_2)\right)\right\|_* + \rho\|\Psi(\mathbf{S})\|_1 \quad (4.11)$$

where $\mathcal{H}_l$ denotes hankelization operator in the temporal domain, Ψ denotes temporal sparsifying operater (1D FFT in the echo domain), $\mathcal{R}_r$ denotes the extraction of local patches for locally low-rank (LLR) structure at the r^{th} patch [89-91], μ_1, μ_2 and ρ denote regularization parameters for LLR and sparsity respectively. The LLR constraint, which has higher redundancy than entire image, was implemented to encourage the low rankness of local patches for $\mathbf{L}_1$ and $\mathbf{L}_2$ [89-91]. Equation (4.11) is solved using the alternating direction method of multipliers (ADMM) [11, 92, 93]. Based on the variable splitting scheme in [93], Eq (11) is re-formulated as:

$$\min_{\substack{\mathbf{U}_{1,r},\mathbf{U}_{2,r},\mathbf{U}_3,\\ \mathbf{L}_1,\mathbf{L}_2,\mathbf{S}}} \frac{1}{2}\|\mathbf{L}_1 + \mathbf{L}_2 + \mathbf{S} - \mathbf{M}\|_2^2 + \mu_1 \sum_r \left\|\mathbf{U}_{1,r}\right\|_* + \mu_2 \sum_r \left\|\mathbf{U}_{2,r}\right\|_* + \rho\|\mathbf{U}_3\|_1$$

$$s.t. \begin{cases} \mathbf{U}_{1,r} = \mathcal{R}_r\left(\mathcal{H}_l(\mathbf{L}_1)\right) \\ \mathbf{U}_{2,r} = \mathcal{R}_r\left(\mathcal{H}_l(\mathbf{L}_2)\right) \\ \mathbf{U}_3 = \Psi(\mathbf{S}) \end{cases} \quad (4.12)$$

and the associated augmented Lagrangian function is:

$$\mathcal{L}_A = \frac{1}{2}\|\mathbf{L}_1 + \mathbf{L}_2 + \mathbf{S} - \mathbf{M}\|_2^2 + \mu_1 \sum_r \left\|\mathbf{U}_{1,r}\right\|_* + \mu_2 \sum_r \left\|\mathbf{U}_{2,r}\right\|_* + \rho\|\mathbf{U}_3\|_1$$

$$+ \sum_r \langle \mathbf{Z}_{1,r}, \mathcal{R}_r\left(\mathcal{H}_l(\mathbf{L}_1)\right) - \mathbf{U}_{1,r}\rangle + \sum_r \left\|\frac{\delta_1}{2}\mathcal{R}_r\left(\mathcal{H}_l(\mathbf{L}_1)\right) - \mathbf{U}_{1,r}\right\|_2^2$$

$$+\sum_r \langle \mathbf{Z}_{2,\mathrm{r}}, \mathcal{R}_r\left(\mathcal{H}_\mathrm{l}(\mathbf{L}_2)\right) - \mathbf{U}_{2,\mathrm{r}} \rangle + \sum_r \left\| \frac{\delta_2}{2} \mathcal{R}_r\left(\mathcal{H}_\mathrm{l}(\mathbf{L}_2)\right) - \mathbf{U}_{2,\mathrm{r}} \right\|_2^2$$

$$+\langle \mathbf{Z}_3, \Psi(\mathbf{S}) - \mathbf{U}_3 \rangle + \frac{\delta_3}{2} \|\Psi(\mathbf{S}) - \mathbf{U}_3\|_2^2 \tag{4.13}$$

where $\mathbf{Z}_{1,\mathrm{r}}$, $\mathbf{Z}_{2,\mathrm{r}}$ and $\mathbf{Z}_3$ are Lagrangian multipliers. Ignoring constants irrelevant to optimization, Eq (13) can be written as:

$$\mathcal{L}_A = \frac{1}{2}\|\mathbf{L}_1 + \mathbf{L}_2 + \mathbf{S} - \mathbf{M}\|_2^2 + \mu_1 \sum_r \left\|\mathbf{U}_{1,\mathrm{r}}\right\|_* + \mu_2 \sum_r \left\|\mathbf{U}_{2,\mathrm{r}}\right\|_* + \rho\|\mathbf{U}_3\|_1$$

$$+\sum_r \frac{\delta_1}{2} \left\|\mathcal{R}_r\left(\mathcal{H}_\mathrm{l}(\mathbf{L}_1)\right) + {\delta_1}^{-1}\mathbf{Z}_{1,\mathrm{r}} - \mathbf{U}_{1,\mathrm{r}}\right\|_2^2$$

$$+\sum_r \frac{\delta_2}{2} \left\|\mathcal{R}_r\left(\mathcal{H}_\mathrm{l}(\mathbf{L}_2)\right) + {\delta_2}^{-1}\mathbf{Z}_{2,\mathrm{r}} - \mathbf{U}_{2,\mathrm{r}}\right\|_2^2$$

$$+\frac{\delta_3}{2} \left\|\Psi(\mathbf{S}) - {\delta_3}^{-1}\mathbf{Z}_3 - \mathbf{U}_3\right\|_2^2 \tag{4.14}$$

where δ_1, δ_2, δ_3 denotes regularization parameters. The ADMM minimizes $\mathcal{L}_A$ over $\mathbf{U}_1, \mathbf{U}_2, \mathbf{U}_3, \mathbf{L}_1, \mathbf{L}_2$ and $\mathbf{S}$ separately by solving sub-problems with closed-form solutions:

$$\mathbf{U}_{1,\mathrm{r}}{}^{(k+1)} = \underset{\mathbf{U}_{1,\mathrm{r}}}{\operatorname{argmin}} \frac{\mu_1}{\delta_1}\left\|\mathbf{U}_{1,\mathrm{r}}\right\|_* + \frac{1}{2}\left\|\mathcal{R}_r\left(\mathcal{H}_\mathrm{l}\left(\mathbf{L}_1{}^{(k)}\right)\right) + {\delta_1}^{-1}\mathbf{Z}_{1,\mathrm{r}}{}^{(k)} - \mathbf{U}_{1,\mathrm{r}}\right\|_2^2$$

$$= SVT_{\mu_1/\delta_1}\left(\mathcal{R}_r\left(\mathcal{H}_\mathrm{l}\left(\mathbf{L}_1{}^{(k)}\right)\right) + {\delta_1}^{-1}\mathbf{Z}_{1,\mathrm{r}}{}^{(k)}\right) \tag{4.15a}$$

$$\mathbf{U}_{2,\mathrm{r}}{}^{(k+1)} = \underset{\mathbf{U}_{2,\mathrm{r}}}{\operatorname{argmin}} \frac{\mu_2}{\delta_2}\left\|\mathbf{U}_{2,\mathrm{r}}\right\|_* + \frac{1}{2}\left\|\mathcal{R}_r\left(\mathcal{H}_\mathrm{l}\left(\mathbf{L}_2{}^{(k)}\right)\right) + {\delta_2}^{-1}\mathbf{Z}_{2,\mathrm{r}}{}^{(k)} - \mathbf{U}_{2,\mathrm{r}}\right\|_2^2$$

$$= SVT_{\mu_2/\delta_2}\left(\mathcal{R}_r\left(\mathcal{H}_\mathrm{l}\left(\mathbf{L}_2{}^{(k)}\right)\right) + {\delta_2}^{-1}\mathbf{Z}_{2,\mathrm{r}}{}^{(k)}\right) \tag{4.15b}$$

$$\mathbf{U}_3{}^{(k+1)} = \underset{\mathbf{U}_3}{\operatorname{argmin}} \frac{\rho}{\delta_3} \|\mathbf{U}_3\|_1 + \frac{1}{2} \left\| \mathbf{S}^{(k)} + \delta_3{}^{-1} \mathbf{Z}_3{}^{(k)} - \mathbf{U}_3 \right\|_2^2$$

$$= ST_{\rho/\delta_3}(\mathbf{S}^{(k)} + \delta_3{}^{-1} \mathbf{Z}_3{}^{(k)}) \tag{4.15c}$$

where SVT_{μ_1/δ_1} and SVT_{μ_2/δ_2} denotes (hard) singular value thresholding operators using NMF for each local patches r, ST_{ρ/δ_3} denotes soft thresholding operators [9, 94].

$$\mathbf{L}_1{}^{(k+1)} = \underset{\mathbf{L}_1}{\operatorname{argmin}} \frac{1}{2} \left\| \mathbf{L}_1 + \mathbf{L}_2{}^{(k)} + \mathbf{S}^{(k)} - \mathbf{M} \right\|_2^2$$

$$+ \sum_r \frac{\delta_1}{2} \left\| \mathcal{R}_r\left(\mathcal{H}_l(\mathbf{L}_1)\right) + \delta_1{}^{-1} \mathbf{Z}_{1,\mathrm{r}}{}^{(k)} - \mathbf{U}_{1,\mathrm{r}}{}^{(k)} \right\|_2^2$$

$$= \frac{1}{1+\delta_1} (\mathbf{M} - \mathbf{L}_2{}^{(k)} - \mathbf{S}^{(k)} + \delta_1 \mathbf{U}_1 - \mathbf{Z}_1) \tag{4.16a}$$

$$\mathbf{L}_2{}^{(k+1)} = \underset{\mathbf{L}_2}{\operatorname{argmin}} \frac{1}{2} \left\| \mathbf{L}_1{}^{(k+1)} + \mathbf{L}_2 + \mathbf{S}^{(k)} - \mathbf{M} \right\|_2^2$$

$$+ \sum_r \frac{\delta_2}{2} \left\| \mathcal{R}_r\left(\mathcal{H}_l(\mathbf{L}_2)\right) + \delta_2{}^{-1} \mathbf{Z}_{2,\mathrm{r}}{}^{(k)} - \mathbf{U}_{2,\mathrm{r}}{}^{(k)} \right\|_2^2$$

$$= \frac{1}{1+\delta_2} (\mathbf{M} - \mathbf{L}_1{}^{(k+1)} - \mathbf{S}^{(k)} + \delta_2 \mathbf{U}_2 - \mathbf{Z}_2) \tag{4.16b}$$

$$\mathbf{S}^{(k+1)} = \underset{\mathbf{S}}{\operatorname{argmin}} \frac{1}{2} \left\| \mathbf{L}_1{}^{(k+1)} + \mathbf{L}_2{}^{(k+1)} + \mathbf{S} - \mathbf{M} \right\|_2^2$$

$$+ \frac{\delta_3}{2} \left\| \Psi(\mathbf{S}) - \delta_3{}^{-1} \mathbf{Z}_3{}^{(k)} - \mathbf{U}_3{}^{(k)} \right\|_2^2$$

$$= \frac{1}{1+\delta_3} (\mathbf{M} - \mathbf{L}_1{}^{(k+1)} - \mathbf{L}_2{}^{(k+1)} + \delta_3 \mathbf{U}_3 - \mathbf{Z}_3) \tag{4.16c}$$

where dehankelization was performed while solving Eq (16a) and Eq (16b). Corresponding Lagrangian multipliers are updated as:

$$\mathbf{Z}_1{}^{(k+1)} = \mathbf{Z}_1{}^{(k)} + \mathbf{L}_1{}^{(k+1)} - \mathbf{U}_1{}^{(k+1)} \tag{4.17a}$$

$$\mathbf{Z}_2{}^{(k+1)} = \mathbf{Z}_2{}^{(k)} + \mathbf{L}_2{}^{(k+1)} - \mathbf{U}_2{}^{(k+1)} \tag{4.17b}$$

$$\mathbf{Z}_3{}^{(k+1)} = \mathbf{Z}_3{}^{(k)} + \Psi\left(\mathbf{S}^{(k+1)}\right) - \mathbf{U}_3{}^{(k+1)} \tag{4.17c}$$

The regularization parameters for the proposed rPCA-MWF were empirically set as follows: $\mu_1 = 1,\ \mu_2 = 1,\ \rho = 0.5,\ \delta_1 = 0.01,\ \delta_2 = 0.01,\ \delta_3 = 0.0005$. The local patch size and convergence tolerance were empirically set as follows: patch size = 8x8x8, and $\epsilon = 10^{-6}$. Here, the convergence rate was estimated to relative residual ($\left\|\mathbf{X}^{k+1} - \mathbf{X}^{k}\right\|_2 / \left\|\mathbf{X}^{k}\right\|_2 \times 100$). A summary of the iteration process is described in Table 4.1. (See Figure 4.2 for simulations on the determination of hyperparameters and the convergence rate of the algorithm).

Task:
Find $\mathbf{L}_1$, $\mathbf{L}_2$ and $\mathbf{S}$ minimizing Eq. (11)
Initialization:
Iteration index: $k = 1$,
Initial solutions: $\mathbf{U_{1,r}}^{(0)}$, $\mathbf{U_{2,r}}^{(0)}$, $\mathbf{U_3}^{(0)} = 0$,
$\mathbf{L}_1 = SVT_{\mu_1/\delta_1}(\mathbf{M})$,
$\mathbf{L}_2 = SVT_{\mu_2/\delta_2}(\mathbf{M}) - \mathbf{L}_1$,
$\mathbf{S} = \mathbf{M} - \mathbf{L}_1 - \mathbf{L}_2$,
$\mathbf{Z_1}^{(0)}$, $\mathbf{Z_2}^{(0)}$, $\mathbf{Z_3}^{(0)} = 0$,
while "not converged" **and** "k < 100" **do**
Step 1: Update $\mathbf{U_1}, \mathbf{U_2}, \mathbf{U_3}$ by solving Eq. (15)
Step 2: Update $\mathbf{L}_1$, $\mathbf{L}_2$, $\mathbf{S}$ by solving Eq. (16)
Step 3: Update $\mathbf{Z}_1$, $\mathbf{Z}_2$, $\mathbf{Z}_3$ by solving Eq. (17)
Step 4: Increase the iteration number k
end
Output: $\widehat{\mathbf{L}_1} = \mathbf{L}_1^k$, $\widehat{\mathbf{L}_2} = \mathbf{L}_2^k$, $\hat{\mathbf{S}} = \mathbf{S}^k$

Table 4.1. rPCA-MWF algorithm

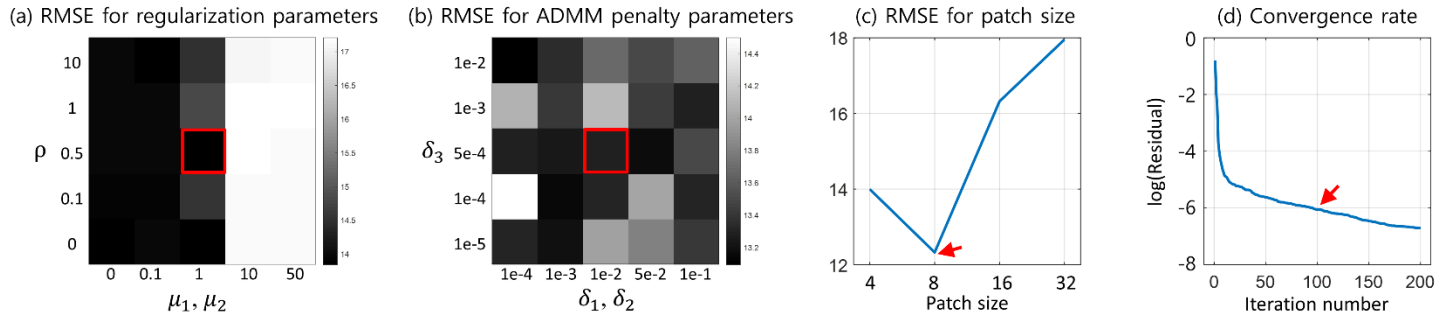

Figure 4.2. Simulation results for determination of hyperparameters and convergence plot of the iterative algorithm. The RMSE is shown for difference hyperparameter settings. (a) Regularization parameters (μ_1, μ_2 and ρ), (b) ADMM penalty parameters (δ_1, δ_2 and δ_3) and (c) patch size (r). (d) Convergence rate with respect to iteration number ($Residual = \|\boldsymbol{X}^{k+1} - \boldsymbol{X}^{k}\|_2 / \|\boldsymbol{X}^{k}\|_2 \times 100$ where $\mathbf{X}^{k} = \boldsymbol{L_1}^{k} + \boldsymbol{L_2}^{k} + \boldsymbol{S}^{k}$). The hyperparameters used in this study are marked by red boxes and arrows. The regularization parameters for rankness (i.e., μ_1 and μ_2) and the ADMM penalty parameters (i.e., δ_1 and δ_2) were set identically as they possess the same attributes.

Afterwards, the MWF was mapped as the ratio of 2nd unit rank component to total unit-rank component at TE_1 for each voxel;

$$MWF(\boldsymbol{r}) = \frac{\mathbf{L}_2(\boldsymbol{r},TE_1)}{\mathbf{L}_1(\boldsymbol{r},TE_1)+\mathbf{L}_2(\boldsymbol{r},TE_1)} \times 100\ (\%) \tag{4.18}$$

The residual signal was mapped to the sparse component, which can also be sparsified in the frequency domain.

I provide the source code and related data (in MATLAB) to reproduce most of the results described in this paper. The source code and related data can be downloaded from:

https://github.com/Yonsei-MILab.

4.3 Methods

4.3.1 Comparison of Model-based MWF and rPCA-MWF

Among the GRE-MWI models, two types of model-based method were adopted; three-component magnitude and complex model which I refer here as "magnitude model-based" (Eq. 4.2) and "complex model-based" (Eq. 4.3) respectively. In simulations, magnitude model-based MWF was compared to rPCA-MWF due to difficulty of modeling three component complex signals. In in-vivo experiments, magnitude and complex model-based MWF were compared to rPCA-MWF. In this study, a total 30 echoes were used with the last echo time of 31.81 ms. Note that multi-component magnitude model-based MWF using

rNNLS does not provide adequate results due to the limited number of echoes.

4.3.2 Simulations

Numerical simulations were performed on an analytic phantom to compare the performance of MWF estimation between model-based MWF and rPCA-MWF for various situations. An analytic phantom composed of 24 region-of-interests (ROI) was designed. Each ROI had a size of 8x8 voxels, containing two water pools (i.e., slowly-decaying component ($T_{2,slow}^{*}$) and fast-decaying component ($T_{2,fast}^{*}$)) with various T_2^* and MWF (Figure 4.3a). The index of each ROI was set to 1-6, 7-12, 13-18 and 19-24 for each column. For ROI 1-12, $T_{2,slow}^{*}$ and $T_{2,fast}^{*}$ were set to 60ms and 10ms respectively and MWF varied from 2% to 24 % with step size 2%. For ROI 13-18, $T_{2,slow}^{*}$ varied from 40ms to 90ms with step size 10ms and $T_{2,S}^{*}$ was set to 10ms. For ROI 19-24, $T_{2,slow}^{*}$ was set to 60ms and $T_{2,fast}^{*}$ varied from 5ms to 15ms with step size 2ms. The MWF of ROI 13-24 were set to 10%. Each parameter was set based on the literature values of the myelin and axonal/extracellular water component of healthy white matter at 3T [77].

In order to reflect a more realistic biological tissue characteristics representing a continuous distribution for each water pool, the aforementioned T_2^* components of each ROI were modeled to have a Gaussian distribution centered at each T_2^*, with a standard deviation of 10% of each T_2^* [95]. The first TE and echo spacing was set to 2ms and 1ms respectively and 30 echoes were assumed to be sampled [96].

White Gaussian noise was added so that the SNR of the magnitude image at the first TE varied from 240 to 60 with a step size of 20. A series of Monte-Carlo simulations were performed with 100 repetitions for each case. The error of the estimated MWF map was evaluated with RMSE and the standard deviation of each ROI was calculated.

The effects of the number of echoes on the rPCA-MWF was studied using simulated data. The true and estimated MWF was calculated assuming different number of echoes collected (from 12 to 32 with step size of 4). Subsequently, a linear regression of the calculated result was performed. By doing this, the slope of the linear regression provided information about the overall underestimation and the intercept of the regression provided the overall bias information.

4.3.3 In-vivo experiment

All MR imaging experiments were performed on 3 Tesla clinical scanners (Tim Trio/Skyra, Siemens, Erlangen, Germany or Signa, General Electric Company, Milwaukee, WI). All examination was performed with approval from the institution's ethical review board and all subjects provided signed, informed consent prior to participation. A 12-channel phased-array head coil and a 32-channel head coil were used for data reception in Siemens scanner and GE scanner respectively.

The 3D mGRE imaging parameters were FOV = 256×256×80mm^3, spatial resolution = 2×2×2 mm^3, TR = 46 ms, TE_1 = 1.65 ms, ΔTE = 1.04 ms, # of echoes = 30, flip-angle =

20°, bandwidth = 1560 Hz/pixel and total scan time = 3min 55sec. For anatomical reference, T_1-weighted sagittal 3D MPRAGE (1.0 mm isotropic) was used for all subjects.

Data were collected from 10 subjects. Subjects 1~7 were healthy volunteers (age range: 25-35) with no documented disease in the brain. Subject 8, 9 and 10 were patients with pathologically confirmed disease by a radiologist; dementia (female, age 70), non-amnestic mild cognitive impairment (MCI) disease (female, age 81) and x-linked adrenoleukodystrophy (X-ALD) disease, respectively. Note that all the experiments were performed on Siemens scanner except for subject 10. The experiment for subject 10 with X-ALD disease was performed on GE scanner in order to acquire another quantitative myelin water imaging method equipped on scanner; quantitative inhomogeneous magnetization transfer imaging [97].

For subject 10 with X-ALD, parameters of mGRE imaging were modified due to different scanner conditions: FOV=256×256×100mm3, spatial resolution=1.6×1.6×2.0 mm3, TR = 60 ms, TE_1 = 1.4 ms, ΔTE = 2.1 ms, # of echoes = 16, flip-angle = 25° and scan time = 8min. For anatomical reference, T_1-weighted sagittal image was acquired using 3D FSPGR. Furthermore, a inhomogeneous magnetization transfer (ihMT) imaging protocol [97] was added with the following parameters: 3D SPGR sequence, spatial resolution=3×3×3 mm3, TR = 10.2 ms, TE = 2 ms, flip-angle = 8° and scan time = 5min 34sec. After data acquisition, quantitative ihMT (qihMT) map was estimated by taking the difference of the longitudinal relaxation rates between two MT states, dual frequency and single frequency, by using a prototype image processing software provided by GE [97].

The reproducibility was calculated using Pearson's correlation coefficient for white matter region. First, to evaluate the reproducibility of the MWF maps, subjects 1~7 were scanned twice and a correlation between the two scans was calculated. Student's t-test was performed to evaluate the statistical significance of model-free MWF map against model-based MWF maps. The significance level was set to 0.05. Second, to evaluate the noise sensitivity of the technique, additional white gaussian noise was added to mGRE data from subject 7. The MWF map from original mGRE images was used as a reference. The SNR of the reference mGRE image at the first echo was 160 and the noise corrupted images was from 60 to 140 with step size 20. The correlation between reference and noise additive cases was calculated.

4.4 Results

4.4.1 Simulations

The simulation result of the MWF mapping is shown in Figure 4.3. The noise of MWF map was reduced in rPCA-MWF compared to model-based MWF (Figure 4.3b and 4.3f). The standard deviation (STD) of the estimated MWF values from each ROI was reduced by more than 40 % in rPCA-MWF compared to model-based MWF (Figure 4.3c-4.3e and 4.3g-4.3i). For the ROIs with varying MWF (i.e., #1~12), the correlation coefficient of the estimated MWF for true MWF was 20% higher in rPCA-MWF than model-based MWF.

However, the linear regression of the estimated MWF showed underestimation of 15% for rPCA-MWF and model-based MWF (Figure 4.3c and 4.3g). Meanwhile, for the ROIs with varying $T_{2,slow}^{*}$ and $T_{2,fast}^{*}$ (i.e., ROI #13~24), the accuracy of the estimated MWF was more sensitive to variations in $T_{2,fast}^{*}$ than to $T_{2,slow}^{*}$ (Figure 4.3d-4.3e and 4.3h-4.3i).

The noise sensitivity of estimated MWF values from six representative ROIs is shown in Figure 4.4. The six representative ROIs were selected from regions where true MWF, $T_{2,slow}^{*}$ and $T_{2,fast}^{*}$ have minimum and maximum values (Figure 4.3a). The RMSE between true MWF map and estimated MWF map was reduced by more than 40% in rPCA-MWF compared to model-based MWF (Figure 4.4a). The STD of rPCA-MWF was invariant against true MWF, $T_{2,slow}^{*}$ and $T_{2,fast}^{*}$. However, the STD of model-based MWF increased as true MWF increased (Figure 4.4b). This shows the sensitivity of model-based method against true MWF. For all range of SNR, rPCA-MWF showed reduced RMSE and STD compared to model-based MWF, which supports robustness against noise of proposed method.

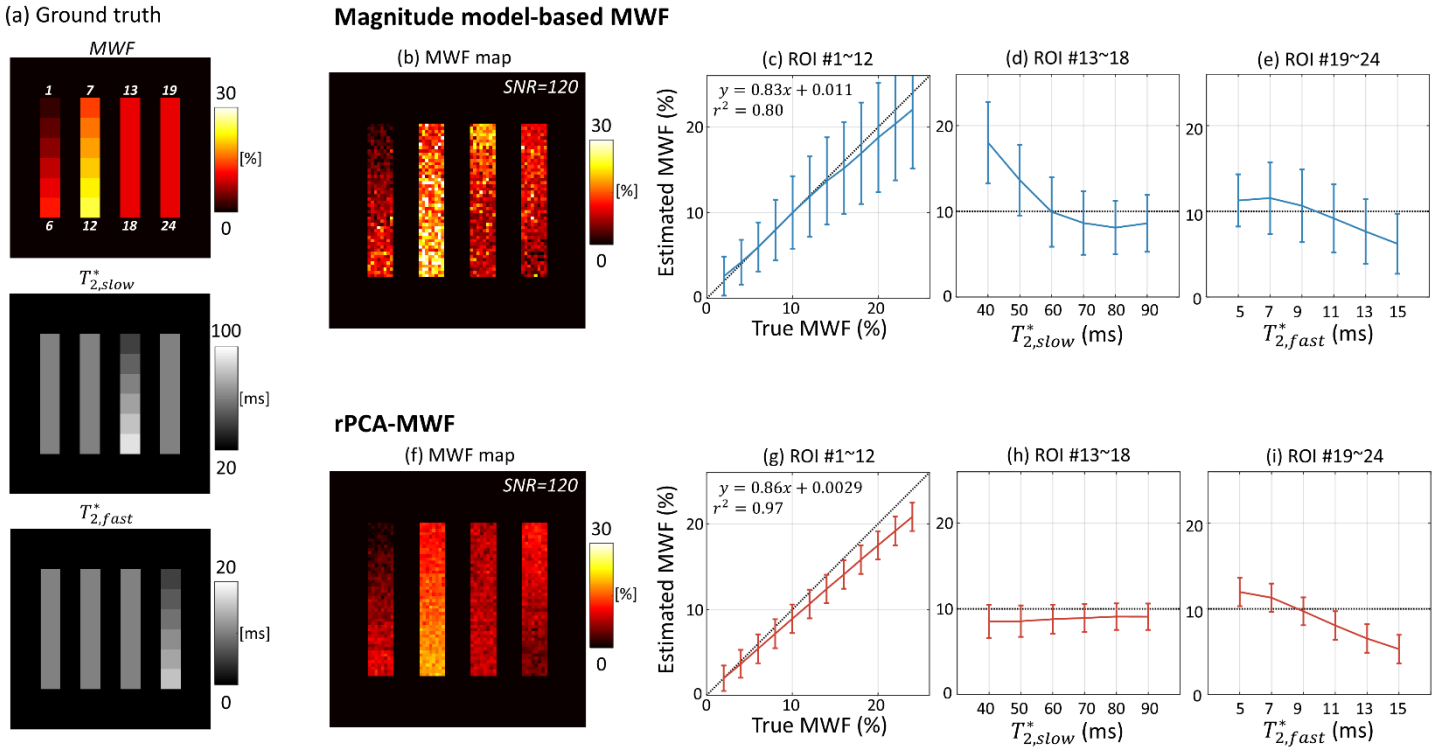

Figure 4.3. Numerical simulation of the MWF mapping for various $T_{2,\text{slow}}^*$, $T_{2,\text{fast}}^*$, and MWF. (a) Ground truth of the MWF, $T_{2,\text{slow}}^*$, $T_{2,\text{fast}}^*$. The MWF map and ROI analysis using (b-e) magnitude model-based MWF and (f-i) rPCA-MWF. Each column of ground truth indicates the ROI index 1~6, 7~12, 13~18 and 19~24 respectively.

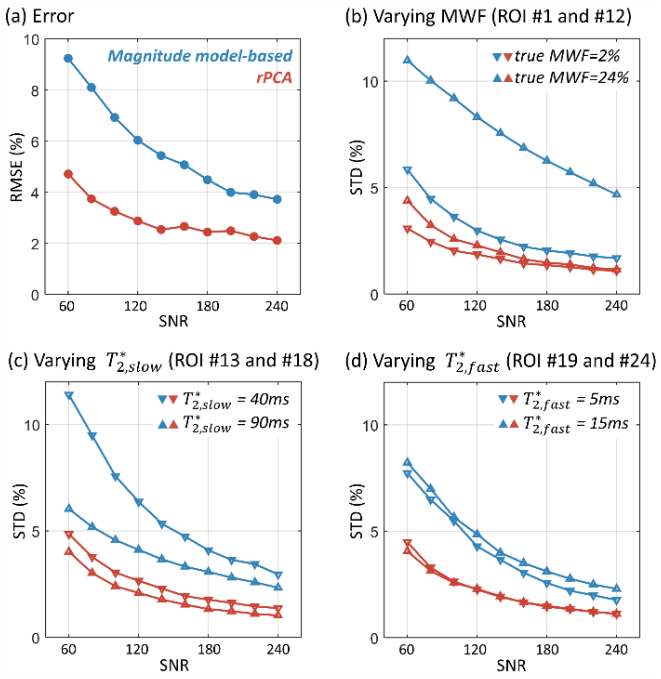

Figure 4.4. Noise sensitivity of the MWF map in simulation. (a) RMSE according to SNR. The STD of each ROI for (b) varying MWF (c) varying $T_{2,\text{slow}}{}^*$ and (c) varying $T_{2,\text{fast}}{}^*$. Note that only ROI #1,12,13,18,19 and 24 are represented here.

The effect of the number of echoes on the rPCA-MWF is shown in Figure 4.5. For both model-based MWF and rPCA-MWF, the overall underestimation gradually decreased as the number of echoes increased (Figure 4.5a). Meanwhile, the overall bias decreased as the number of echoes increased for model-based MWF while it was consistent for rPCA-MWF (Figure 4.5b). The number of echoes collected was determined to be 30 (i.e., the last echo of 32 ms) since the underestimation tended to slow down at this value while maintaining scan time. Additionally, the accuracy of estimated MWF values from four representative

ROIs is shown in Figure 4.6. The four representative ROIs were selected from regions where true $T_{2,\text{slow}}^{*}$ and $T_{2,\text{fast}}^{*}$ have minimum and maximum values. The accuracy of rPCA-MWF outperformed for varying $T_{2,\text{slow}}^{*}$.

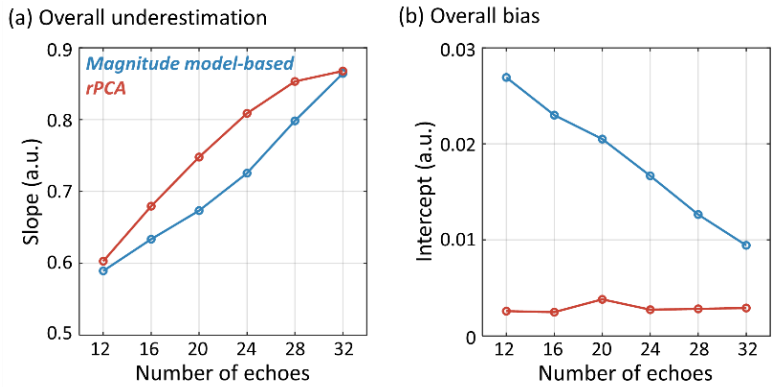

Figure 4.5. Effect of number of echoes on the MWF using simulated data. (a) The slope and (b) the intercept following linear regression of Figure 4.3c and 4.3g for varying number of echoes. Note that the slope represents overall underestimation and the intercept represents overall bias.

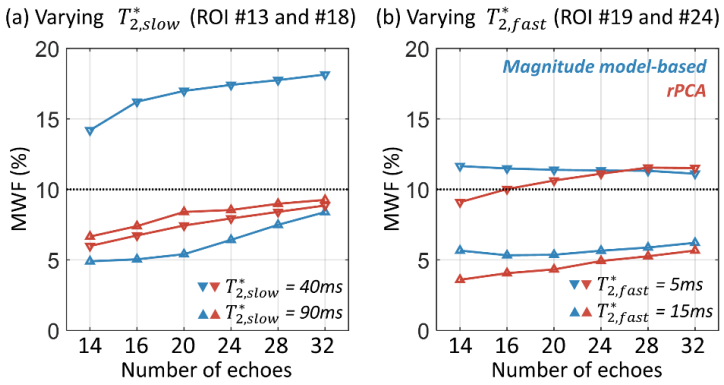

Figure 4.6. Effect of number of echoes in simulation. Estimated MWF for varying (a) $T_{2,\text{slow}}^{*}$ (ROI #13 and #18) and (b) $T_{2,\text{fast}}^{*}$ (ROI #19 and #24). Note that true MWF is 10%.

4.4.2 In-vivo experiments

Component-wise analysis for the decomposed source signal is shown in Figure 4.7. The decomposed mGRE data matrix using proposed rPCA-MWF shows three components; $\mathbf{L}_1$, $\mathbf{L}_2$ and $\mathbf{S}$. The $\mathbf{L}_1$ component represents slow-varying signals, while the $\mathbf{L}_2$ component represents signals appearing only at early echoes. The R_2^* maps of $\mathbf{M}$, $\mathbf{L}_1$ and $\mathbf{L}_2$ were reconstructed by mono-exponential fitting and the histogram of T2* measurements were plotted after removing the skull region by using FSL BET [98] (Figure 4.7b and 4.7c). The mean T_2^* values were measured at 20.6ms, 52.6ms and 9.7ms while the mean amplitude was 0.91, 0.84 and 0.08, respectively. The T_2^* measurements, especially short T_2^* value, corresponded well to the literature values of GRE-MWI reported to being 6~15 ms [62, 66, 78]. The $\mathbf{S}$ component represented residual signals including noise, and B_0–oriented artifact (frontal lobe, yellow arrow in Figure 4.7a). Other tissue signals such as subcutaneous fat is not of interest in this study.

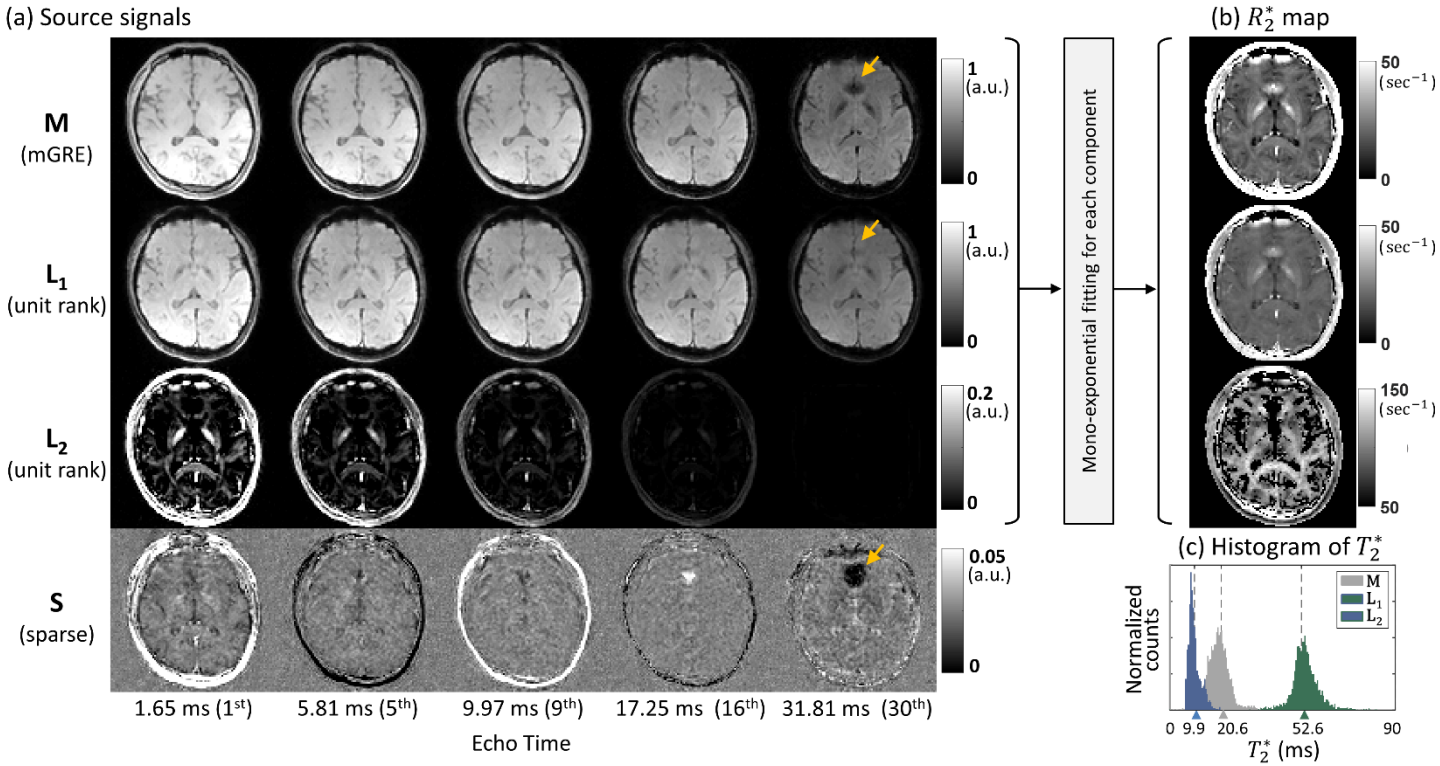
(a) Source signals
M
(mGRE)
L1
(unit rank)
L2
(unit rank)
S
(sparse)
1
(a.u.)
0
1
(a.u.)
0
0.2
(a.u.)
0
0.05
(a.u.)
0
1.65 ms (1st)
5.81 ms (5th)
9.97 ms (9th)
17.25 ms (16th)
31.81 ms (30th)
Echo Time
Mono-exponential fitting for each component
(b) R_2^* map
50
(sec^{-1})
0
50
(sec^{-1})
0
150
(sec^{-1})
50
(c) Histogram of T_2^*
Normalized counts
M
L1
L2
0
9.9
20.6
52.6
90
T_2^* (ms)

Figure 4.7. Component-wise analysis of rPCA-MWF (subject 1). (a) Spatial distribution and temporal evolution of original mGRE and each decomposed component for five representative echo times. Note that the abnormal signal decay at frontal lobe of $\mathbf{M}$ is decomposed to $\mathbf{S}$ component (yellow arrow). (b) R_2^* map estimated by mono-exponential fitting of $\mathbf{M}$, $\mathbf{L}_1$ and $\mathbf{L}_2$ signals. (c) Histogram of T_2^* from each R_2^* map. Note that the T_2^* of $\mathbf{L}_1$ and $\mathbf{L}_2$ are not biased to a single T_2^* but represent various T_2^*.

Representative MWF maps using magnitude model-based, complex model-based and rPCA technique are shown in Figure 4.8. A clearer visualization of the white matter area is noted for rPCA-MWF and corresponds well to the details of the MPRAGE images. Note that the magnitude model-based MWF and rPCA-MWF shows overestimation in the globus pallidus region compared to complex model-based MWF (first slice in Figure 4.8).

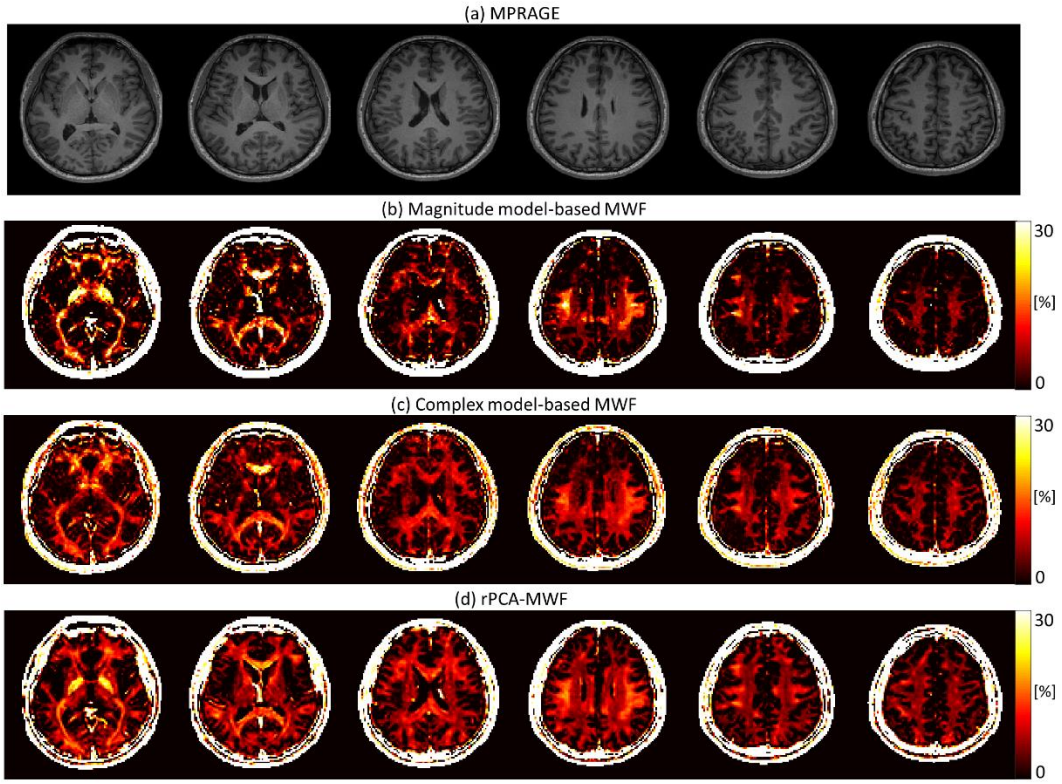

Figure 4.8. Six representative slices from healthy volunteer (subject 1). (a) MPRAGE, (b) magnitude three pool model-based MWF, (c) complex three pool model-based MWF and (d) rPCA-MWF.

Reproducibility results for the 7 subjects is given in Table 4.2. Correlation coefficients between two repeated scans are largest in the rPCA-MWF map with 0.925, which corresponds to an improvement of more than 10% compared to model-based MWF map ($p<0.05$). Also, the STD was smallest for the rPCA-MWF. In Figure 4.9, reproducibility analysis with respect to noise is shown. As more noise is present, the model-based MWF maps show reduced reproducibility with correlation coefficient under 0.8. The rPCA-MWF shows robustness with correlation coefficient over 0.9 even at SNR of 60. The discrete variation of rPCA-MWF resulted from the mis-estimation of $\mathbf{L}_2$ after SNR of 80.

	Magnitude model-based	Complex model-based	**rPCA**
r^2 (a.u.)	0.802 *	0.812 *	**0.925**
std (a.u.)	0.087	0.072	**0.052**

r^2: Pearson's correlation coefficient, * $p < 0.05$

Table 4.2. Reproducibility analysis of the MWF map for 7 healthy volunteers

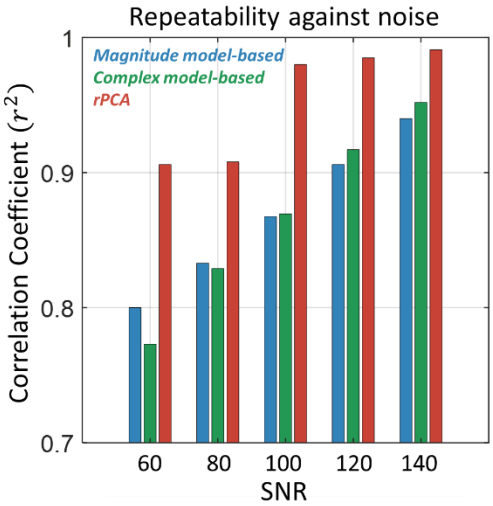

Figure 4.9. The reproducibility of the MWF map as noise corruption. $\mathbf{r^2}$ is Pearson's correlation coefficient between reference MWF map and noise additive MWF map.

Cases when artifacts were present are shown in Figure 4.10. Subject 9, 8 and 6 showed B_0 inhomogeneity, motion artifact and zipper artifact corrupted cases respectively. In Figure 4. 10a, temporal signal evolution of mGRE deviated from the exponential decay at the frontal lobe, and the complex model-based MWF image presented abnormal high values. The rPCA-MWF removed this to the $\mathbf{S}$ component. In Figure 4.10b, the aliasing patterns in mGRE image are separated to the S component and rPCA-MWF shows a more uniform distribution than model-based MWF. In Figure 4.10c, a zipper artifact in mGRE image is shown leading to abnormal overestimation of MWF in model-based MWF. The rPCA-MWF removed this to the S component. For all cases, the rPCA-MWF shows a clearer image of the MWF. In Figure 4.11, images from other slices and comparison with magnitude model-based MWF for each of these cases are provided.

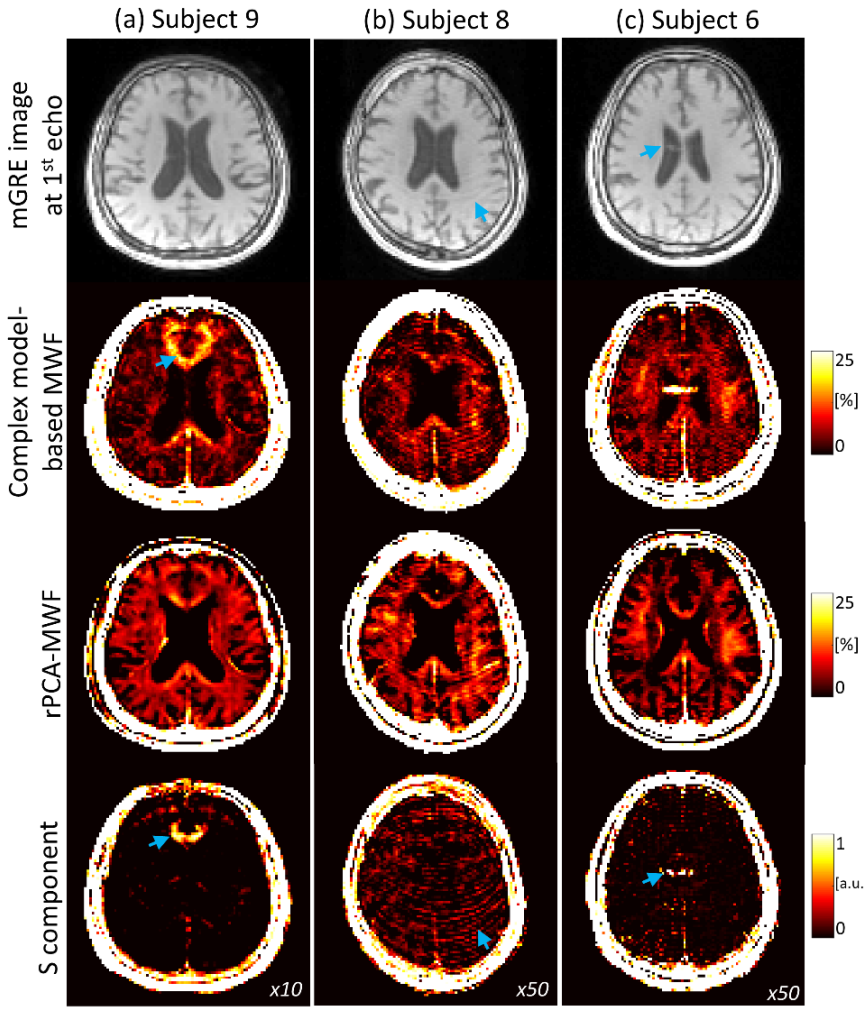

Figure 4.10. Single representative slice when imaging artifacts are present. (a) B_0 inhomogeneity (subject 9), (b) motion (subject 8) and (c) zipper (subject 6) artifacts. The rPCA-MWF shows reduced artefactual images. Note that the imaging artifacts depicted in mGRE images and complex model-based MWF are separated to the S component.

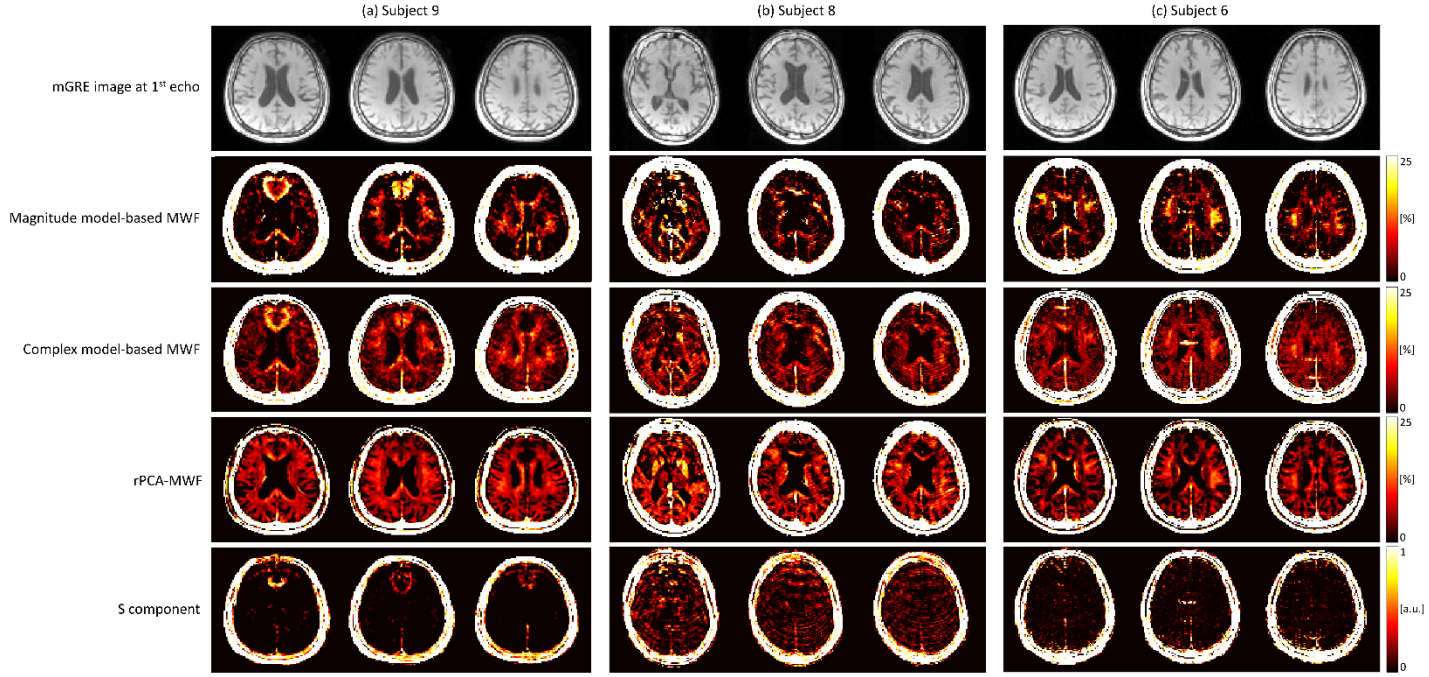

Figure 4.11. Three representative slices when imaging artifacts are present. (a) B_0 inhomogeneity (subject 9), (b) motion (subject 8) and (c) zipper (subject 6) artifacts. The rPCA-MWF shows reduced artefactual images. Note that the imaging

Results from a patient with demyelination (subject 10) is provided in Figure 4.12. Image from the MT scan is also shown for comparison. The rPCA-MWF map shows decreased MWF at the genu of corpus callosum which is in agree with the MT scan (green arrow). The complex model-based MWF map, however, showed unclear representation.

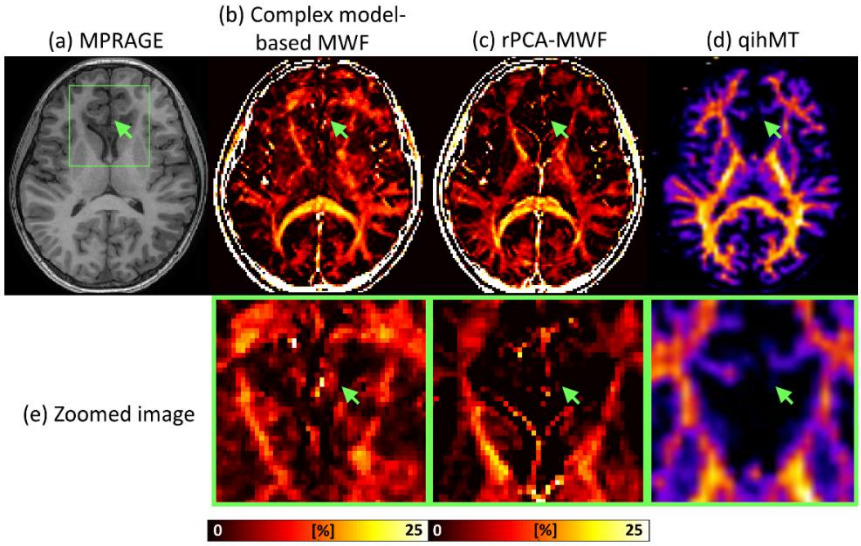

Figure 4.12. Patient exam results for a single slice (subject 10). (a) T1 weighted image, (b) Complex model-based MWF, (c) rPCA-MWF (d) qihMT image and (e) the magnified image for demyelinated region. Note that the demyelination (green arrow at genu) is observed in rPCA-MWF, which is in agreement with the anatomic and qihMT image.

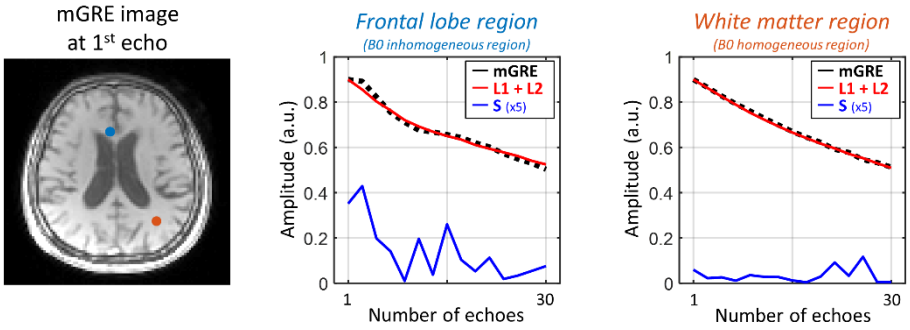

Figure 4.13. Effect of B0 inhomogeneity on S component. The mGRE signal, low-rank signal and sparse signal at B0 inhomogeneous and homogeneous region are plotted for subject 9. Note that the oscillating signal of S component was amplified for frontal region.

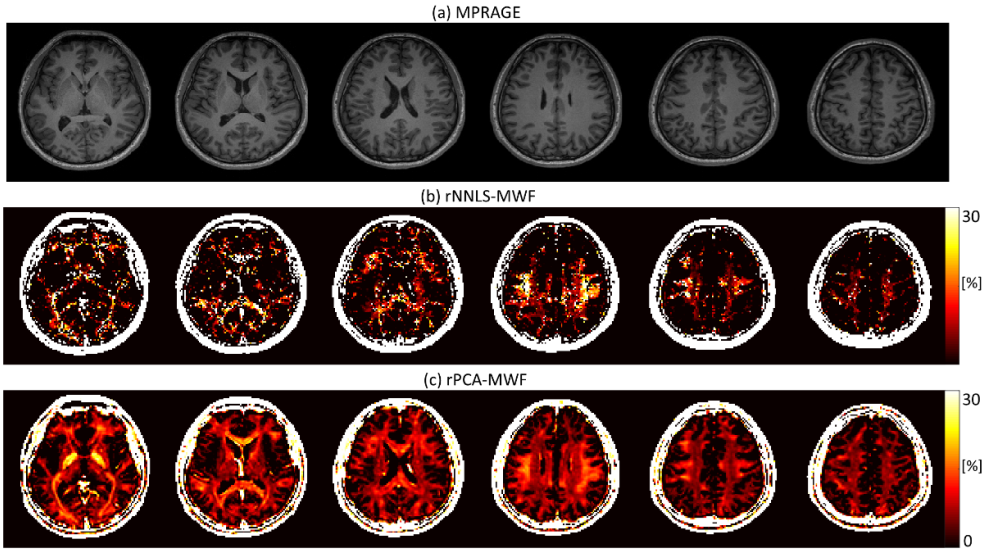

Figure 4.14. Six representative slices from healthy volunteer (subject 1). (a) MPRAGE, (b) rNNLS-MWF and (c) rPCA-MWF. The regularization parameters for rNNLS-MWF were set the same as in reference [64, 99]. Note that the rNNLS-MWF was reconstructed from current acquisition protocol (i.e., using 30 echoes with the last echo time of 31.81 ms) and does not provide a satisfactory result.

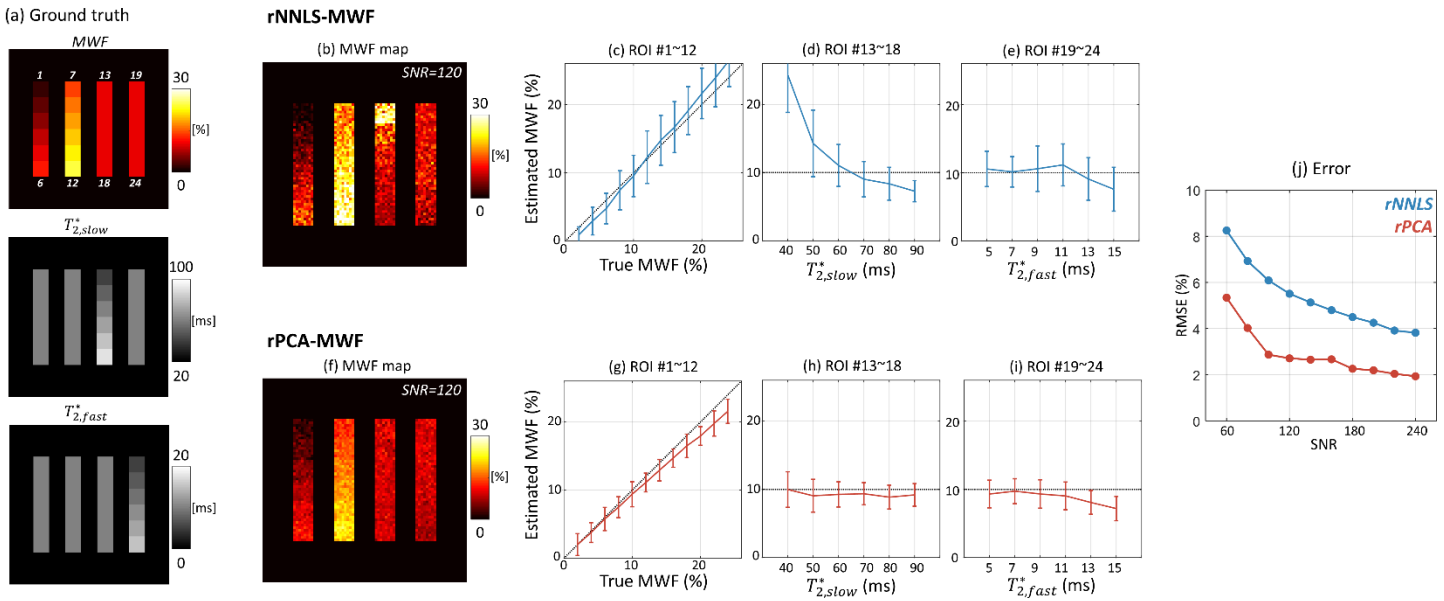

Figure 4.15. Numerical simulation of the MWF mapping for various $T_{2,\text{slow}}^*$, $T_{2,\text{fast}}^*$, and MWF. (a) Ground truth of the MWF, $T_{2,\text{slow}}^*$, and $T_{2,\text{fast}}^*$. The MWF map and ROI analysis using (b-e) rNNLS-MWF and (f-i) rPCA-MWF. Each column of ground truth indicates the ROI index 1~6, 7~12, 13~18 and 19~24 respectively. (j) Noise sensitivity of the MWF map. The regularization parameters were set the same as in reference [5, 44]. Note that the number of echoes was assumed to be 64.

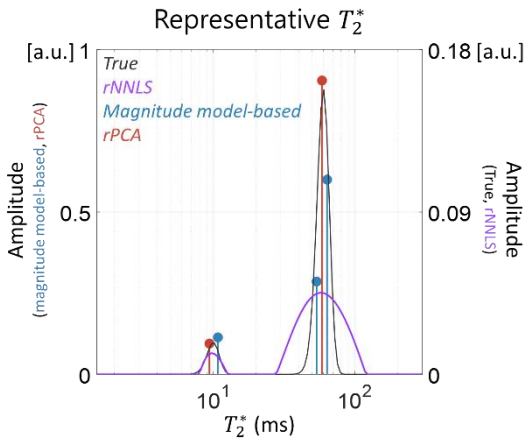

Figure 4.16. The representative T_2^* of rNNLS (purple), magnitude model-based MWF (blue) and rPCA-MWF (red) when true MWF (black) is 10% and SNR is 120 (ROI #5 in Figure 4.3). For each method, sum of amplitude of all T_2^* components was normalized to 1. Note that the representative T_2^* of rPCA-MWF is corresponded to the logarithmic center of spectral distribution of true T_2^*.

4.5 Discussion

In this study, I propose a data-driven source separation algorithm to map MWF from mGRE data as an alternative to conventional MWF mapping methods. By optimizing the standard rPCA algorithm for MWF mapping, the separation of two unit-rank components and sparse component allowed robust MWF mapping as well as differentiating myelin water and axonal/extracellular water signals.

The incorporation of NMF and hankelization allowed preservation of the physical

characteristics of tissue relaxation without a need for numerical modeling. First, NMF only allows additive combinations of signal sources by imposing non-negative constraint. This leads to the separated source signals to be represented in a more meaningful and interpretable feature [81]. Second, hankelization encourages exponential relaxation decays [86, 100]. The enforcement of the unit-rankness of each mono-exponential decay promotes the differentiation of axonal/extracellular water and myelin water signal.

One of the major advantages of rPCA-MWF is artifact robustness. In conventional GRE-MWI, the procedure to solve model-based MWF is a nonlinear regression, fitting the parameters of the model that minimizes least squares residuals. The deviations in the signal derived from artifact misfit the fitting parameters of the model. In proposed rPCA-MWF, by model-free source separation, the deviated signal due to artifact representing non-exponential decay are decomposed to the $\mathbf{S}$ component. Consequently, the $\mathbf{L}_1$ and $\mathbf{L}_2$ components are free from out-of-model signal sources and supports the improvement of the reproducibility in rPCA-MWF. In particular, the S component was amplified with oscillatory signal for B0 inhomogeneity dominant voxel (Figure 4.13). Although there was no numerical field inhomogeneity correction method implemented, the rPCA-MWF effectively separated non-exponentially decaying field inhomogeneity artifacts.

Another main advantage of rPCA-MWF is the noise robustness. In solving the objective function, the low rankness is enforced by singular value thresholding (SVT). The noisy subspace which yield small singular values are thresholded and the $\mathbf{L}_1$ and $\mathbf{L}_2$ components are represented by subspace with large singular values. Consequently, the rPCA-MWF

mapped using the $\mathbf{L_1}$ and $\mathbf{L_2}$ components achieves noise robustness. This supports the improvement of the reproducibility against noise in rPCA-MWF.

The amount of noise robustness of the $\mathbf{L_1}$ and $\mathbf{L_2}$ components is determined by the singular values of each component. As myelin water has lower signal than axonal/extracellular water, it is more susceptible to noise. Consequently, the robustness to noise was disrupted earlier for $\mathbf{L_2}$ (i.e., myelin water component) than $\mathbf{L_1}$ which results in mis-estimation of $\mathbf{L_2}$. The regularization parameters of rPCA-MWF were empirically determined to be robust for SNR ~100 typical of in-vivo mGRE acquisition, however it could be further adjusted for lower SNR.

Another benefit of rPCA-MWF is the range of echo time. rPCA-MWF stabilized using 30 echoes with the last echo of 32 ms. Meanwhile, a typical regularized non-negative least squares MWF (i.e., rNNLS-MWF) requires more than 64 echoes (i.e., the last echo being longer than the slowly-decaying T2* component) [64, 99]. Under the same hardware performances, TR of at least 80 ms is required to acquire 64 echoes. Consequently, the total scan time for rNNLS-MWF using 64 echoes is estimated to be 6 min 50 sec, which is 1.7 times longer than the scan time of this study. To avoid the increase of scan time and maintain a reasonable scan time for clinical application, a total of 30 echoes were acquired. In addition, it has been reported that mGRE-MWF can robustly estimate MWF with this decreased number of [63, 79]. As rNNLS-MWF does not perform well under the given acquisition protocol due to lack of echo signals, it was not thoroughly compared in this study (Figure 4.14 shows a demonstrative comparison of rNNLS-MWF and rPCA-MWF

under the current acquisition protocol). In addition, a simulation study using numerical phantom shows that the RMSE for rPCA-MWF is lower than rNNLS-MWF, even assuming 64 echo acquisition (Figure 4.15).

An additional benefit of the rPCA-MWF is the processing time. In our implementations, the complex model-based fitting and magnitude model-based fitting method required 69 secs and 31 secs per slice, respectively. The rPCA-MWF took 7.5 secs per slice and could cover whole 3D volume in under 5 mins.

Compared to multi-component model-based MWF, rPCA-MWF has two representative T_2^* for each voxel. The axonal water and extracellular water signals have T_2^* difference less than 20 ms at 7T, and therefore are difficult to differentiate [101]. In rPCA-MWF, these signals are represented as a single $\mathbf{L_1}$ component. Given a distribution of T_2^* values, the representative T_2^* of $\mathbf{L_1}$ and $\mathbf{L_2}$ corresponded to the logarithmic center of each distributed water pool (Figure 4.16) and to the literature T_2^* distribution in vivo (Figure 4.7b). This supports that the separated $\mathbf{L_1}$ and $\mathbf{L_2}$ represent intra-/extracellular water and myelin water component respectively.

A potential limitation of the current rPCA-MWF is that only magnitude information has been used and each separated component is based on the magnitude signal. The susceptibility differences along fiber orientation of mGRE data perturbate the effective resonant frequencies of the water compartments [102]. While considering frequency offsets could improve the GRE-MWI [67, 79], the lack of non-negativity and unit rankness of

complex-valued signal made it difficult to implement a complex-value based rPCA-MWF. The absence of consideration for these orientational dependencies resulted in overestimation in iron rich regions (e.g., globus pallidus in deep gray matter of Figure 4.8) [103, 104]. Extending rPCA-MWF to handle complex values in a different way is a future study.

Chapter 5

Robust Deep Autoencoder for Myelin Water Fraction Mapping using Multi-echo Gradient-echo Image

5.1 Motivation

5.1.1 Overview

In conventional myelin Myelin water imaging (MWI) is a promising biomarker that imaging demyelinating diseases such as multiple sclerosis [105-107], neuromyelitis optica [108, 109], dementia [110] and stroke [111]. In conventional MWI, multi-echo spin-echo (mSE) images are fitted to a numerical model in order to estimate multiple T2 components [59, 60]. Recently, multi-echo gradient-echo (mGRE) images have been implemented to estimate multiple T2* components, and it has been demonstrated that T2* signal has multiple water components [61-63, 68, 78, 79, 99]. Compared to mSE-MWI, mGRE-MWI has promising advantages such as low specific absorption rate, fast scan time, and insensitivity to B1 inhomogeneity [61]. However, anomaly sources such as physiological

noise and image artifacts disrupted the mGRE images and degraded the mGRE-MWI [66, 67, 112].

In previous studies, linear dimensionality reduction (LDR) techniques have been suggested to extract low dimensional features of MR signal [69, 71, 72, 74, 113-115]. By representing the high-dimensional dataset with intrinsic dimensionality (i.e., the minimum number of variables needed), the features which do not reside in the low dimensional subspace were excluded. The application of LDR varies including denoising in DWI [71, 114], denoising in fMRI [69], background signal removal in dynamic MRI [72] and denoising in MWI [113, 115], and artifact removal [74, 115, 116]. In particular, it has been validated that the mGRE images can be represented in linear low dimensional subspace by using robust principal component analysis (rPCA) [9, 117]. LDR in mGRE shows robustness for noise and artifacts, however, it cannot separate three water components corresponding to mGRE sources (i.e., myelin, axonal and intracellular water) in the complex-valued domain due to lack of orthogonality.

Recently, nonlinear dimensionality reduction (NLDR) techniques using deep neural networks have been developed to extract non-linear low dimensional features from the high dimensional dataset [7, 12, 118, 119]. An autoencoder, consisting of an encoder which maps the signal to a latent subspace and the decoder which maps the latent subspace to the signal [120, 121], extracts low dimensional feature at the latent layer (i.e., bottleneck layer). It has been suggested in MRI for compressed sensing reconstruction [122, 123], denoising dynamic contrast-enhanced (DCE) image [124], and denoising magnetic resonance

spectroscopic imaging (MRSI) [125].

I propose in this work an NLDR algorithm to estimate complex-valued low dimensional T2* components that captures the three water sources of mGRE signal. The proposed technique separates spatio-temporal mGRE images into three low dimensional features (referred to as $\mathbf{L}_1$, $\mathbf{L}_2$, and $\mathbf{L}_3$) and sparse feature (referred to as $\mathbf{S}$) for a complex-valued signal. Then, MWF map is suggested as the ratio of $\mathbf{L}_1$ to sum of $\mathbf{L}_1$, $\mathbf{L}_2$ and $\mathbf{L}_3$. I have demonstrated the proposed technique in healthy volunteers and clinical patients.

The outline of this Chapter is as follows. In Chapter 5.1.2-5.1.4, I give the previous study for mGRE-MWI using non-linear least squares algorithm (referred here as NLLS-MWF) and linear dimensionality reduction algorithm (referred here as LDR-MWF). Chapter 5.2 describes the proposed non-linear dimensionality reduction algorithm which is optimized for MWF mapping (referred here as NLDR-MWF). Chapter 5.3 and 5.4 present the methods and results of the simulation and in-vivo experiments. Finally, Chapter 5.5 provides the discussion and conclusion.

5.1.2 Complex model-based MWF (NLLS-MWF)

The voxel-wise T_2^* decaying signal, $s(t)$, is fitted to the complex three-component model as follows [63]:

$$s(t) = (A_{my}e^{-(1/T_{2,ex}^* + i2\pi\Delta f_{bg+my})t} + A_{ax}e^{-(1/T_{2,ex}^* + i2\pi\Delta f_{bg+ax})t}$$

$$+A_{ex}e^{-(1/T_{2,ex}^{*}+i2\pi\Delta f_{bg+ex})t})e^{-i\varphi_0} \quad (5.1)$$

where A_{my}, A_{ax} and A_{ex} are the amplitude of the three water component, $T_{2,my}^{*}, T_{2,ax}^{*}$ and $T_{2,ex}^{*}$ are T_2^{*} value of the three water component, $\Delta f_{bg+my}, \Delta f_{bg+ax}$ and Δf_{bg+ex} are the frequency offset of the three water component plus the sum of background frequency offset, φ_0 is the B_1^{+} phase offset. The parameters are estimated by minimizing the nonlinear least-squares errors using an iterative nonlinear curve-fitting algorithm [63, 68, 79]. Then, MWF is estimated as the ratio of the myelin water component to the total water component (i.e., $A_{my}/(A_{my}+A_{ax}+A_{ex})$). The initial values and bounds of the fitted parameters are set the same as in [79].

5.1.3 Linear Dimensionality Reduction for mGRE images (LDR-MWF)

I denote matrices by boldface uppercase letters, operators by lightface uppercase letters, vectors by boldface lowercase italics, constants by lightface uppercase italics. $\mathbb{C}$, $\mathbb{R}$ and $\mathbb{R}_+$ represent a set of complex, real and positive-real values, respectively.

In advance of implementing LDR, the mGRE data $m(\cdot)$ is represented to the spatio-temporal Casorati matrix as follows:

$$\mathbf{M}(\boldsymbol{r},t)=\begin{bmatrix} m(r_1,t_1) & m(r_1,t_2) & \cdots & m(r_1,t_{N_t}) \\ m(r_2,t_1) & m(r_2,t_2) & \cdots & m(r_2,t_{N_t}) \\ \vdots & \vdots & \ddots & \vdots \\ m(r_{N_s},t_1) & m(r_{N_s},t_2) & \cdots & m(r_{N_s},t_{N_t}) \end{bmatrix} \quad (5.2)$$

where $\mathbf{M} \in \mathbb{R}^{N_s \times N_t}$, N_s is the number of samples (i.e., number of voxels) and N_t is the number of contrasts (i.e., number of echoes). The LDR-MWF algorithm separates the spatio-temporal mGRE data into two rank-1 components (i.e., fast-decaying ($\mathbf{L}_1$) and slowly-decaying ($\mathbf{L}_2$)) and sparse component (i.e., residual artifact signal ($\mathbf{S}$)) by solving an optimization problem as follows [115]:

$$\min_{\mathbf{L}_1,\mathbf{L}_2,\mathbf{S}} \left\| \mathbf{M} - \sum_{i=1}^{2} \mathbf{L}_i - \mathbf{S} \right\|_2^2 + \sum_{i=1}^{2} \mu_i \|\mathcal{H}(\mathbf{L}_i)\|_* + \rho \|\Psi(\mathbf{S})\|_1 \tag{5.3}$$

where $\mathbf{L}_1, \mathbf{L}_2, \mathbf{S} \in \mathbb{R}_+^{N_s \times N_t}$, $\|\cdot\|_*$ denotes the nuclear norm, $\|\cdot\|_1$ denotes the ℓ_1-norm, $\mathcal{H}(\cdot)$ denotes temporal hankelization operator, $\Psi(\cdot)$ denotes temporal sparsifying operator (1D FFT in the echo domain). μ_1, μ_2 and ρ denote regularization parameters for low-rankness and sparsity respectively. Equation (5.3) is solved using the alternating direction method of multipliers (ADMM) Goldstein and Osher [93]. The MWF can be calculated as the ratio of a fast-decaying rank-1 component to the total rank-1 component at TE1. The local patch extraction operator from the original algorithm was omitted for simplification.

Compared to NLLS-MWF, LDR-MWF provided the robust estimation of MWF map by separating low dimensional feature (i.e., exponential decaying) and sparse feature (i.e., artifacts) [115]. However, even though additional operators for enforcing the low dimensionality (e.g., nonnegative matrix factorization (NMF) and hankelization), it was insufficient to separate three low-dimensional features which correspond to three water components (i.e., myelin, extra and axonal water). Consequently, LDR-MWF extracted

only two rank-1 components which correspond to slowly-decaying (i.e., intra-/extra-cellular water signal) and fast-decaying signal (i.e., myelin water signal) respectively. Also, each low dimensional feature of LDR-MWF was constrained on the magnitude domain, and complex attribute of low dimensional features could not be considered.

5.1.4 Deep Autoencoder

A deep autoencoder (DAE) is a feed-forward neural network with fully connected stacked encoding and decoding layers (Figure 5.1.a). The network is trained to minimize the mean squared error between the input and output of the network. The training allows the bottleneck layer to provide a low dimensional representation that preserves the data feature of the entire training dataset [7, 12].

Autoencoder is consists of two-part: encoder and decoder. The encoder maps the signal to a latent subspace and the decoder which maps the latent subspace to the signal as [120, 121]:

$$h = \mathcal{E}(m_{ns}(t); \theta_{\mathcal{E}}) \tag{5.4a}$$

$$\hat{m} = \mathcal{D}(h; \theta_{\mathcal{D}}) = \mathcal{D}(\mathcal{E}(m_{ns}(t); \theta_{\mathcal{E}}); \theta_{\mathcal{D}}) \tag{5.4b}$$

where ns denotes an index of spatial instances, $m_{ns}(t)$ denotes temporal signal at spatial pixel ns (i.e., $m(r_{ns}, t)$), h denotes latent feature, $\mathcal{E}$ and $\mathcal{D}$ denote encoder and decoder mapping respectively, $\theta_{\mathcal{E}}$ and $\theta_{\mathcal{D}}$ denote weights and biases of entire multilayers for encoder and decoder respectively. Training is finding $\theta_{\mathcal{E}}$ and $\theta_{\mathcal{D}}$ while

minimizing RMSE error as:

$$\{\hat{\theta}_{\mathcal{E}}, \hat{\theta}_{\mathcal{D}}\} = \underset{\theta_{\mathcal{E}}, \theta_{\mathcal{D}}}{\operatorname{argmin}} \frac{1}{N_s} \sum_{ns=1}^{N_s} \| m_{ns}(t) - \mathcal{D}(\mathcal{E}(m_{ns}(t); \theta_{\mathcal{E}}); \theta_{\mathcal{D}}) \|_2^2 \quad (5.5)$$

where N_s denotes the number of training samples. Note that the voxel-wise multi-echo signals are feed into the network.

5.2 Proposed Methods

5.2.1 Pre-trained model for initialization

Recognizing that mGRE signal is observed as multiple exponential T2* decaying signals in Eq. 5.1 [63, 79], an initialization strategy to estimate each mono-exponential T2* decaying signals using a fully connected encoder was proposed. In LDR-MWF, a model-free initialization approach using non-negative double singular value decomposition (NNDSVD) was unable to distinguish axonal and extracellular water signals. As an alternative to NNDSVD, each water component estimation network was trained using complex three-component model. Several studies showed feasibility for using a model-based synthesized signal for training [125-128].

The input signal was generated as in Eq. 5.1 and the label of each source signal, s_i, was generated as:

$$s_i(t) = A_i e^{-(1/T_{2,i}^* + i2\pi\Delta f_i)t} \quad (5.6)$$

where i denotes the index of each water component. The training dataset was generated by simulating $s_i(t)$ based on empirical distribution. The parameters for each mono-exponential signal was set based on empirical data as [126]: $A_1 = (10, 2)$, $A_2 = (60, 10)$, $A_3 = (30, 6)$, $T^*_{2,1} = (10, 2)$, $T^*_{2,2} = (72, 10)$, $T^*_{2,3} = (48, 6)$, $\Delta f_1 = (-10, 20)$, $\Delta f_2 = (-10, 10)$, $\Delta f_3 = (0,0)$.

The training is carried out to minimize RMSE between input and label and is represented as:

$$\underset{\theta_i}{\operatorname{argmin}} \|s_i(t) - f(s(t); \theta_i)\|_2^2 \quad (for\ i = 1,2,3) \tag{5.7}$$

where θ_i denotes the parameterized weights and bias for all layers. The network had $2N_t$ neurons in the input layer and the output layer. Between the input and output layers, 5 hidden layers were constructed with 500 fully connected neurons, respectively. A rectified linear unit (ReLU) with 0.2 was used as a nonlinear activation function and Adam optimizer with learning rate of 1e-4 was used.

The trained parameters of each water component estimation network were then integrated into the initialization step of the proposed NLDR-MWF algorithm.

5.2.2 Algorithm of the proposed method (NLDR-MWF)

The original rDAE separates the signal sources into a low-dimensional component, **L**, and a sparse component, **S**, by solving the constrained optimization problem as [13]:

$$\min_{\theta_{\mathcal{E}},\theta_{\mathcal{D}},\mathbf{S}} \frac{1}{N_s}\sum_{ns=1}^{N_s} \|\mathbf{L}(r_{ns},t) - \mathcal{D}(\mathcal{E}(\mathbf{L}(r_{ns},t);\theta_{\mathcal{E}});\theta_{\mathcal{D}})\|_2 + \rho\|\Psi(\mathbf{S})\|_1$$

$$\text{s.t. } \mathbf{M} - \mathbf{L} - \mathbf{S} = 0 \tag{5.8}$$

where $\mathbf{L}(r_{ns},t)$ denotes temporal signal at spatial pixel ns. Note that the input feed into autoencoder pixel-wisely and the constraint is regularized for entire pixels. Equation (5.8) is solved by using the concept of alternating direction method of multipliers (ADMM) [11, 93] and Dykstra's alternating projection method [14].

In this study, I present optimized NLDR method that separates three low-dimensional sources and a sparse source from mGRE images. With the guide of model based T2* source separation which was mentioned in Chapter 5.2.1, a modified rDAE to separate three distinct sources from mGRE data is presented. The LDR-MWF separates the mGRE signal sources into two low-rank component and a sparse component. In this study, the signal source of mGRE data was separated into three low-dimensional signals and sparse signal. The optimization problem is defined as:

$$\min_{\theta_{\mathcal{E},\mathrm{i}},\theta_{\mathcal{D},\mathrm{i}},\mathbf{S}} \sum_{\mathrm{i}=1}^{3}\frac{1}{N_s}\sum_{ns=1}^{N_s} \left\|\mathbf{L}_i(r_{ns},t) - \mathcal{D}\left(\mathcal{E}\left(\mathbf{L}_i(r_{ns},t);\theta_{\mathcal{E},\mathrm{i}}\right);\theta_{\mathcal{D},\mathrm{i}}\right)\right\|_2 + \rho\|\Psi(\mathbf{S})\|_1$$

$$\text{s.t. } \mathbf{M} - \sum_{\mathrm{i}=1}^{3}\mathbf{L}_{\mathrm{i}} - \mathbf{S} = 0 \tag{5.9}$$

where ρ denotes regularization parameters for sparsity. $\mathcal{E}$ and $\mathcal{D}$ denote encoding and decoding layers with a dimension of $2N_t - 30 - 5 - 30 - 2N_t$. ReLU activation functions were used in the hidden layers except for the last layer. The following steps were performed iteratively in our proposed algorithm:

Update initialized low-dimensional components by projecting on pre-trained model f as:

$$\mathbf{L}_1{}^{(\mathrm{k})} = f\left(\mathbf{M} - \mathbf{S}^{(\mathrm{k})}, \theta_1\right) \tag{5.10a}$$

$$\mathbf{L}_2{}^{(\mathrm{k})} = f\left(\mathbf{M} - \mathbf{S}^{(\mathrm{k})}, \theta_2\right) \tag{5.10b}$$

$$\mathbf{L}_3{}^{(\mathrm{k})} = f\left(\mathbf{M} - \mathbf{S}^{(\mathrm{k})}, \theta_3\right) \tag{5.10c}$$

where θ_1, θ_2, and θ_3 denote all the weights and bias of pre-trained model in Chapter 5.2.1. Note that these parameters are fixed during solving optimization problem.

Update DAE model parameters by minimizing the RMSE between the input and the output signals of each low dimensional component as:

$$\left\{\theta_{\mathcal{E},1}{}^{(\mathrm{k})}, \theta_{\mathcal{D},1}{}^{(\mathrm{k})}\right\} = \underset{\theta_{\mathcal{E},1},\theta_{\mathcal{D},1}}{\operatorname{argmin}} \frac{1}{N_s}\sum_{ns=1}^{N_s}\left\|\mathbf{L}_1{}^{(\mathrm{k})}(r_{ns}, t) - \mathcal{D}\left(\mathcal{E}\left(\mathbf{L}_1{}^{(\mathrm{k})}(r_{ns}, t); \theta_{\mathcal{E},1}\right); \theta_{\mathcal{D},1}\right)\right\|_2$$

(5.11a)

$$\left\{\theta_{\mathcal{E},2}{}^{(\mathrm{k})}, \theta_{\mathcal{D},2}{}^{(\mathrm{k})}\right\} = \underset{\theta_{\mathcal{E},2},\theta_{\mathcal{D},2}}{\operatorname{argmin}} \frac{1}{N_s}\sum_{ns=1}^{N_s}\left\|\mathbf{L}_1{}^{(\mathrm{k})}(r_{ns}, t) - \mathcal{D}\left(\mathcal{E}\left(\mathbf{L}_1{}^{(\mathrm{k})}(r_{ns}, t); \theta_{\mathcal{E},2}\right); \theta_{\mathcal{D},2}\right)\right\|_2$$

(5.11b)

$$\left\{\theta_{\mathcal{E},3}{}^{(\mathrm{k})}, \theta_{\mathcal{D},3}{}^{(\mathrm{k})}\right\} = \underset{\theta_{\mathcal{E},3},\theta_{\mathcal{D},3}}{\operatorname{argmin}} \frac{1}{N_s}\sum_{ns=1}^{N_s}\left\|\mathbf{L}_1{}^{(\mathrm{k})}(r_{ns}, t) - \mathcal{D}\left(\mathcal{E}\left(\mathbf{L}_1{}^{(\mathrm{k})}(r_{ns}, t); \theta_{\mathcal{E},3}\right); \theta_{\mathcal{D},3}\right)\right\|_2$$

(5.11c)

Update low dimensional components using DAE model parameters in previous step,

$\{\theta_{\mathcal{E},i}{}^{(k)}, \theta_{\mathcal{D},i}{}^{(\mathrm{k})}\}_{i=1}^{3}$, as:

$$\mathbf{L}_1{}^{(\mathrm{k}+1)} = \mathcal{D}\left(\mathcal{E}\left(\mathbf{L}_1{}^{(\mathrm{k})}; \theta_{\mathcal{E},1}{}^{(\mathrm{k})}\right); \theta_{\mathcal{D},1}{}^{(\mathrm{k})}\right) \tag{5.12a}$$

$$\mathbf{L_2}{}^{(\mathrm{k}+1)} = \mathcal{D}\left(\mathcal{E}\left(\mathbf{L_2}{}^{(\mathrm{k})}; \theta_{\mathcal{E},2}{}^{(\mathrm{k})}\right); \theta_{\mathcal{D},2}{}^{(\mathrm{k})}\right) \tag{5.12b}$$

$$\mathbf{L}_3{}^{(\mathrm{k}+1)} = \mathcal{D}\left(\mathcal{E}\left(\mathbf{L}_3{}^{(\mathrm{k})}; \theta_{\mathcal{E},3}{}^{(\mathrm{k})}\right); \theta_{\mathcal{D},3}{}^{(\mathrm{k})}\right) \tag{5.12c}$$

Update sparsity feature with fixed $\mathbf{L}_1$, $\mathbf{L}_2$, and $\mathbf{L}_3$ using proximal operator as:

$$\mathbf{S}^{(\mathrm{k}+1)} = \mathrm{ST}_{\rho}(\mathbf{M} - \mathbf{L}_1{}^{(\mathrm{k}+1)} - \mathbf{L}_2{}^{(\mathrm{k}+1)} - \mathbf{L}_3{}^{(\mathrm{k}+1)}) \tag{5.13}$$

where ST_{ρ} denotes soft thresholding operator [9, 117].

Two types of convergence were investigated to evaluate convergence to input and convergence to a fixed point as [13]:

$$c1 = \left\|\mathbf{M} - \sum_{\mathrm{i}=1}^{3} \mathbf{L}_{\mathrm{i}}{}^{(\mathrm{k}+1)} - \mathbf{S}^{(\mathrm{k}+1)}\right\|_2 / \|\mathbf{X}\|_2 \tag{5.14a}$$

$$c2 = \frac{\left\|\left(\sum_{\mathrm{i}=1}^{3} \mathbf{L}_{\mathrm{i}}{}^{(\mathrm{k}+1)} + \mathbf{S}^{(\mathrm{k}+1)}\right) - \left(\sum_{\mathrm{i}=1}^{3} \mathbf{L}_{\mathrm{i}}{}^{(\mathrm{k})} + \mathbf{S}^{(\mathrm{k})}\right)\right\|_2}{\left\|\sum_{\mathrm{i}=1}^{3} \mathbf{L}_{\mathrm{i}}{}^{(\mathrm{k})} + \mathbf{S}^{(\mathrm{k})}\right\|_2} \tag{5.14b}$$

The regularization parameters and the convergence tolerance were empirically set as follows: $\rho = 10^{-2}$, $\epsilon = 10^{-4}$.

Finally, the MWF map was estimated as the ratio of the myelin water originated low-dimensional component to the total low-dimensional components at TE_1:

$$\mathrm{MWF}(r) = \frac{\mathbf{L}_1(r, TE_1)}{\sum_{\mathrm{i}=1}^{3} \mathbf{L}_{\mathrm{i}}\,(r, TE_1)} \times 100\ (\%) \tag{5.15}$$

A summary of the iteration process is described in Table 5.1. The schematic architecture of NLDR-MWF is depicted in Figre 5.1.

Task:
Find $\mathbf{L}_1$, $\mathbf{L}_2$, $\mathbf{L}_3$ and $\mathbf{S}$ minimizing Eq. (5)
Initialization:
k = 0, $\mathbf{S}^{(0)} = \mathbf{0}$,
while "not converged" **and** "k < 100" **do**
Step 1: Update $\left\{\mathbf{L}_i{}^{(\mathrm{k})}\right\}_{i=1}^{3}$ by projecting $\mathbf{M} - \mathbf{S}^{(\mathrm{k})}$ to f
Step 2: Update $\left\{\theta_{\mathcal{E},i}{}^{(k)}, \theta_{\mathcal{D},i}{}^{(\mathrm{k})}\right\}_{i=1}^{3}$ by solving Eq.11
Step 3: Update $\left\{\mathbf{L}_i{}^{(\mathrm{k}+1)}\right\}_{i=1}^{3}$ by solving Eq.12
Step 4: Update $\mathbf{S}$ by solving Eq. 13
Step 5: Increase the iteration number k
end
Output:
$\widehat{\mathbf{L}_1} = \mathbf{L}_1{}^{(\mathrm{k}+1)}$, $\widehat{\mathbf{L}_2} = \mathbf{L}_2{}^{(\mathrm{k}+1)}$, $\widehat{\mathbf{L}_3} = \mathbf{L}_3{}^{(\mathrm{k}+1)}$, $\hat{\mathbf{S}} = \mathbf{S}^{(\mathrm{k}+1)}$

Table 5.1. NLDR-MWF algorithm

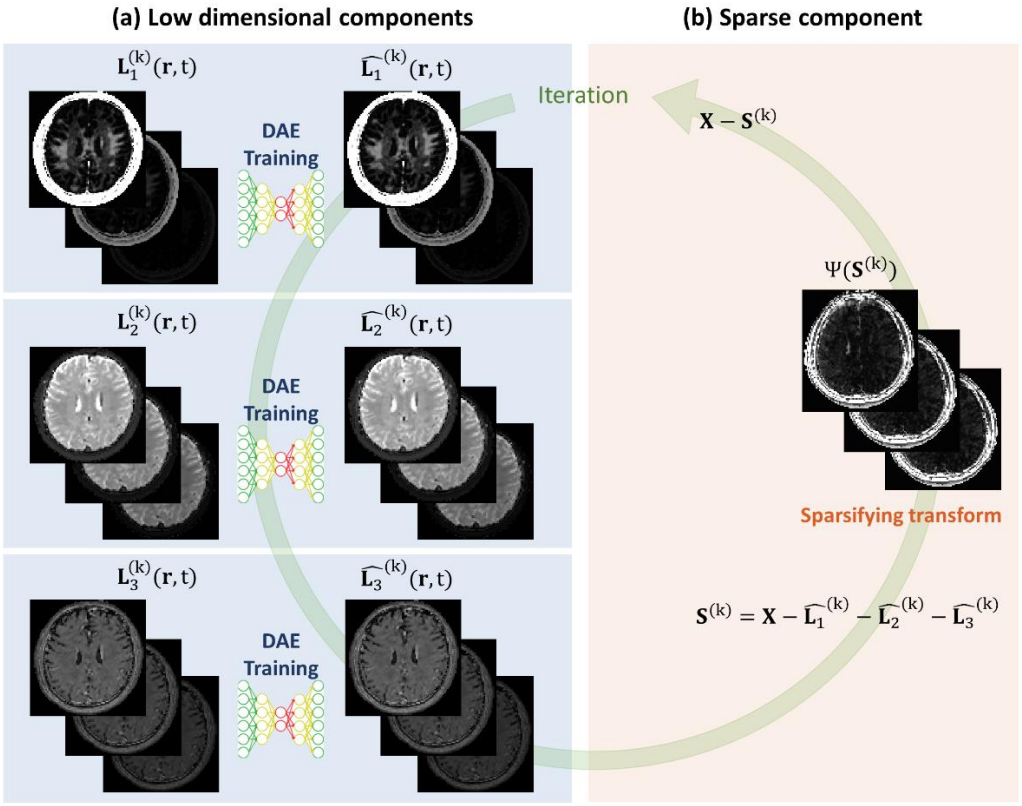

Figure 5.1. The schematic architecture of NLDR-MWF for spatio-temporal mGRE images. (a) Deep autoencoders trained to extract nonlinear low dimensional features at the bottleneck layer. (b) Sparsifying transform to the residual of input ($\mathbf{M}$) and low dimensional component ($\mathbf{L_1}$, $\mathbf{L_2}$, and $\mathbf{L_3}$). Note that the DAEs are trained voxel-wisely and subject-wisely.

5.2.3 Numerical Simulations

Numerical simulations were conducted to evaluate the performance of NLLS-MWF,

LDR-MWF, and NLDR-MWF for various situations.

The hollow cylinder fiber model was used to characterize the effect of fiber anisotropy on the evolution of the magnitude and phase signal according to the different orientation angle [102]. Here, the fiber orientation (FO) was set as an angle between the white matter fiber and the main field. The detail parameters were set the same as in [79].

An analytic phantom composed of varying MWF and FO was simulated. MWF was varied from 2% to 20% with a step size of 2% and RA was varied from 0° to 90° with a step size 30°.

The complex-valued Gaussian noise was added so that the SNR at the first TE varied from 80 to 200 with a step size of 20. A series of Monte-Carlo simulations were performed with 200 repetitions.

The estimated MWF was investigated for each ROI and the RMSE between true MWF map and estimated MWF map was evaluated for each SNR.

5.2.4 In-vivo Experiments

All MR imaging experiments were performed on 3 Tesla clinical scanners (Tim Trio/Skyra, Siemens, Erlangen, Germany). All examination was performed with approval from the institution's ethical review board and all subjects provided signed, informed consent before participation.

The 3D mGRE imaging parameters were FOV = 256×256×80mm3, spatial resolution = 2×2×2 mm3, TR = 46 ms, TE1 = 1.65 ms, ΔTE = 1.04 ms, # of echoes = 30, flip-angle = 20°, bandwidth = 1560 Hz/pixel and total scan time = 3min 55sec.

For fiber orientation reference, DTI was acquired with TR = 7113 ms, TE = 91 ms, diffusion direction = 30, b-value = 600 s/mm2. For anatomical reference, T1-weighted sagittal 3D MPRAGE (1.0 mm isotropic) was acquired.

Data were acquired from 6 subjects. Subjects 1-4 were healthy volunteers (age 25-29). Subject 5 and subject 6 were patients with mild cognitive impairment (male, age 63) and Alzheimer's disease (female, age 71) confirmed by a radiologist, respectively. The ringing artifacts were corrupted for patients. Subject 3 and subject 4 were artifact corrupted cases for zipper and B0 inhomogeneity, respectively.

The mean and STD of perpendicular and parallel ROIs were calculated for four healthy subjects. The ROIs were selected based on DTI. Student's t-test was performed to evaluate the statistical significance of LDR-MWF against others. The significance level was set to 0.05. Additionally, the mean and STD of six ROIs were calculated for four healthy subjects. The ROIs were selected based on MPRAGE.

The component-wise analysis was conducted for each low dimensional component from NLDR-MWF using the mono-exponential model in Eq. 5.6a. The initial values and bounds were set the same as NLLS-MWF in Chapter 5.1.2.

5.3 Results

5.3.1 Numerical Simulations

The simulation results of MWF mapping for various MWF and fiber orientation are shown in Figure 5.2. The STD of LDR-MWF and NLDR-MWF was reduced by about 40% compared to NLLS-MWF. For FA with 0° and 30°, NLLS-MWF, LDR-MWF, and NLDR-MWF showed similar results. For FA with 60° and 90°, on the other hand, LDR-MWF showed significant underestimation (green arrow in Figure 5.2c). The ROI analysis for simulation is shown in Figure 5.3. For FA with 0° and 30°, NLLS-MWF was underestimated about 10% and LDR/NLDR-MWF was underestimated about 15% (Figure 5.3a and 5.3b). For FA with 60° and 90°, the linearity of estimated MWF using NLLS-MWF and LDR-MWF deviated (Figure 5.3c and 5.3d). NLLS-MWF fluctuated when true MWF is 8% to 12% and LDR-MWF faded away when true MWF is less than 6%.

The RMSE of the estimated MWF map is shown in Figure 5.4. The RMSE of NLDR-MWF was reduced by about 40% and 20% compared to NLLS-MWF and LDR-MWF, respectively (Figure 5.4a). For FA with 0° and 30°, the RMSE of LDR-MWF and NLDR-MWF was similar (Figure 5.4b and 5.4c). For FA with 60° and 90°, the RMSE of LDR-MWF was over NLLS-MWF (Figure 5.4d and 5.4e). It supports the fiber robustness of NLDR-MWF

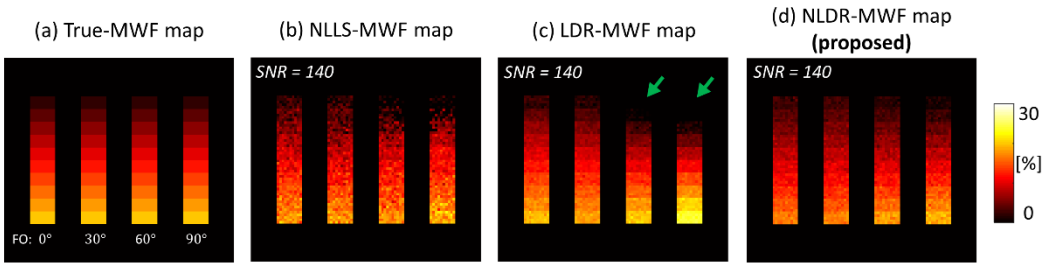

Figure 5.2. Numerical simulation of MWF mapping for various MWF and FA. (a) True MWF map, (b) NLLS-MWF map, (c) LDR-MWF map and (d) NLDR-MWF map. Note that the LDR-MWF is abnormally underestimated for low MWF with high FA. ROI analysis and linear regression for each FA is depicted in Figure 5.3.

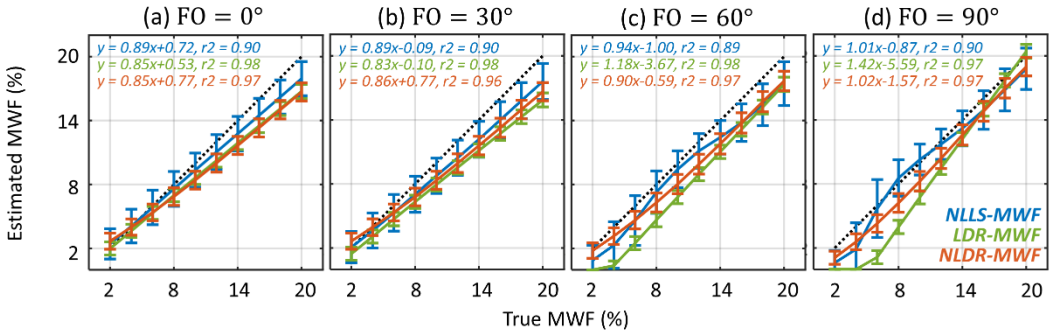

Figure 5.3. ROI analysis of MWF map in numerical simulation. (a) FO = 0° region, (b) FO = 30° region, (c) FO = 60° region, and (d) FO = 90° region. ROI analysis and linear regression were evaluated for each FOs corresponding to single column in Figure 5.2.

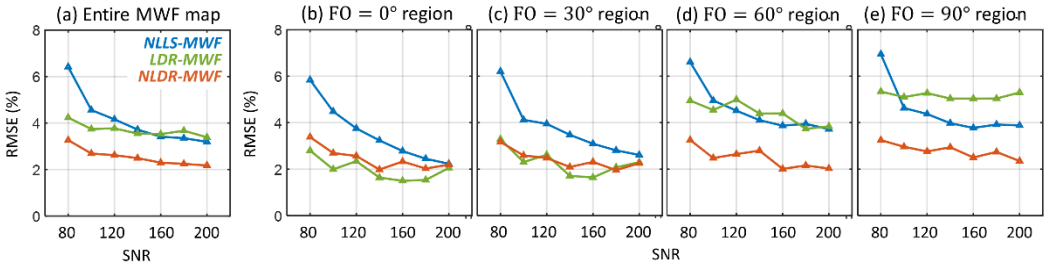

Figure 5.4. Noise sensitivity of MWF map in simulation. RMSE according to SNR for (a) entire MWF map, (b) FO = 0° region, (c) FO = 30° region, (d) FO = 60° region, and (e) FO = 90° region. Note that RMSE for each FA region is evaluated for single column in Figure 5.2.

5.3.2 In-vivo Experiments

The effect of fiber orientation to MWF value is shown in Figure 5.5. For perpendicular ROI with low MWF value under 6%, the LDR-MWF was reduced by more than 25% compared to NLLS-MWF and NLDR-MWF ($p<0.05$). For parallel ROI with a low MWF value under 6%, there was no significant difference. It supports the robustness of the fiber orientation of NLDR-MWF in simulation. The perpendicular and parallel ROIs of each healthy subject is depicted in Figure 5.6.

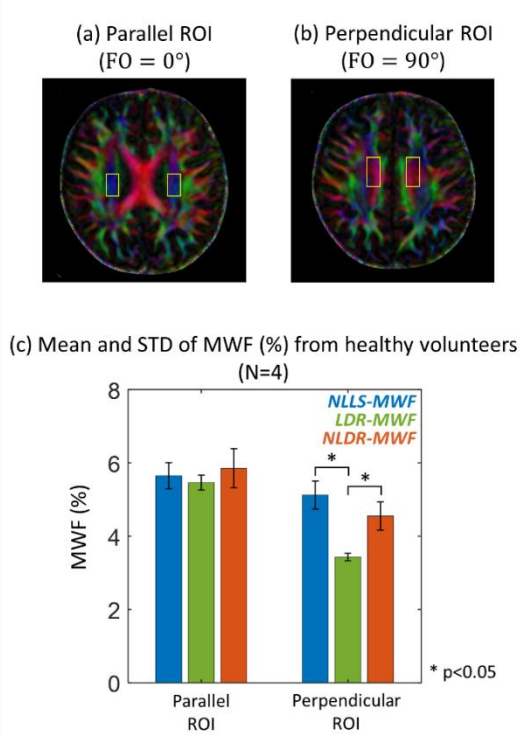

Figure 5.5. Effect of fiber orientation to MWF map in in-vivo (subject1). (a) perpendicular ROI and (b) parallel ROI (yellow box) with low MWF (<6%). (c) Mean and STD of MWF from healthy volunteers (N=4). The significant level was set to 0.05.

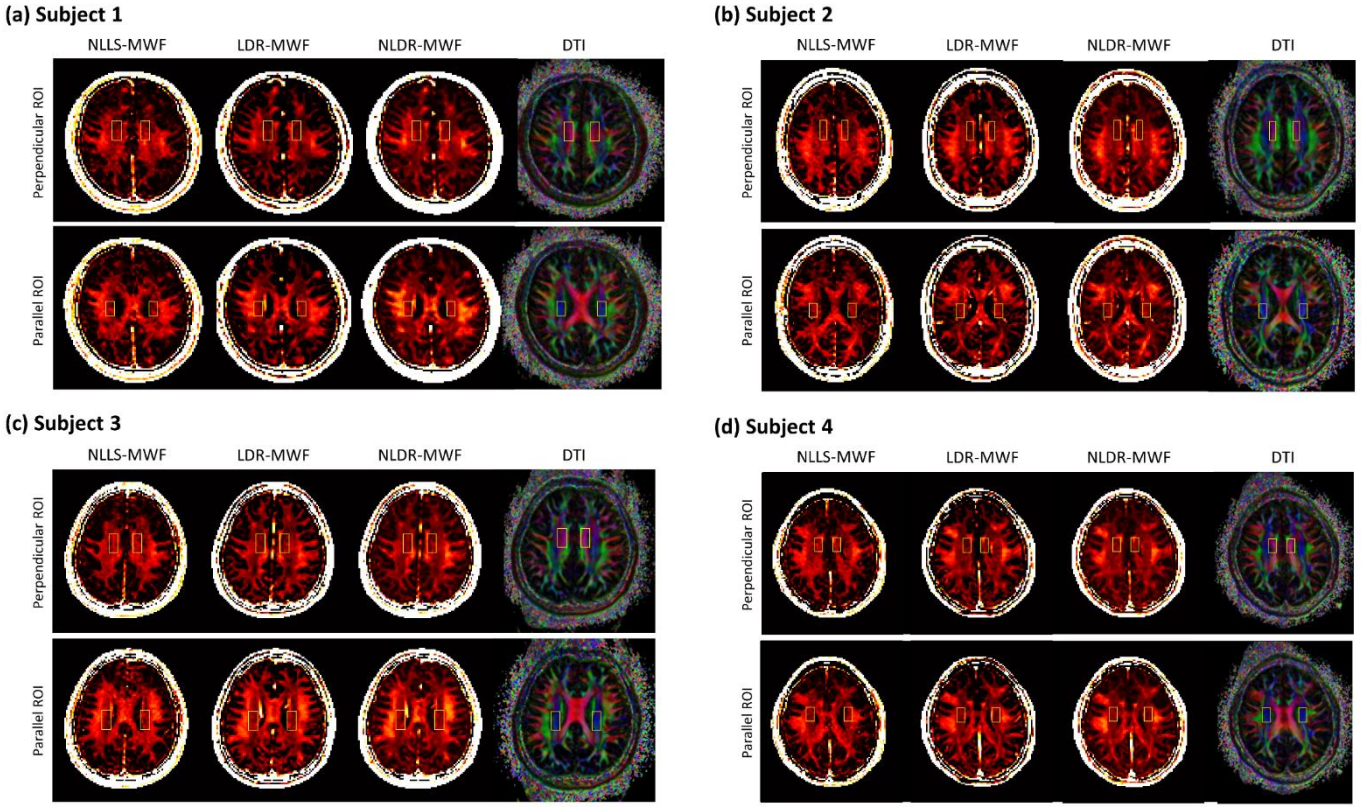

Figure 5.6. Perpendicular ROIs and parallel ROIs (yellow box) with low MWF (<6%). (a) subject 1, (b) subject 2, (c) subject 3, and (d) subject 4.

Representative MWF maps from subject 1 are shown in Figure 5.7. The boundary of white matter was more clearly visualized in LDR/NLDR-MWF compared to NLLS-MWF. For the frontal lobe region, LDR/NLDR-MWF was well corresponded to MRPAGE, while NLLS-MWF was corrupted.

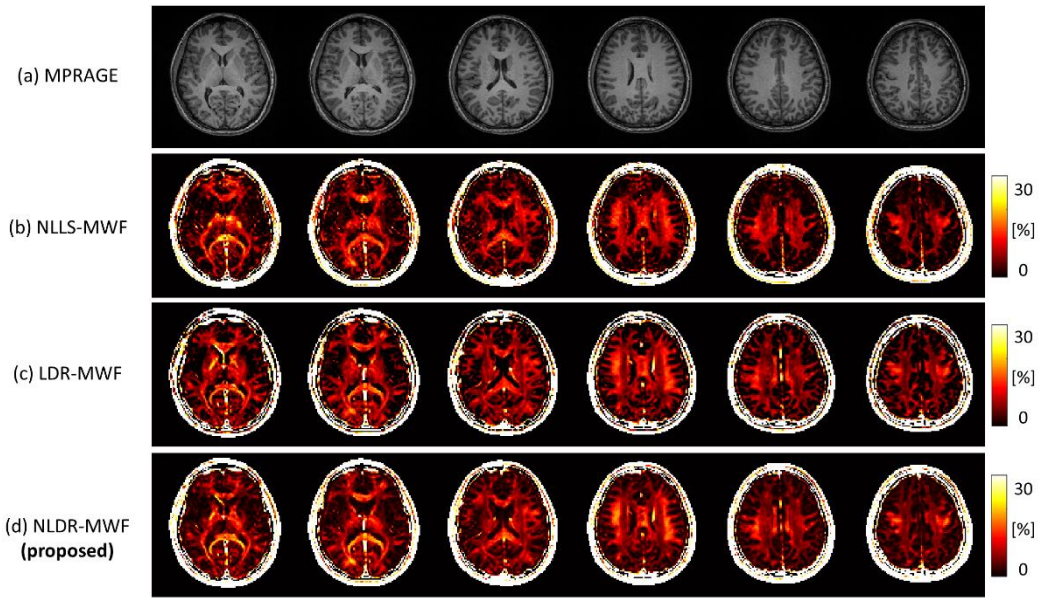

Figure 5.7. Six representative slices from healthy volunteer (subject1). (a) MPRAGE, (b) NLLS-MWF, (c) LDR-MWF, and (d) NLDR-MWF.

Artifact corrupted cases are shown in Figure 5.8. Subjects 5 and 6 showed a ringing artifact. Subjects 3 and 4 showed zipper and B0 inhomogeneity artifacts, respectively. In Figure 5.8a and 8b, ringing artifacts in NLLS-MWF are reduced in LDR-MWF and NLDR-MWF. In Figure 5.8c and 5.8d, a zipper artifact and B0 inhomogeneity artifact in NLLS-MWF are reduced in LDR-MWF and NLDR-MWF. The MWF maps from other slices are shown in Figure 5.9 - 5.11.

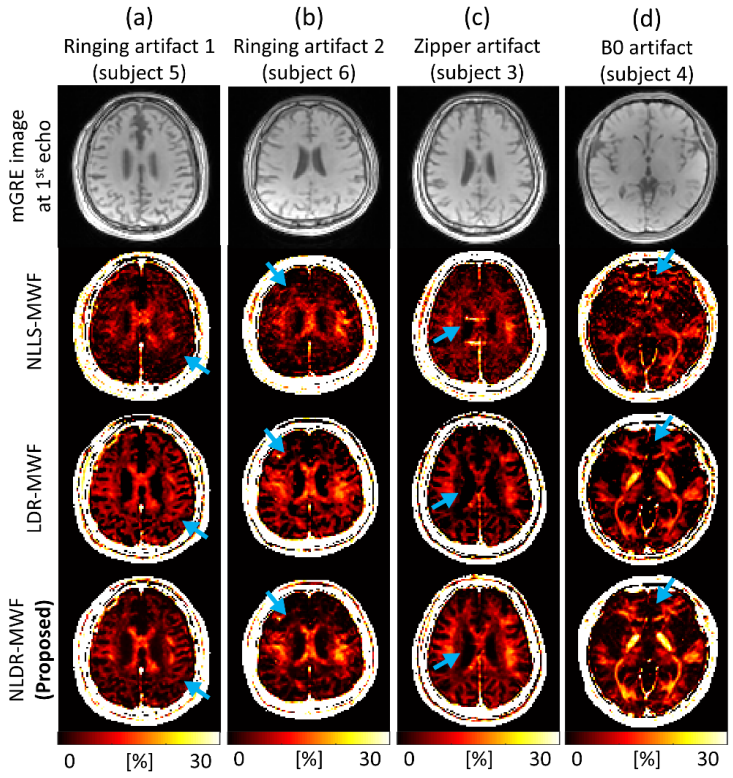

Figure 5.8. Single representative slice when imaging artifacts are corrupted. (a) Ringing artifact 1, (b) Ringing artifact 2, (c) Zipper artifact, and (d) B0 inhomogeneity artifact were corrupted, respectively. Note that blue arrow indicates each artifact. Additional four consecutive slices are provided in Figure 5.9 - 5.11.

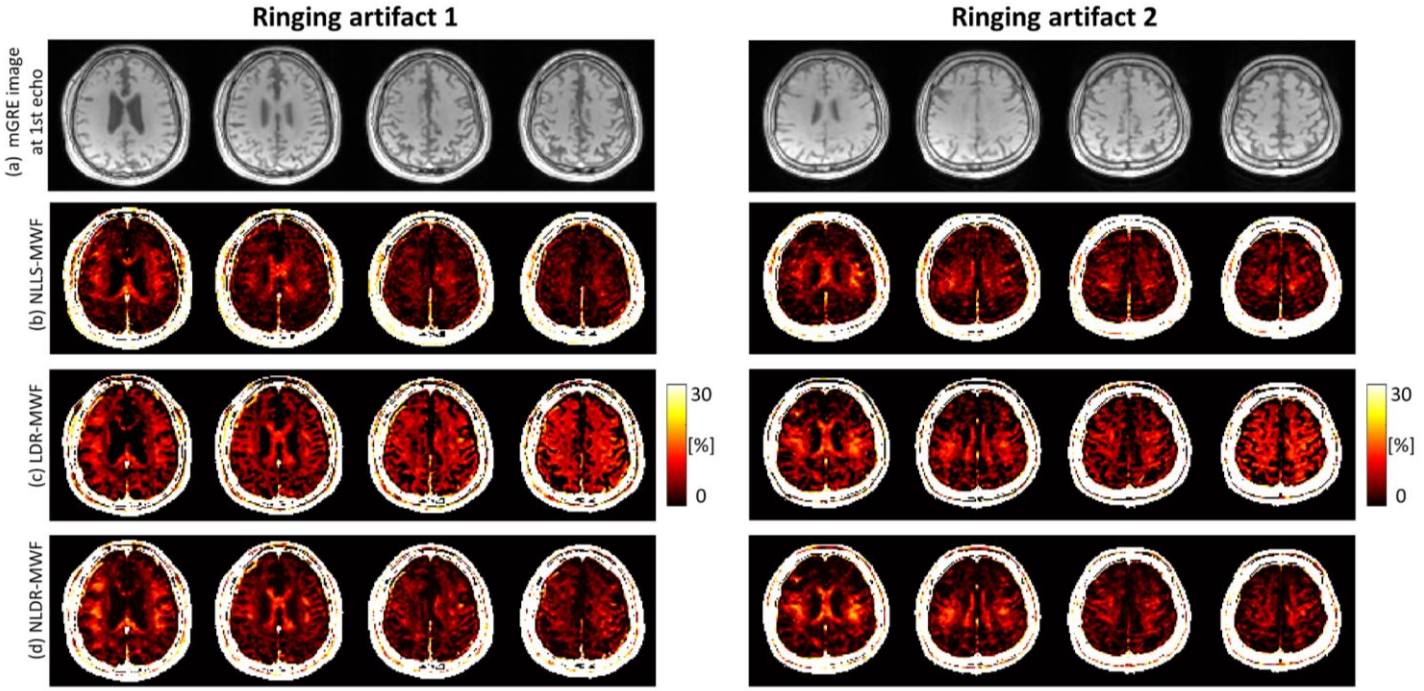

Figure 5.9. Four representative slices for ringing artifact corrupted cases.

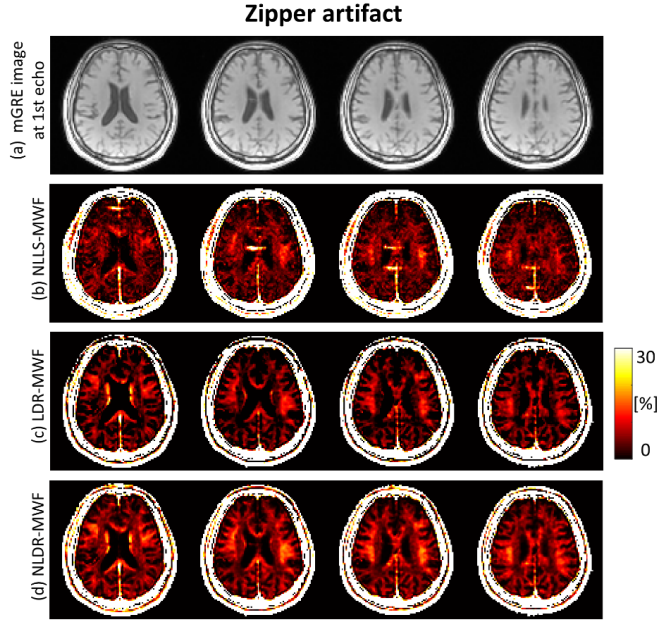

Figure 5.10. Four representative slices for zipper artifact corrupted case.

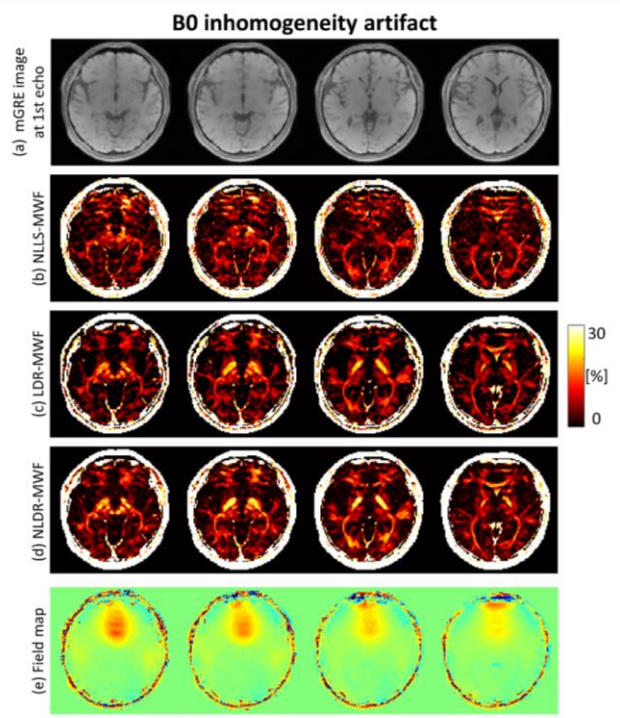

Figure 5.11. Four representative slices for B0 inhomogeneity artifact corrupted case.

The component-wise analysis for NLLS-MWF and NLDR-MWF is shown in Figure 5.12. The amplitude map and R2* map was more clearly visualized for NLDR-MWF than NLLS-MWF (Figure 5.12a and 5.12b). The histogram of amplitude using NLLS-MWF and NLDR-MWF was well corresponded (Figure 5.12c). The histogram of $T_{2,my}^{*}$ using NLLS-MWF was biased to 10ms, while the histogram of $T_{2,ax}^{*}$ and $T_{2,ex}^{*}$ using NLDR-MWF was biased to 60ms and 45ms, respectively (Figure 5.12d).

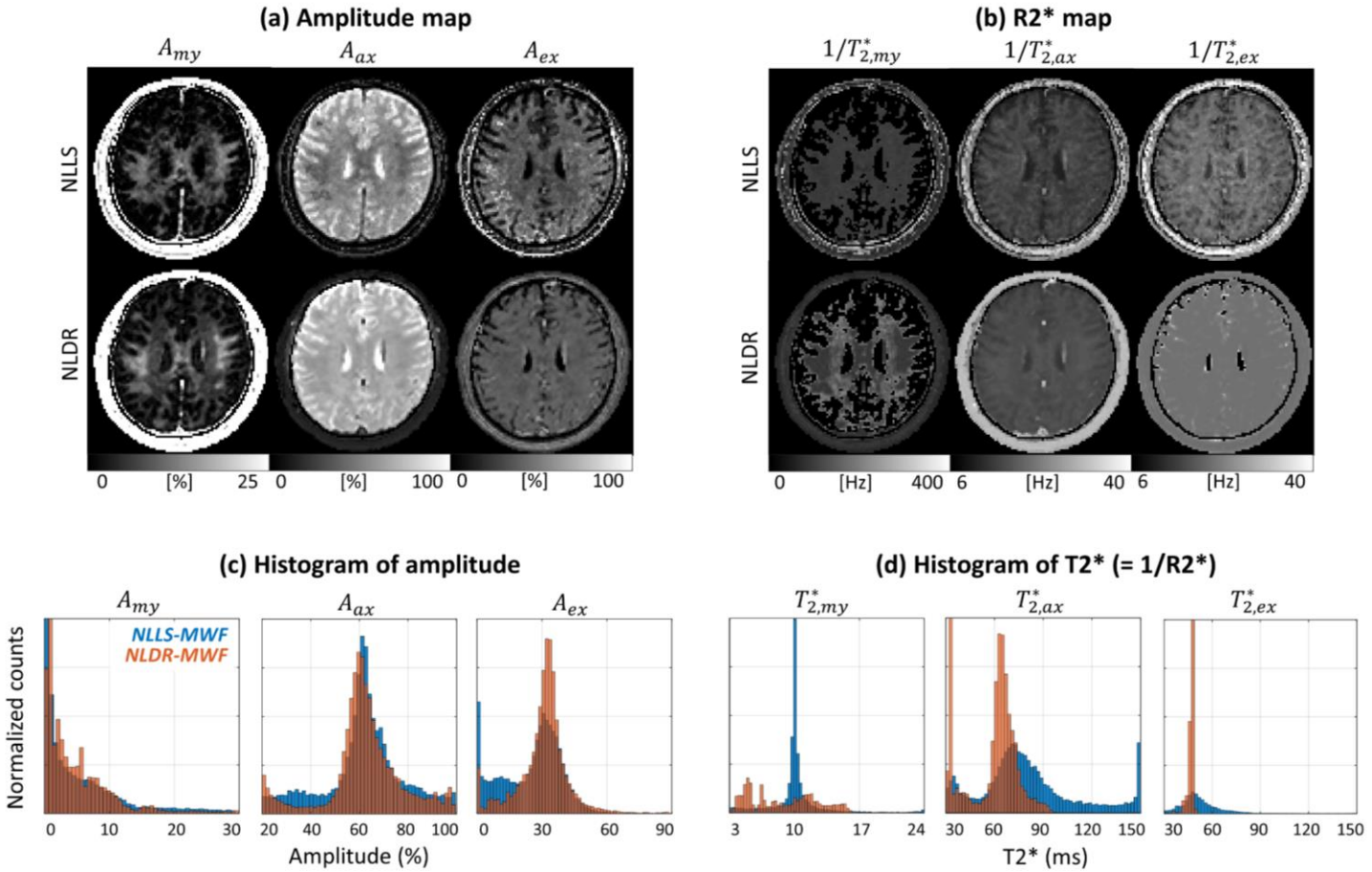
(a) Amplitude map
A_{my}
A_{ax}
A_{ex}
NLLS
NLDR
0 [%] 25
0 [%] 100
0 [%] 100
(b) R2* map
$1/T^*_{2,my}$
$1/T^*_{2,ax}$
$1/T^*_{2,ex}$
NLLS
NLDR
0 [Hz] 400
6 [Hz] 40
6 [Hz] 40
(c) Histogram of amplitude
A_{my}
A_{ax}
A_{ex}
NLLS-MWF
NLDR-MWF
Normalized counts
0 10 20 30
20 40 60 80 100
0 30 60 90
Amplitude (%)
(d) Histogram of T2* (= 1/R2*)
$T^*_{2,my}$
$T^*_{2,ax}$
$T^*_{2,ex}$
3 10 17 24
30 60 90 120 150
30 60 90 120 150
T2* (ms)

Figure 5.12. Comparison of component-wise analysis for NLLS-MWF and NLDR-MWF. (a) amplitude map and (b) R2* map. (c) histogram of amplitude and (d) histogram of R2*. The R2* map of myelin water component was masked. Note that mono-exponential curve-fitting was processed for each low dimension component of rDAE. Note that the noise.

5.4 Discussion

In this study, I propose a nonlinear dimensionality reduction (NLDR) method to separate multi-component T2* sources from mGRE images. Based on the linear low dimensionality of mGRE source signals discerned by rPCA-MWF (referred here as LDR-MWF), I suggest rDAE as a nonlinear approach.

The NLDR-MWF has several improvements compared to the LDR-MWF. First, the dimensionality reduction of the proposed method is expanded to a complex-valued attribute of the signal. As LDR-MWF implemented NMF for nuclear norm minimization, the low dimensionality of mGRE sources was limited to the magnitude domain. By substituting NMF for DAE, the low dimensional feature can be extracted from the concatenated real and imaginary signal. The incorporation of a complex-valued signal feature improves the accuracy of MWF for high fiber anisotropy with low MWF in simulation. It supports that LDR-MWF and others are significantly different for perpendicular ROI of in-vivo. Second, each low dimensional component of the proposed method well corresponds to myelin, axonal, and extracellular water components. As LDR-MWF implemented NNDSVD for initial estimation, it cannot differentiate two slowly decaying signals (i.e., axonal and extracellular water) which are lack of orthogonality. By replacing NNDSVD with a model-based pre-trained network, those signals are distinguished.

It is noteworthy that the noise and artifact robustness of LDR-MWF is maintained for NLDR-MWF as well. By reducing the size of hidden layers, the DAE is trained to represent

the hidden feature of the dataset so that each T2* source signal is represented with intrinsic dimensionality (i.e., the size of the bottleneck layer). Subsequent sparsifying operator for residual signal encourages the separation of anomaly features that does not reside in low dimensional subspace. Consequently, the artifact robustness of NLDR-MWF is accomplished similarly to LDR-MWF.

Several modifications are worthy to investigate for future work. First, the complex-valued neural network can be implemented to the proposed method. While the input signal was arranged by concatenating the real and the imaginary part of the complex-valued signal as in [129-131], the complex-valued neural network can improve the performance [132]. The activation function considering phase evolution as well as complex-valued weights can improve the signal deviation in the NLDR of DAE. Second, the variational autoencoder can be implemented to the proposed method [133]. While a simple autoencoder was designed by stacking the multiple layers in this study, the consideration of probabilistic distribution for latent feature could improve the low dimensional feature extraction.

5.5 Conclusion

In this study, I present a nonlinear dimensionality reduction method for MWF mapping. The low dimensionality feature is extracted using a deep autoencoder while encouraging the sparsity of residuals. The proposed method not only maintains the robustness for noise and artifacts in linear dimensionality reduction approach, but also improved the accuracy

of MWF map by considering the complex-valued attributes. The proposed method may be extended in various ways including implementation of complex-valued activation function, and improved network design.

Chapter 6

Conclusion

This chapter summarizes the dimensionality reduction methods for spatiotemporal MRI presented in this dissertation. PCA, rPCA, and rDAE have been optimized for MRSI and MGRE datasets, and the low dimensional temporal feature has been effectively extracted and investigated.

In Chapter 3, a linear dimensionality reduction technique has been implemented to the reconstruction of hyperpolarized dynamic 13C MRSI. Based on the spectroscopic signal model, the 13C MRSI dataset possesses the spatiotemporal correlation, and it allows the distinction of temporal basis function and spatial coefficient. The temporal basis features have been extracted over dynamic frames and the consistency has been investigated. Finally, the single basis acquisition scheme has been proposed.

In Chapter 4, a robust linear dimensionality reduction technique has been implemented to separate multi-component exponential sources from MGRE. Considering the low dimensional feature of sources, NMF and hankelization have been implemented to reduce the dimensionality. Additionally, the separation of sparse component improves the robustness of low dimensional component against noise and artifacts. The low dimensional components well corresponded to the literature source signals.

In Chapter 5, a nonlinear dimensionality reduction technique has been implemented to separate complex-valued multi-component exponential sources from MGRE. The proposed method not only maintains the robustness for noise and artifacts in linear dimensionality reduction approach, but also improved the accuracy of the MWF map by considering the complex-valued attributes. The proposed method may be extended in various ways including implementation of complex-valued activation function, and improved network design.

References

1. Bloembergen, N., E.M. Purcell, and R.V. Pound, Relaxation Effects in Nuclear Magnetic Resonance Absorption. Physical Review, 1948. **73**(7): p. 679-712.
2. MA Bernstein, K.K., XJ Zhou, Handbook of MRI pulse sequences. 2004.
3. Bloch, F., Nuclear Induction. Physical Review, 1946. **70**(7-8): p. 460-474.
4. Hotelling, H., Analysis of a complex of statistical variables into principal components. Journal of educational psychology, 1933. **24**(6): p. 417-441.
5. Eckart, C., The approximation of one matrix by another of lower rank. Psychometrika, 1936. **1**(3): p. 211-218.
6. Jolliffe, Principal Component Analysis. Springer. 1986.
7. Van Der, M., Dimensionality reduction: a comparative. Journal of machine learning research, 2009. **10**(66-71).
8. Strang, G., Linear Algebra and Learning from Data. 2020.
9. Candès, E.J., et al., Robust principal component analysis? Journal of the ACM, 2011. **58**(3): p. 1-37.
10. Donoho, D.L., For most large underdetermined systems of linear equations the minimal 1-norm solution is also the sparsest solution. Communications on pure and applied mathematics, 2006. **59**(6): p. 797-829.
11. Boyd, S., et al., Distributed Optimization and Statistical Learning via the Alternating Direction Method of Multipliers. Foundations and Trends® in Machine Learning, 2011. **3**(1): p. 1-122.
12. Hinton, G.E. and R.R. Salakhutdinov, Reducing the Dimensionality of Data with Neural Networks. Science, 2006. **313**(5786): p. 504.
13. Zhou, C.a.P., Randy C., Anomaly Detection with Robust Deep Autoencoders, in Proceedings of the 23rd ACM SIGKDD International Conference on Knowledge Discovery and Data Mining. 2017, Association for Computing Machinery: Halifax, NS, Canada. p. 665–674.

14. Dykstra, J.P.B.L., A Method for Finding Projections onto the Intersection of Convex Sets in Hilbert Spaces. Advances in Order Restricted Statistical Inference, 1986.
15. Ardenkjær-Larsen, J.H., et al., Increase in signal-to-noise ratio of > 10,000 times in liquid-state NMR. Proceedings of the National Academy of Sciences, 2003. **100**(18): p. 10158-10163.
16. Chen, A.P., et al., Hyperpolarized C-13 spectroscopic imaging of the TRAMP mouse at 3T—Initial experience. Magnetic Resonance in Medicine, 2007. **58**(6): p. 1099-1106.
17. Tran, M., et al., First-in-human in vivo non-invasive assessment of intra-tumoral metabolic heterogeneity in renal cell carcinoma. The Birth of Institute of Radiology. **0**(0): p. 20190003.
18. Hu, S., et al., In Vivo Carbon-13 Dynamic MRS and MRSI of Normal and Fasted Rat Liver with Hyperpolarized ^{13}C-Pyruvate. Molecular Imaging and Biology, 2009. **11**(6): p. 399.
19. Day, S.E., et al., Detecting response of rat C6 glioma tumors to radiotherapy using hyperpolarized [1-^{13}C] pyruvate and ^{13}C magnetic resonance spectroscopic imaging. Magnetic Resonance in Medicine, 2011. **65**(2): p. 557-563.
20. Zierhut, M.L., et al., Kinetic modeling of hyperpolarized 1-13C pyruvate metabolism in normal rats and TRAMP mice. Journal of Magnetic Resonance, 2010. **202**(1): p. 85-92.
21. Day, S.E., et al., Detecting tumor response to treatment using hyperpolarized ^{13}C magnetic resonance imaging and spectroscopy. Nature Medicine, 2007. **13**: p. 1382.
22. Laustsen, C., et al., Assessment of early diabetic renal changes with hyperpolarized [1-13C]pyruvate. Diabetes/Metabolism Research and Reviews, 2013. **29**(2): p. 125-129.
23. Laustsen, C., et al., Hyperpolarized 13C urea relaxation mechanism reveals renal changes in diabetic nephropathy. Magnetic Resonance in Medicine, 2016. **75**(2): p.

515-518.

24. von Morze, C., et al., Detection of localized changes in the metabolism of hyperpolarized gluconeogenic precursors 13C-lactate and 13C-pyruvate in kidney and liver. Magnetic Resonance in Medicine, 2017. **77**(4): p. 1429-1437.
25. Qi, H., et al., Acute renal metabolic effect of metformin assessed with hyperpolarised MRI in rats. Diabetologia, 2018. **61**(2): p. 445-454.
26. Månsson, S., et al., 13C imaging—a new diagnostic platform. European Radiology, 2006. **16**(1): p. 57-67.
27. Mayer, D., et al., Dynamic and high-resolution metabolic imaging of hyperpolarized [1-^{13}C]-pyruvate in the rat brain using a high-performance gradient insert. Magnetic Resonance in Medicine, 2011. **65**(5): p. 1228-1233.
28. Wang, J.-X., et al., Accelerated chemical shift imaging of hyperpolarized ^{13}C metabolites. Magnetic Resonance in Medicine, 2016. **76**(4): p. 1033-1038.
29. Chen, H.-Y., et al., Assessing Prostate Cancer Aggressiveness with Hyperpolarized Dual-Agent 3D Dynamic Imaging of Metabolism and Perfusion. Cancer Research, 2017. **77**(12): p. 3207-3216.
30. Cao, P., et al., Accelerated high-bandwidth MR spectroscopic imaging using compressed sensing. Magnetic Resonance in Medicine, 2016. **76**(2): p. 369-379.
31. Wiesinger, F., et al., IDEAL spiral CSI for dynamic metabolic MR imaging of hyperpolarized [1-^{13}C]pyruvate. Magnetic Resonance in Medicine, 2012. **68**(1): p. 8-16.
32. Cunningham, C.H., et al., Pulse sequence for dynamic volumetric imaging of hyperpolarized metabolic products. Journal of Magnetic Resonance, 2008. **193**(1): p. 139-146.
33. Lupo, J.M., et al., Analysis of hyperpolarized dynamic 13C lactate imaging in a transgenic mouse model of prostate cancer. Magnetic Resonance Imaging. **28**(2): p. 153-162.
34. Lau, A.Z., et al., Rapid multislice imaging of hyperpolarized ^{13}C pyruvate and

bicarbonate in the heart. Magnetic Resonance in Medicine, 2010. **64**(5): p. 1323-31.

35. Reed, G.D., et al., A method for simultaneous echo planar imaging of hyperpolarized 13C pyruvate and 13C lactate. Journal of Magnetic Resonance, 2012. **217**: p. 41-47.
36. Sigfridsson, A., et al., Hybrid multiband excitation multiecho acquisition for hyperpolarized ^{13}C spectroscopic imaging. Magnetic Resonance in Medicine, 2015. **73**(5): p. 1713-1717.
37. Lam, F., et al., High-resolution 1H-MRSI of the brain using SPICE: Data acquisition and image reconstruction. Magnetic Resonance in Medicine, 2016. **76**(4): p. 1059-1070.
38. Lam, F. and Z.P. Liang, A subspace approach to high-resolution spectroscopic imaging. Magnetic Resonance in Medicine, 2014. **71**(4): p. 1349-1357.
39. Lee, H., et al., High resolution hyperpolarized 13C MRSI using SPICE at 9.4T. Magnetic Resonance in Medicine, 2018. **80**(2): p. 703-710.
40. Ma, C., et al., High-resolution dynamic 31P-MRSI using a low-rank tensor model. Magnetic Resonance in Medicine, 2017. **78**(2): p. 419-428.
41. Haldar, J.P. and Z.P. Liang. Spatiotemporal imaging with partially separable functions: A matrix recovery approach. in 2010 IEEE International Symposium on Biomedical Imaging: From Nano to Macro. 2010.
42. Liang, Z.p. Spatiotemporal Imaging with Partially Seperable Functions. in 2007 4th IEEE International Symposium on Biomedical Imaging: From Nano to Macro. 2007.
43. Haldar, J.P., et al., Anatomically constrained reconstruction from noisy data. Magnetic Resonance in Medicine, 2008. **59**(4): p. 810-818.
44. Eslami, R. and M. Jacob, Robust Reconstruction of MRSI Data Using a Sparse Spectral Model and High Resolution MRI Priors. IEEE Transactions on Medical Imaging, 2010. **29**(6): p. 1297-1309.

45. Kasten, J., F. Lazeyras, and D.V.D. Ville, Data-Driven MRSI Spectral Localization Via Low-Rank Component Analysis. IEEE Transactions on Medical Imaging, 2013. **32**(10): p. 1853-1863.
46. Brindle, K., Watching tumours gasp and die with MRI: the promise of hyperpolarised 13C MR spectroscopic imaging. The British Journal of Radiology, 2012. **85**(1014): p. 697-708.
47. Peng, X., et al. Correction of field inhomogeneity effects on limited k-space MRSI data using anatomical constraints. in 2010 Annual International Conference of the IEEE Engineering in Medicine and Biology. 2010.
48. Tamir, J.I., et al., T2 shuffling: Sharp, multicontrast, volumetric fast spin-echo imaging. Magnetic Resonance in Medicine, 2017. **77**(1): p. 180-195.
49. Recht, B., M. Fazel, and P.A. Parrilo, Guaranteed Minimum-Rank Solutions of Linear Matrix Equations via Nuclear Norm Minimization. SIAM Review, 2010. **52**(3): p. 471-501.
50. Dutta, P., et al., Evaluation of LDH-A and Glutaminase Inhibition In Vivo by Hyperpolarized 13C-Pyruvate Magnetic Resonance Spectroscopy of Tumors Cancer Research, 2013. **73**(14): p. 4190-4195.
51. Stein, S.E. and D.R. Scott, Optimization and testing of mass spectral library search algorithms for compound identification. Journal of the American Society for Mass Spectrometry, 1994. **5**(9): p. 859-866.
52. Daniels, C.J., et al., A comparison of quantitative methods for clinical imaging with hyperpolarized 13C-pyruvate. NMR in Biomedicine, 2016. **29**(4): p. 387-399.
53. Hill, D.K., et al., Model Free Approach to Kinetic Analysis of Real-Time Hyperpolarized 13C Magnetic Resonance Spectroscopy Data. PLOS ONE, 2013. **8**(9): p. e71996.
54. Mather, A. and C. Pollock, Glucose handling by the kidney. Kidney International, 2011. **79**: p. S1-S6.
55. Neumiller, J.J., R.Z. Alicic, and K.R. Tuttle, Therapeutic Considerations for

Antihyperglycemic Agents in Diabetic Kidney Disease. Journal of the American Society of Nephrology, 2017. **28**(8): p. 2263-2274.

56. Kan, H.E., et al., In vivo 31P MRS detection of an alkaline inorganic phosphate pool with short T1 in human resting skeletal muscle. NMR in Biomedicine, 2010. **23**(8): p. 995-1000.
57. Andronesi, O.C., et al., Spectroscopic imaging with improved gradient modulated constant adiabaticity pulses on high-field clinical scanners. Journal of Magnetic Resonance, 2010. **203**(2): p. 283-293.
58. Bankson, J.A., et al., Kinetic Modeling and Constrained Reconstruction of Hyperpolarized [1-13C]-Pyruvate Offers Improved Metabolic Imaging of Tumors. Cancer Research, 2015. **75**(22): p. 4708-4717.
59. Mackay, A., et al., In vivo visualization of myelin water in brain by magnetic resonance. Magnetic Resonance in Medicine, 1994. **31**(6): p. 673-677.
60. Whittall, K.P., et al., In vivo measurement of T2 distributions and water contents in normal human brain. Magnetic Resonance in Medicine, 1997. **37**(1): p. 34-43.
61. Du, Y.P., et al., Fast multislice mapping of the myelin water fraction using multicompartment analysis of T decay at 3T: A preliminary postmortem study. Magnetic Resonance in Medicine, 2007. **58**(5): p. 865-870.
62. van Gelderen, P., et al., Nonexponential T_2^* decay in white matter. Magnetic Resonance in Medicine, 2012. **67**(1): p. 110-7.
63. Nam, Y., et al., Improved estimation of myelin water fraction using complex model fitting. Neuroimage, 2015. **116**: p. 214-21.
64. Alonso-Ortiz, E., et al., Field inhomogeneity correction for gradient echo myelin water fraction imaging. Magnetic Resonance in Medicine, 2017. **78**(1): p. 49-57.
65. Yablonskiy, D.A., et al., Voxel spread function method for correction of magnetic field inhomogeneity effects in quantitative gradient-echo-based MRI. 2013. **70**(5): p. 1283-1292.
66. Lee, H., et al., Improved three-dimensional multi-echo gradient echo based myelin

water fraction mapping with phase related artifact correction. Neuroimage, 2018. **169**: p. 1-10.

67. Nam, Y., D.H. Kim, and J. Lee, Physiological noise compensation in gradient-echo myelin water imaging. Neuroimage, 2015. **120**: p. 345-9.
68. Layton, K.J., et al., Modelling and Estimation of Multicomponent T_2 Distributions. IEEE Transactions on Medical Imaging, 2013. **32**(8): p. 1423-1434.
69. McKeown, M.J., L.K. Hansen, and T.J. Sejnowsk, Independent component analysis of functional MRI: what is signal and what is noise? Current Opinion in Neurobiology, 2003. **13**(5): p. 620-629.
70. Nakai, T., et al., Application of independent component analysis to magnetic resonance imaging for enhancing the contrast of gray and white matter. NeuroImage, 2004. **21**(1): p. 251-260.
71. Molina-Romero, M., et al., A diffusion model-free framework with echo time dependence for free-water elimination and brain tissue microstructure characterization. Magnetic Resonance in Medicine, 2018. **80**(5): p. 2155-2172.
72. Otazo, R., E. Candès, and D.K. Sodickson, Low-rank plus sparse matrix decomposition for accelerated dynamic MRI with separation of background and dynamic components. Magnetic Resonance in Medicine, 2015. **73**(3): p. 1125-1136.
73. Levine, E., et al., Accelerated three-dimensional multispectral MRI with robust principal component analysis for separation of on- and off-resonance signals. 2018. **79**(3): p. 1495-1505.
74. Jin, K.H., et al., MRI artifact correction using sparse + low-rank decomposition of annihilating filter-based hankel matrix. Magnetic Resonance in Medicine, 2017. **78**(1): p. 327-340.
75. Campbell-Washburn, A.E., et al., Using the robust principal component analysis algorithm to remove RF spike artifacts from MR images. 2016. **75**(6): p. 2517-2525.

76. Whittall, K.P. and A.L. MacKay, Quantitative interpretation of NMR relaxation data. Journal of Magnetic Resonance, 1989. **84**(1): p. 134-152.
77. Alonso-Ortiz, E., I.R. Levesque, and G.B. Pike, Multi-gradient-echo myelin water fraction imaging: Comparison to the multi-echo-spin-echo technique. Magnetic Resonance in Medicine, 2018. **79**(3): p. 1439-1446.
78. Hwang, D., D.-H. Kim, and Y.P. Du, In vivo multi-slice mapping of myelin water content using T2* decay. NeuroImage, 2010. **52**(1): p. 198-204.
79. Lee, H., Y. Nam, and D.-H. Kim, Echo time-range effects on gradient-echo based myelin water fraction mapping at 3T. Magnetic Resonance in Medicine, 2019. **81**(4): p. 2799-2807.
80. Ding, C., T. Li, and M.I. Jordan, Convex and semi-nonnegative matrix factorizations. IEEE Transactions on Pattern Analysis and Machine Intelligence, 2010. **32**(1): p. 45-55.
81. Lee, D.D. and H.S. Seung, Learning the parts of objects by non-negative matrix factorization. Nature, 1999. **401**: p. 788-791.
82. Boutsidis, C. and E. Gallopoulos, SVD based initialization: A head start for nonnegative matrix factorization. Pattern Recognition, 2008. **41**(4): p. 1350-1362.
83. Xue, Y., et al., Clustering-based initialization for non-negative matrix factorization. Applied Mathematics and Computation, 2008. **205**(2): p. 525-536.
84. Rezaei, M. and R. Boostani, Using the genetic algorithm to enhance nonnegative matrix factorization initialization. Expert Systems, 2014. **31**(3): p. 213-219.
85. Fazel, M., et al., Hankel Matrix Rank Minimization with Applications to System Identification and Realization. SIAM Journal on Matrix Analysis and Applications, 2013. **34**(3): p. 946-977.
86. Cao, P., et al., Shuffled magnetization-prepared multicontrast rapid gradient-echo imaging. Magnetic Resonance in Medicine, 2018. **79**(1): p. 62-70.
87. Cai, J.F., et al., Robust recovery of complex exponential signals from random Gaussian projections via low rank Hankel matrix reconstruction. Applied and

Computational Harmonic Analysis, 2016. **41**(2): p. 470-490.

88. De Groen, P. and B. De Moor, The fit of a sum of exponentials to noisy data. Journal of Computational and Applied Mathematics, 1987. **20**: p. 175-187.
89. Trzasko, J.D., Exploiting local low-rank structure in higher-dimensional MRI applications. Proceedings of SPIE, 2013. **8858**.
90. Zhang, T., J.M. Pauly, and I.R. Levesque, Accelerating parameter mapping with a locally low rank constraint. Magn. Reson. Med., 2015. **73**(2): p. 655-661.
91. Lima da Cruz, G., et al., Sparsity and locally low rank regularization for MR fingerprinting. Magnetic Resonance in Medicine, 2019. **81**(6): p. 3530-3543.
92. Wang, Y., et al., A New Alternating Minimization Algorithm for Total Variation Image Reconstruction. SIAM Journal on Imaging Sciences, 2008. **1**(3): p. 248-272.
93. Goldstein, T. and S. Osher, The Split Bregman Method for L1-Regularized Problems. SIAM Journal on Imaging Sciences, 2009. **2**(2): p. 323-343.
94. Cai, J.-F., E.J. Candès, and Z. Shen, A Singular Value Thresholding Algorithm for Matrix Completion. SIAM Journal on Optimization, 2010. **20**(4): p. 1956-1982.
95. Kroeker, R.M. and R. Mark Henkelman, Analysis of biological NMR relaxation data with continuous distributions of relaxation times. Journal of Magnetic Resonance, 1986. **69**(2): p. 218-235.
96. Graham, S.J., P.L. Stanchev, and M.J. Bronskill, Criteria for analysis of multicomponent tissue T2 relaxation data. Magnetic Resonance in Medicine, 1996. **35**(3): p. 370-378.
97. Geeraert, B.L., et al., A comparison of inhomogeneous magnetization transfer, myelin volume fraction, and diffusion tensor imaging measures in healthy children. Neuroimage, 2017. **182**: p. 343-350.
98. Smith, S.M., Fast robust automated brain extraction. Human Brain Mapping, 2002. **17**(3): p. 143-155.
99. Lenz, C., M. Klarhöfer, and K. Scheffler, Feasibility of in vivo myelin water imaging using 3D multigradient-echo pulse sequences. Magnetic Resonance in

Medicine, 2012. **68**(2): p. 523-528.

100. Zimmermann, M., et al., Accelerated Parameter Mapping of Multiple-Echo Gradient-Echo Data Using Model-Based Iterative Reconstruction. IEEE Transactions on Medical Imaging, 2018. **37**(2): p. 626-637.
101. Sati, P., et al., Micro-compartment specific T2∗ relaxation in the brain. NeuroImage, 2013. **77**: p. 268-278.
102. Wharton, S. and R. Bowtell, Fiber orientation-dependent white matter contrast in gradient echo MRI. roceedings of the National Academy of Sciences of the United States of America, 2012. **109**(45): p. 18559-18564.
103. Langkammer, C., et al., Quantitative susceptibility mapping (QSM) as a means to measure brain iron? A post mortem validation study. NeuroImage, 2012. **62**(3): p. 1593-1599.
104. Yao, B., et al., Susceptibility contrast in high field MRI of human brain as a function of tissue iron content. NeuroImage, 2009. **44**(4): p. 1259-1266.
105. Laule, C., et al., Water content and myelin waterfraction in multiple sclerosis. Journal of Neurology, 2004. **251**(3): p. 284-293.
106. Neema, M., et al., 3 T MRI relaxometry detects T2 prolongation in the cerebral normal-appearing white matter in multiple sclerosis. NeuroImage, 2009. **46**(3): p. 633-641.
107. Li, X., et al., Detection of demyelination in multiple sclerosis by analysis of T2* relaxation at 7 T. NeuroImage: Clinical, 2015. **7**: p. 709-714.
108. Manogaran, P., et al., Quantifying visual pathway axonal and myelin loss in multiple sclerosis and neuromyelitis optica. NeuroImage: Clinical, 2016. **11**: p. 743-750.
109. Jeong, I.H., et al., Normal-appearing white matter demyelination in neuromyelitis optica spectrum disorder. European Journal of Neurology, 2017. **24**(4): p. 652-658.
110. Bouhrara, M., et al., Evidence of demyelination in mild cognitive impairment and dementia using a direct and specific magnetic resonance imaging measure of

myelin content. Alzheimer's & Dementia, 2018. **14**(8): p. 998-1004.

111. Borich, M.R., et al., Evaluation of white matter myelin water fraction in chronic stroke. NeuroImage: Clinical, 2013. **2**: p. 569-580.

112. Lee, D., et al., Single-scan z-shim method for reducing susceptibility artifacts in gradient echo myelin water imaging. Magnetic Resonance in Medicine, 2018. **80**(3): p. 1101-1109.

113. Does, M.D., et al., Evaluation of principal component analysis image denoising on multi-exponential MRI relaxometry. Magnetic Resonance in Medicine, 2019. **81**(6): p. 3503-3514.

114. Chen, N.-K., et al., A diffusion-matched principal component analysis (DM-PCA) based two-channel denoising procedure for high-resolution diffusion-weighted MRI. PloS one, 2018. **13**(4): p. e0195952-e0195952.

115. Song, J.E., et al., Blind Source Separation for Myelin Water Fraction Mapping using Multi-echo Gradient Echo Imaging. IEEE Transactions on Medical Imaging, 2020: p. 1-1.

116. Song, J.E., et al. Noise sensitivity study of model-free rPCA in Myelin Water Fraction Mapping using multi-echo GRE. in International Society for Magnetic Resonance in Medicine. 2019. Montreal, Canada.

117. Cai, J.-F., E.J. Candès, and Z. Shen, A Singular Value Thresholding Algorithm for Matrix Completion. 2010. **20**(4): p. 1956-1982.

118. Vincent, Stacked denoising autoencoders: Learning useful representations in a deep network with a local denoising criterion. Journal of machine learning research, 2010. **11**(dec).

119. Bengio, Y., A. Courville, and P. Vincent, Representation Learning: A Review and New Perspectives. IEEE Transactions on Pattern Analysis and Machine Intelligence, 2013. **35**(8): p. 1798-1828.

120. Hinton, G.E. and R.S. Zemel, Autoencoders, minimum description length and Helmholtz free energy, in Proceedings of the 6th International Conference on

Neural Information Processing Systems. 1993, Morgan Kaufmann Publishers Inc.: Denver, Colorado. p. 3–10.

121. Courville, I.G.a.Y.B.a.A., Deep Learning. 2016: MIT Press.

122. Mehta, J. and A. Majumdar, RODEO: Robust DE-aliasing autoencOder for real-time medical image reconstruction. Pattern Recognition, 2017. **63**: p. 499-510.

123. Majumdar, A., An autoencoder based formulation for compressed sensing reconstruction. Magnetic Resonance Imaging, 2018. **52**: p. 62-68.

124. Benou, A., et al., Ensemble of expert deep neural networks for spatio-temporal denoising of contrast-enhanced MRI sequences. Medical Image Analysis, 2017. **42**: p. 145-159.

125. Lam, F., Y. Li, and X. Peng, Constrained Magnetic Resonance Spectroscopic Imaging by Learning Nonlinear Low-Dimensional Models. IEEE Transactions on Medical Imaging, 2020. **39**(3): p. 545-555.

126. Soozy Jung, H.L., Kanghyun Ryu, Jae Eun Song, Yoonho Nam, Hojoon Lee, Donghyun Kim. Feasibility study on artificial neural network based myelin water fraction mapping. in 27th Annual Meeting of the International Society of Magnetic Resonance in Medicine,. 2019. Montreal, Canada.

127. Kim, C., et al., Generation of Large-Scale Simulated Utterances in Virtual Rooms to Train Deep-Neural Networks for Far-Field Speech Recognition in Google Home. 2017. 379-383.

128. Yeomans, J., et al., Simulating Time-Series Data for Improved Deep Neural Network Performance. IEEE Access, 2019. **7**: p. 131248-131255.

129. Akçakaya, M., et al., Scan-specific robust artificial-neural-networks for k-space interpolation (RAKI) reconstruction: Database-free deep learning for fast imaging. Magnetic Resonance in Medicine, 2019. **81**(1): p. 439-453.

130. Schlemper, J., et al., A Deep Cascade of Convolutional Neural Networks for Dynamic MR Image Reconstruction. IEEE Transactions on Medical Imaging, 2018. **37**(2): p. 491-503.

131. Eo, T., et al., KIKI-net: cross-domain convolutional neural networks for reconstructing undersampled magnetic resonance images. Magnetic Resonance in Medicine, 2018. **80**(5): p. 2188-2201.
132. Virtue, P., S.X. Yu, and M. Lustig. Better than real: Complex-valued neural nets for MRI fingerprinting. in 2017 IEEE International Conference on Image Processing. 2017.
133. Welling, D.P.K.a.M. Auto-Encoding Variational Bayes. arXiv, 2013. arXiv:1312.6114.

국문요약

시공간분해능 자기공명영상을 위한 차원축소법

자기공명영상은 다원적 영상 촬영방법으로, 이온화 및 침습적 시술 없이 인체 내부의 다양한 대조도를 제공한다. 이러한 자기공명영상의 유연성은 다중대비영상, 조직에서의 대사활동, 뇌의 기능활동, 전자기적 특성을 포함한 많은 응용을 가능케 한다.

시공간분해능 자기공명영상은 공간정보 뿐 아니라 시간정보도 제공할 수 있다. 몇몇 시공간분해능 자기공명영상은 시간차원에서 자유유도감쇠, T2* 이완, T1 이완 등 중복적인 특성을 가지고 있어, 이들을 저차원 부분공간을 통해 표현할 수 있다. 저차원 부분공간을 이용하여 재구성된 데이터셋은 원래 데이터셋보다 낮은 차원을 가지며, 이를 내재적 차원이라 일컫는다.

본 논문에서는 고차원 자기공명영상, 특히 자기공명분광영상과 다중에코경사에코 영상을 포함한 시공간분해능 자기공명영상을 위한 차원축소기법을 제안한다. 선형 접근방법으로, 주성분분석을 사용하여 동적 초분극화 13C 자기공명분광영상의 스펙트럼 기반의 일관성을 조사하였다. 추출된 스펙트럼 특성

은 신호대비잡음비 증가와 스캔시간 단축을 가능케 하였다. 또 다른 선형 접근방식인 강건한 주성분분석을 사용하여 다중에코경사에코 영상으로부터 수초물분율을 영상화 하였다. 추출된 시간 특성은 다중에코경사에코 영상의 성분 신호들의 특성과 유사하였다. 비선형 접근방법으로, 강건한 오토인코더를 사용하여 다중에코경사에코 영상으로부터 수초물분율을 영상화 하였다. 기존 강건한 주성분분석 방법의 잡음과 인공물에 대한 강건함이 유지되었을 뿐 아니라, 다중에코경사에코 영상의 복소신호의 추출을 가능케 하였다.

핵심어: 자기공명영상, 차원축소법, 주성분분석, 오토인코더, 기계학습